This is to certify that the

thesis entitled

A STUDY OF THE EFFECTS OF EXCITING THE INTAKE FLOW IN AN INTERNAL COMBUSTION ENGINE MODEL

presented by

Greg Ambrose

has been accepted towards fulfillment
of the requirements for

M.S. degree in Mechanical Engineering

M. M. Koochesfahani
Major professor

Date 4-16-97

DATE DUE	DATE DUE	DATE DUE

A STUDY OF THE EFFECTS OF EXCITING THE INTAKE FLOW IN AN INTERNAL COMBUSTION ENGINE MODEL

By

Greg Ambrose

A THESIS

Submitted to
Michigan State University
in partial fulfillment of the requirements
for the degree of

MASTERS OF SCIENCE

Department of Mechanical Engineering

1997

ABSTRACT

A STUDY OF THE EFFECTS OF EXCITING THE INTAKE FLOW IN AN INTERNAL COMBUSTION ENGINE MODEL

By

Greg Ambrose

The motivation of this experiment was to determine if exciting the flow in an internal combustion engine geometry could have positive effects on the developing large structures. The intent being a new method to improve the combustion process in internal combustion engine applications, by controlling the in-cylinder flow characteristics. The experiment used a water analog model of an internal combustion engine, and the focus of the study was on the intake stroke. The shear layer formed by the flow entering through the intake valve was perturbed by applying a disturbance about the nominal position of the intake valve. Sinusoidal disturbances with peak to peak amplitudes of 0.35 mm and 1.00 mm and frequencies incrementing by 10 Hz from 10 Hz to 90 Hz were used to excite the flow through various ranges of the intake stroke. The effects of these disturbances on the flow were first examined with flow visualization techniques, and then velocity fields were measured using Molecular Tagging Velocimetry (MTV).

The data, in the tumble plane, showed significant changes in the large scale flow structures. The MTV results of mean circulation and mean kinetic energy indicate up to a 40% increase in mean circulation, and a 30% increase in mean kinetic energy.

ACKNOWLEDGEMENTS

I would like to thank many of the people who have helped and assisted me in this work. I would like to thank my advisor Dr. Manooch Koochesfahani, who was the originator of the topic for this thesis, the members of my committee, Dr. Harold Schock and Dr. Daniel Nocera. For technical assistance and input on many matters, I would like to thank Rich Cohn, Thomas Stuecken, Bernd Stier, and CHuck Gendrich. Also a special thanks to the Center of Fundamental Material Research (CFMR) and the Materials Research Science and Engineering Center (MRSEC) at MSU funded by the National Science Foundation (NSF), for supporting this project and the Ford Motor Company for the donation of the equipment for the engine model.

TABLE OF CONTENTS

List of Tables

List of Figures

List of Figures

List of Figures

List of Symbols

Symbol	Description
A	Peak to Peak Amplitude of the Excitation
CA	Crank Angle
D	Characteristic Diameter
f	Frequency of the Excitation
H_z	Angular Momentum about the Z-Axis
I_{zz}	Moment of Inertia about the Z-Axis
KE	Kinetic Energy
N	Number of Engine Cycles
Re	Reynolds Number
RPM	Revolutions per Minute
St_D	Strouhal Number (fD/U)
Tz	Tumble Ratio about the Z-Axis
U	Characteristic Velocity
u,v,w	X, Y, and Z Components of Velocity
x,y,z	Coordinate System Axis
Greek	
ω	vorticity
Δ	Crank Angle Range of the Intake which the Excitation is Activated
Γ	Circulation
Θ	Engine Speed in Cycles per Second
Ω	Engine Speed in Radians per Second
Ψ	A Variable of Interest
Overscores	
~	RMS
-	Mean
Underscores	
_	Vector Representation

Chapter 1

INTRODUCTION

This study was undertaken to examine the effects of exciting the flow entering a piston-cylinder arrangement. To date, studies of exciting the flow entering an internal combustion engine have not been done; however, excited flows have been studied in other geometries. In these other flow arrangements, such as round jets, coaxial jets, and two stream mixing layers, it has been shown that perturbing the flow can modify the amount of the mixing down stream of the wake and turbulence intensities [2,3,4,5]. Studies of the excitation of round and coaxial jets have shown that excitation affects the way small vortical structures in the inner and outer mixing layers combine to form larger ones, which can change the large scale structures and promote turbulence. The desired results in the case of the piston-cylinder arrangement would be a way of controlling the flow characteristics to alter the large scale motions and increase turbulence. Control of turbulence in the bulk flow should provide control of the mixing and burn rates of an internal combustion engine; however, estimation of the direct impact of these changes in the flow on the performance or efficiency of an actual engine was not attempted in this study.

The intake flow most closely resembles that of an annular jet, but it does have some major differences, such as the time varying wall boundary conditions from the piston and cylinder, and a time varying mean velocity due to the sinusoidal movement of the piston. Since to the author's knowledge, no studies of excited annular jets have been done to date, an excited coaxial jet is the closest geometry for a possible comparison to the cur-

rent literature. Studies of excited coaxial jets have been done by Tang and Ko [2], and excited round jets by Zaman and Hussain [3,4]. Tang and Ko [2] studied excited coaxial jets with an inner to outer jet velocity ratio (Ui/Uo) of 0.3 (Uo = 50 m/s). They found broadband turbulence amplification when excited at a preferred Strouhal number of 1.16 ($St_D = fD_o/U_o$, where f is the forcing frequency, D_o is the diameter of the outer jet, and U_o is the outer jet velocity), and a gradual decrease in the amplification as St_D approached 4.0. Zaman and Hussain [3,4] found that a turbulent or laminar single round jet had amplification of turbulence when excited at Strouhal numbers in the range 0.25 to 1.2, with the maximum amplification of turbulence at $St_D = 0.85$.

A water analog model of an internal combustion engine was used, and the flow was excited by applying a disturbance about the nominal position of the intake valve. The intake valve in this IC engine model was located at the center of the cylinder and kept open at a fixed lift of 9 mm. Since water was used as the working fluid, the compression stroke was not examined, so only the effects during the intake stroke were studied. The excitation in this study was introduced by oscillating the intake valve to perturb its shear layer during the intake stroke. Various disturbance conditions were selected to examine structural changes in the flow on the basis of the disturbance's frequency, amplitude, and duration of the intake stroke when the excitation is active.

The effect of these disturbances on the bulk properties of the flow was first examined with flow visualization techniques, and then velocity fields of selected cases were measured using molecular tagging velocimetry, MTV, as done by Gendrich and Koochesfahani [1].

The flow visualization was performed at air equivalent engine speeds of 170 RPM, and 340 RPM. The velocimetry examined a speed of 340 RPM and a subset of the excitations done in the flow visualization to quantify the effects.

To use the results from excited jet studies as a first estimate of the relevant range of Strouhal numbers in the piston-cylinder arrangement, the velocity term in the Strouhal number has to be defined for the piston-cylinder flow. Since the flow through the intake valve is not steady due to the motion of the piston, a simplification would be to use the maximum mean velocity through the valve (at mid-stroke, CA=90 degrees)), to provide a single number for the Strouhal number. The corresponding Strouhal Number would be,

$$St_D = fD/U,$$

where f is the excitation frequency, D is a characteristic length of the geometry (i.e. valve diameter), and U is a characteristic velocity of the flow (i.e. maximum mean velocity through the valve opening). Using the above definition for the velocity in the Strouhal number and the results for maximum turbulence amplification from the jet studies (i.e. $St_D \approx 1$), a first approximation for preferred excitation frequencies is 31.3 Hz at an engine speed of 20 RPM (air equivalent speed of 340 RPM). Comparing the engine speed, Θ = 0.17 Hz (20 RPM), and the excitation frequency, f=31.3 Hz, it is seen that $f >> \Theta$.

In an effort to isolate the effects of the excitation parameters, sinusoidal disturbances of various amplitudes, frequencies, and excitation duration periods were used to excite the flow. The disturbances applied to the valve had amplitudes, A, of 0.35, 0.50, and 1.00 mm peak to peak, frequencies, f, incrementing by 10 Hz from 10 Hz to 90 Hz (this range

covers the first approximation for the preferred excitation frequencies), and excitation was activated during periods in the intake stroke, Δ, from 0-180, 40-180, 60-180, 0-18, 0-60 crank angle (CA) degrees, referenced to TDC (Top Dead Center) of the intake stroke. An examination of the bulk flow characteristics was then carried out for both in the natural (i.e. unperturbed) and perturbed states to study their effects.

The organization of this paper is divided into three remaining chapters. In Chapter 2, Experimental Equipment and Procedure, the engine model is first described, and then equipment and procedure for the flow visualization and MTV data acquisition are described. In the last part of Chapter 2, the MTV data reduction is described along with data correction methods to account for optical distortions created from the curvature of the cylinder. Chapter 3, Results and Discussion, examines selected flow visualization images which are used to evaluate the effects of the forcing parameters (A, f, and Δ) on the large scale motions near the end of the intake stroke. Chapter 3 continues with a discussion of the resulting cycle averaged velocity and vorticity fields from the MTV data which are compared to corresponding flow visualization results. Next, the convergence of the MTV data based on the number of engine cycles used in ensemble averaging is examined for the unperturbed case and one of the excited cases. The MTV results are used to evaluate the effects of the forcing parameters (A, f, and Δ) on the mean circulation and the mean kinetic energy. Chapter 3 ends with a discussion of other aspects of this study which could be examined in future studies in order to understand the effects of exciting the flow. Chapter 4, Conclusions, summarizes the trends observed within this study.

Chapter 2

EXPERIMENTAL EQUIPMENT AND PROCEDURE

2.1 The Water Analog Model of an Internal Combustion Engine.

The geometry of the piston cylinder arrangement, shown schematically in Figure 1, consisted of a 82.0 mm-diameter cylinder with a stroke of 82.4 mm. The piston used was flat, and incorporated Rulon rings for sealing with quartz and Polyethylene when sealing against Plexiglass. The piston and cylinder used for MTV were made of quartz, and Plexiglass was used for flow visualization. The valve diameter was 32 mm, and the lift was set for 9 mm, since typical engines have a maximum lift in the range of 9 to 12 mm. The valve was not operated by a cam as in a typical engine, but instead was held open at a clearance of 9 mm. This was done because water was used as the working fluid, and required the valve being open during the compression cycle. The source of excitation was the valve which was displaced about its nominal position. An Alpha-K model AV-6 shaker driven by a function generator displaced the valve, and the position was monitored by a Linear Variable Displacement Transducer (LVDT). The lowest amplitude that the shaker could produce with long term consistency was 0.35 mm; to go to lower amplitudes would often result in the motion slowly attenuating and occasionally stopping due to the friction in the valve guide interface. The shaker could produce output amplitudes of 0.35 mm with frequencies up to 90 Hz in water without exceeding its maximum power rating, and at amplitudes of 1.00 mm, the maximum frequency obtained was 60 Hz.

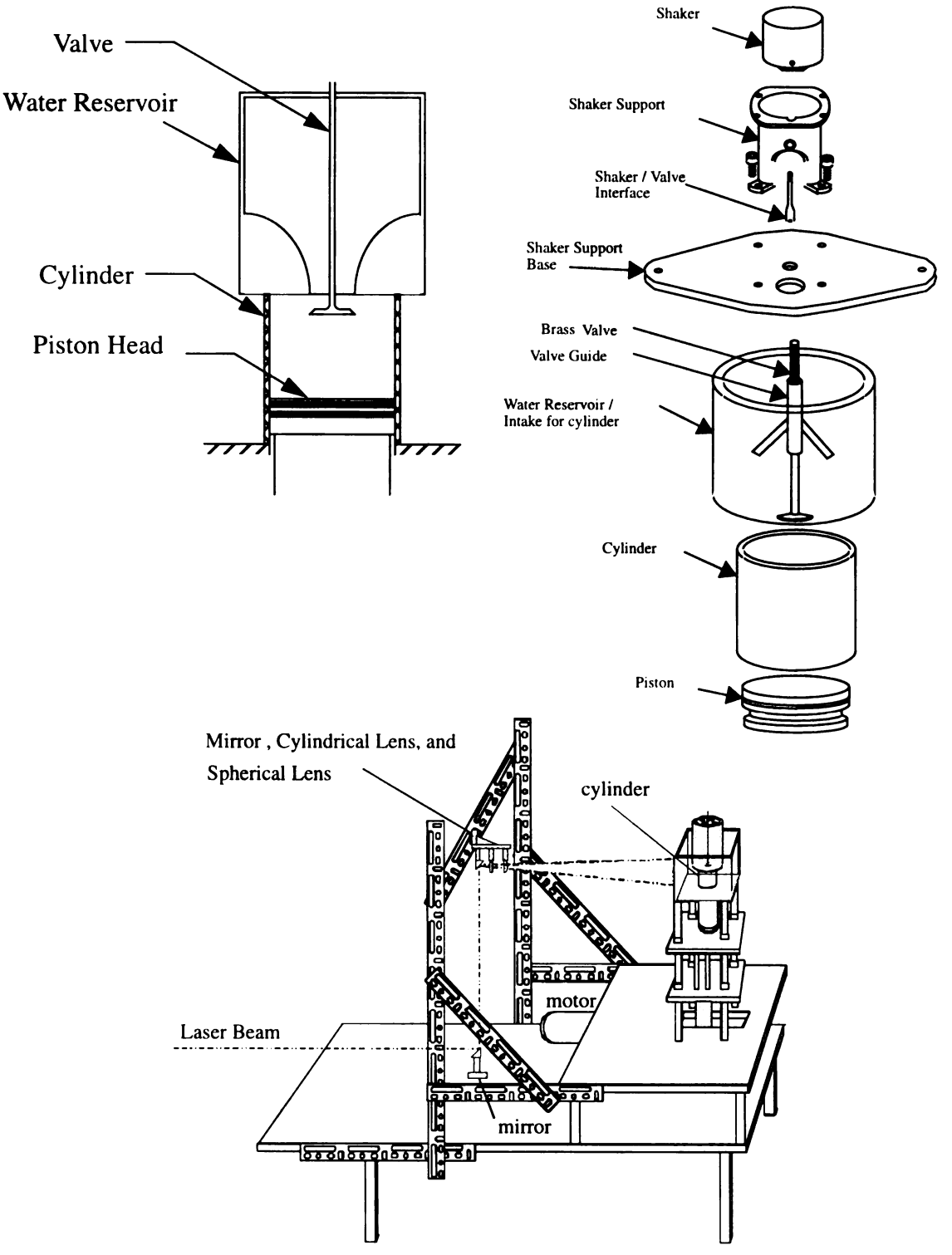

Figure 1. *Assembly view of the piston-cylinder set-up and view of the test rig.*

The engine cycle used for water analog model of the engine is plotted in Figure 2a, which shows that the piston remains at BDC throughout the compression and power strokes, but the intake and exhaust occur as normal, that should create acceptable initial conditions for the intake stroke. This cycle was generated with the cam profile of the crank shaft shown in Figure 2a.

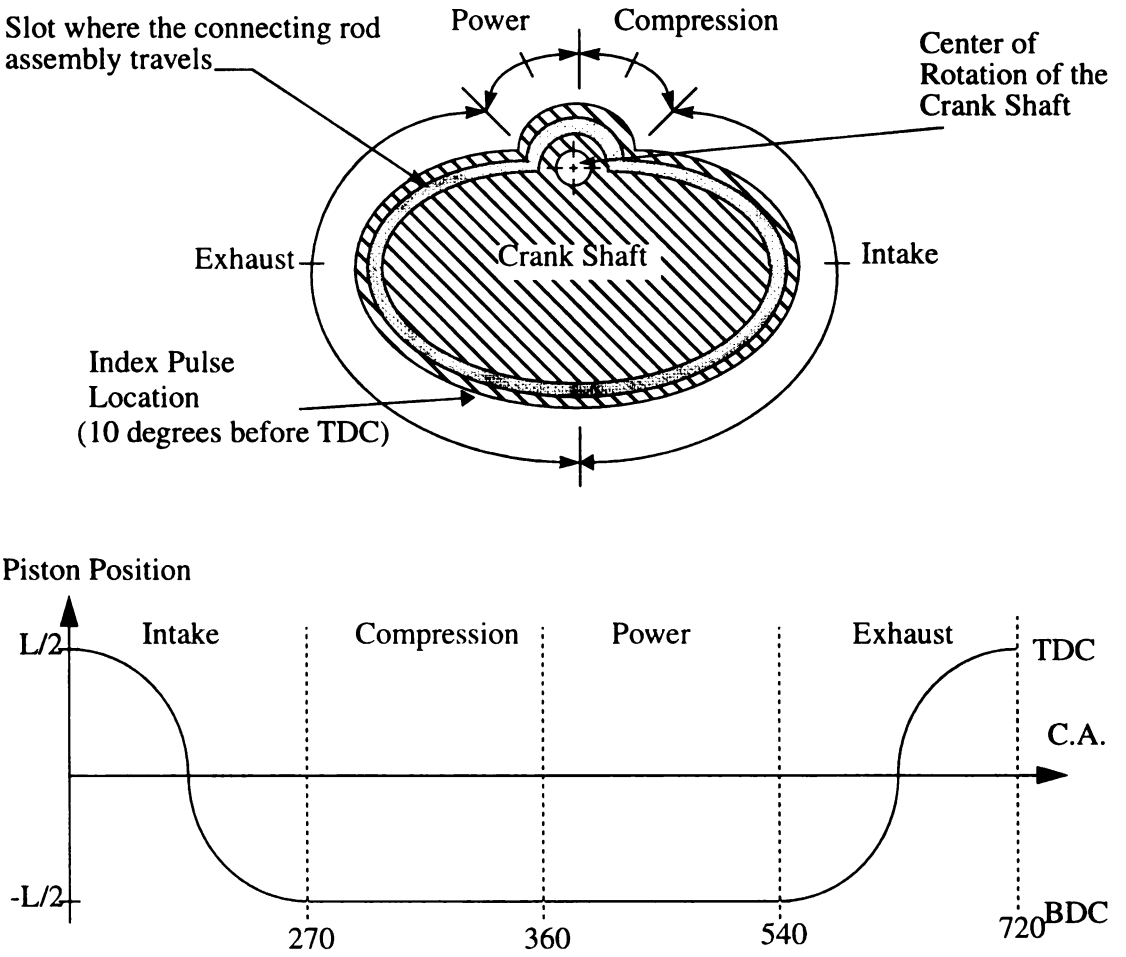

Figure 2a. Operating cycle used for the water analog model of an internal combustion engine.

The connecting rod mechanism was not allowed to have any horizontal motion; it fixed to

the piston at the top and the bottom was attached to the slot in the crank shaft with a roller as shown in Figure 2b. As the crank shaft rotated, the connecting rod would be translated up and down according to the cam profile shown in Figure 2a.

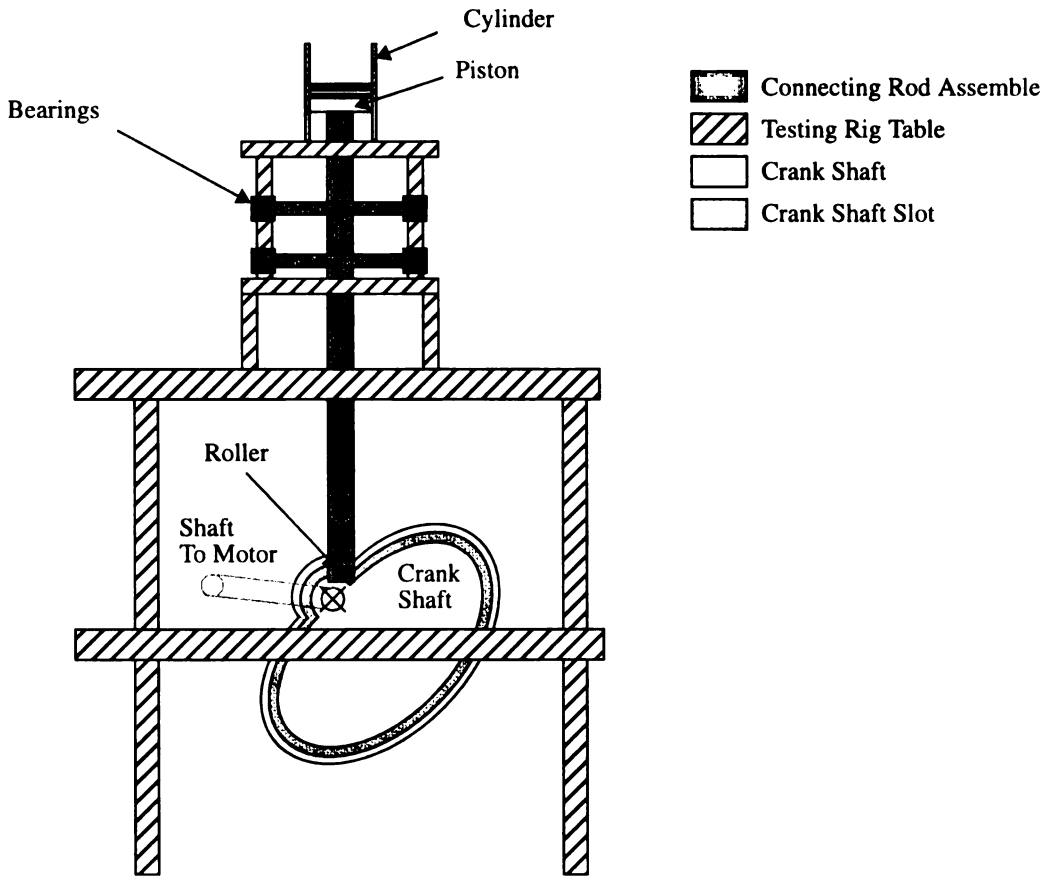

Figure 2b. Crank Shaft and Connecting Rod Assembly.

The piston was driven by a 2 HP DC motor, and the relative crank angle position was monitored by an optical encoder with the precision of one encoder pulse. The encoder output count was 360 per revolution for the flow visualization, and later with MTV it was made to be 720 per revolution through a gearing change. Since a four stroke engine goes through 720 degrees to complete one cycle and this model only goes through 360, the

crank angle position had a maximum error of 1 degree for the MTV results, and 2 degrees for the flow visualization results. Since the encoder output was a continuous series of pulses, the absolute position of the crank angle measurement was located with the addition of a secondary output of one pulse per revolution, which was used as a reference pulse located 10 degrees before TDC.

Water was used as the working fluid in the model for two main reasons. First, since geometric similitude was held between the model and a typical engine dimensions, characteristic lengths are the same, so the velocity for the model engine scales as a ratio of the kinematic viscosities between air and water for the same Reynolds number of a motored engine using air as its working fluid. This results in a velocity, RPM, and valve forcing frequency that scale to be 17 times larger than in air, so much lower speeds are required for a reasonable air equivalent RPM, and the shaker which created the valve motion had a much greater span of frequencies to excite the flow. The other reason for using water in the model was the ease of seeding the fluid for flow visualization and for the introduction of the chemicals required for MTV to generate the phosphorescence which convects with the tagged flow.

2.2. Flow Visualization Set-up

Flow visualization was carried out to examine the qualitative effects of exciting the flow through this method. The flow visualization utilized silver-coated hollow glass spheres to seed the flow. Their size ranged from 10 to 12 microns, and were illuminated with a Lexel Model 95 argon ion laser at 1.0 W. The image acquisition consisted of a NEC CCD

camera with an exposure time of 1/60 second and a Nikkor 50mm f1.2 lens, as well as a Data Translations DT3851 frame grabber, that is capable of storing 8 megabytes of images to memory which was sufficient to capture interlaced imaged as 30 frames per second over the time of the intake stroke. An A/D converter (ComputerBoards CIO-DIO24) simultaneously acquired the valve position from the LVDT and the crank angle position from an encoder mounted to the crank shaft. The optics consisted of a 1000 mm spherical lens to focus the beam and a 80 mm cylindrical lens to form a diverging plane of laser light. The flow visualization was carried out for a tumble plane through the cylinders vertical axis with a field of view which starts from the top of the cylinder to mid stroke, and horizontally 10 mm from the center of the cylinder out to the cylinder wall, as shown below:

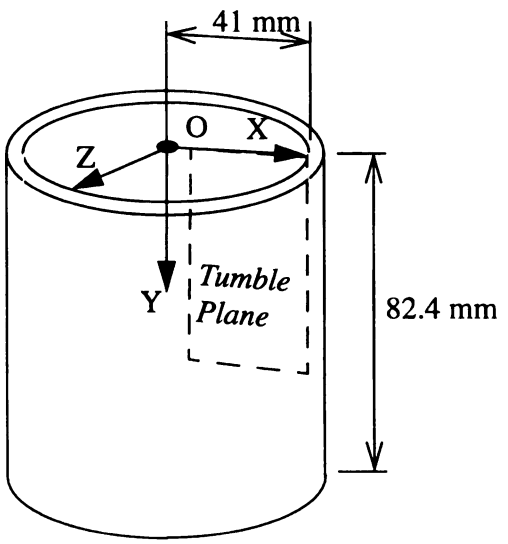

All of the following excitation conditions were examined with flow visualization:

Table 1: Forcing Conditions Examined with Flow Visualization

RPM	*Amp. (mm)*	*Freq. (Hz)*	*Duration (CA)*
170	0.35, 0.50, 1.00	10, 20, 30, 40, 50, 60	0-180
170	0.35, 1.00	10, 20, 30, 40, 50, 60	40-180
340	0.35, 0.50, 1.00	10, 20, 30, 40, 50, 60	0-180, 40-180, 60-180
340	0.35	70, 80, 90	40-180, 60-180, 0-18, 0-60
340	1.00	10, 20, 30, 40, 50, 60	0-18, 0-60

2.3 MTV Set-Up

Molecular Tagging Velocimetry, MTV, uses a working build which is pre-mixed with molecules with long-lived luminescence. A pulsed laser is used to tag the flow in the regions of interest, and the regions are imaged at two successive times within the luminescence lifetime. The measured Lagrangian displacement vector and the time over which the displacement occurred provides the estimate of the velocity vector. For measuring two components of the velocity, the intensity field of the tagged regions must have spacial gradients in two, preferably orthogonal, directions. For a multi-point velocity measurement, this is done by producing a grid of intersecting laser lines.

For MTV, a Lambda Physik LPX 200i UV (308 nm) laser operating at approximately 155 mJ (18 kV) provided the energy to generate phosphorescence from a working fluid mixture of 3.0 L of de-ionized water, 15.5 mL of CycOH, 0.78 gm CD, and saturated with BrNp. This required the use of a quartz piston and cylinder for the transmittance of the

UV light. By using laser beam blockers to create a series of alternating thick and thin laser lines, a nearly perpendicular grid pattern was imposed on the flow by generating one series of laser lines through the bottom of the piston, and a second series of lines directed through the cylinder, see Figure 3a,b.

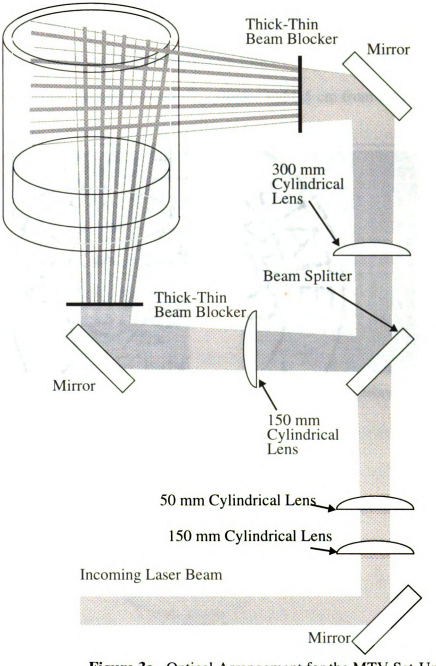

Figure 3a. Optical Arrangement for the MTV Set-Up.

Figure 3a shows the optical arrangement. The laser beam was focused using a combination of two cylindrical lenses with focal lengths of 150mm and 50 mm. A beam splitter was then used divide the beam in two. The divergence of each beam was then adjusted with additional cylindrical lenses, one 300 mm lens for the vertical set of bea and a 150 mm lens for the horizontal beam. Beam blockers fabricated from metal plates with a series of thin lines cut through them were placed in each beam path to generate a series of 12 to 13 lines. The MTV experiments were done with a field of view approximately 6cm x 6cm, located 22 mm below the top of the cylinder and 0.5 cm from the cylinder wall, see Figure 3b.

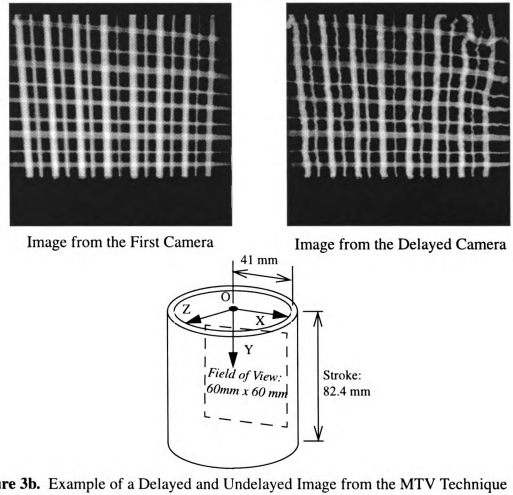

Figure 3b. Example of a Delayed and Undelayed Image from the MTV Technique and the Field of View within the Cylinder.
(images shown contain optical distortion from the cylinder)

Two Pulnix non-interlaced cameras with a 0.25 msec shutter speed and Nikkor 50 mm f1.2 lenses viewed the same region of the flow through a beam splitter. A video signal generator created horizontal and vertical drive inputs for the two cameras, and the vertical drive pulse was the source for the synchronization of the two cameras, the A/D acquisition, and the laser pulse triggering. The laser was triggered early enough (15.0961 msec) relative to the first camera's vertical drive such that the fluorescence range of the emission would disappear (1μsec after the occurrence of the peak intensity), and only phosphorescence would exist. Digital delay generators were used to delay the first camera relative to the laser firing time, and delayed the second camera relative to the first camera by 2.0226 msec which would provide approximately 5 to 10 pixels of displacement of the phosphorescent grid lines. See Figure 3b for an example of an image from each camera.

The image acquisition system was a Trapix Plus. The Trapix Plus is a real time image acquisition system capable of storing up to 8 gigabytes of continuous 8 bit 512k by 512k images from the two camera arrangement. The crank angle data was acquired in the same manner as the flow visualization experiments using a ComputerBoards CIO-DIO24. The framing rate from the Pulnix cameras was free running at a rate of 1/30 sec (approximately every 4 crank angle degrees) throughout the duration of the intake stroke and the DC motor driving the piston was also free running, but at a varying rate since the speed of the motor would drift slightly. Therefore the image acquisition was not phase locked to the crank angle position, and the image acquisition would not occur at the same crank angle locations throughout the stroke, even if the first image always occurred at the same location. The absolute crank angle position was monitored by from the encoder with the

A/D board, and was used to gate the initiation of the image acquisition. The onset of the image acquisition would have the Trapix Plus computer trigger data collection from the crank angle encoder each time a frame was acquired. As an attempt to increase the number of common crank angle positions between cycles, the cycles were only accepted if the crank angle position of the first image was at -1 to 1 degrees (from TDC). All data acquired with MTV were at 340 RPM and 35 engine cycles of each case.

The following forcing cases were acquired with the MTV method:

Table 2: Forcing Conditions Examined with MTV

RPM	*Amp. (mm)*	*Freq. (Hz)*	*Duration (CA)*
340	1.00	20, 30, 40, 50, 60	0-180
340	0.35	40, 60	0-180
340	0.35, 1.00	40, 60	40-180
340	0.35	40, 60, 90	0-18, 0-60
340	1.00	40, 60	0-18, 0-60

2.4 MTV Data Reduction

The MTV data consisting of pairs of images of original laser grid lines and distorted grid lines (see Figure 3b) were reduced to instantaneous velocity fields with the process developed by Gendrich and Koochesfahani [1]. This process correlates specified source regions of the original image with roam regions of the distorted image to determine the

displacement with sub-pixel accuracy. To achieve a high correlation, the source region should have distinctive patterns present that are unique within the roam region, such as a laser grid intersection. This requires that the delay time between the cameras be short enough that the laser intersections don't displace to the location where a different intersection was originally located. In this experiment, the intersections were 45 to 50 pixels apart, and the maximum pixel displacements were near 10 to 12 pixels.

The coordinate system used for the velocity fields had it origin, O, at the top and center of the cylinder, see below in Figure 3c:

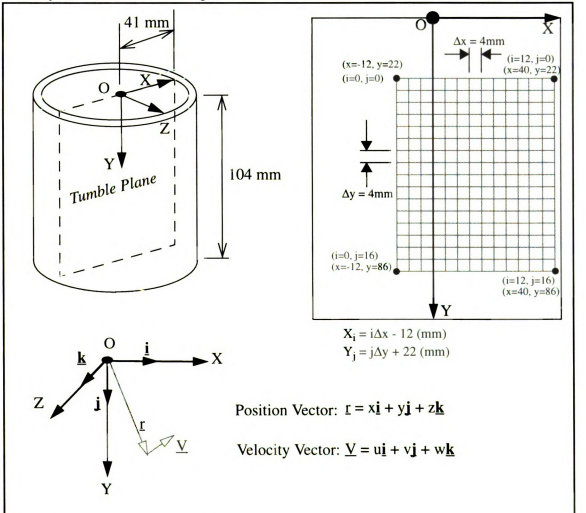

Figure 3c. Coordinate System and Data Locations within the Cylinder

The original velocity vectors had an irregular grid spacing that averaged 4.6 mm, and were re-mapped on a regular grid of 4mm by 4 mm within the region of the non-regular data by using linear interpolation. The range over which data were collected was from -16 mm $\leq x \leq$ 40 mm or from -12 mm $\leq x \leq$ 40 mm (depending on the data set), and from 22 mm $\leq y \leq$ 86 mm. Data at x=40 mm was linearly interpolated from velocity data at x=36mm and the wall boundary condition at x=41mm. Different variables were calculated by approximating integrals as summations at these discrete points.

Ensemble averaging of data at common crank angle positions was carried out in the following manner. At a given crank angle position, a flow variable of interest at the k^{th} engine cycle , Ψ_k, can be represented by:

$$\Psi_k = \overline{\Psi} + \Psi'_k \qquad k = 1 \ldots N \tag{2.1}$$

where $\overline{\Psi}$ is the mean value at the given crank angle position, and Ψ'_k is the fluctuating component of the variable at the k^{th} engine cycle. The mean of Ψ for N engine cycles is given by:

$$\overline{\Psi} = \frac{1}{N} \sum_{k=1}^{N} (\Psi_k) \tag{2.2}$$

The root mean square of the fluctuating component of Ψ is:

$$\tilde{\Psi} = \sqrt{\left(\frac{1}{N-1} \sum_{k=1}^{N} (\Psi'_k)^2 \right)} = \sqrt{\left(\frac{1}{N-1} \sum_{k=1}^{N} (\Psi_k - \overline{\Psi})^2 \right)} \tag{2.3}$$

Equation 2.3 would require a data set to examined twice to calculate the RMS component, because knowledge of the mean is required before equation 2.3 can be evaluated. For computational purposes, an RMS expression was sought that would require a single evaluation of a data set. By expanding equation 2.3, and noting the mean of the fluctuating component $\overline{(\Psi')} = 0$, yields:

$$\tilde{\Psi} = \sqrt{\frac{N}{N-1}\cdot\overline{(\Psi-\bar{\Psi})^2}} = \sqrt{\frac{N}{N-1}\left(\overline{\Psi^2 - 2\Psi\bar{\Psi} + \bar{\Psi}^2}\right)} = \sqrt{\frac{N}{N-1}\left(\overline{\Psi^2} - \overline{2(\Psi+\Psi')\bar{\Psi}} + \overline{\bar{\Psi}^2}\right)} = \sqrt{\frac{N}{N-1}\left(\overline{\Psi^2} - \bar{\Psi}^2\right)} \qquad (2.4)$$

(the $\overline{2(\Psi+\Psi')\bar{\Psi}}$ term reduces to 0)

and re-expressing mean quantities in equation 2.4 as a summation as defined in equation 2.2 yields:

$$\tilde{\Psi} = \sqrt{\left(\left(\frac{1}{N-1}\sum_{k=1}^{N}\Psi_k^2\right) - \frac{N}{N-1}\left(\frac{1}{N}\sum_{k=1}^{N}\Psi_k\right)^2\right)} \qquad (2.5)$$

Thus, equation 2.5 requires only one evaluation of a data set to calculate the mean and the mean of the squares of Ψ_k for the RMS calculation. From the 35 instantaneous velocity fields, the mean and the RMS values of the vorticity, circulation, kinetic energy, and tumble ratio were calculated.

The z-component of vorticity at the spacial location (x_i=i•Δx-.012, y_j=j•Δy-.022) is:

Vorticity:

$$(\omega_z)_{i,j} = \frac{\partial v}{\partial x} - \frac{\partial u}{\partial y} = \left(\frac{v_{(i+1,j)}}{2\Delta x} - \frac{v_{(i-1,j)}}{2\Delta x}\right) - \left(\frac{u_{(i,j+1)}}{2\Delta y} - \frac{u_{(i,j-1)}}{2\Delta y}\right) \begin{cases} \text{i=0 to 12,} \\ \text{j=0 to 16} \end{cases} \qquad (2.6)$$

The gradients in the vorticity were calculated, as shown, from a first order finite difference method. The i and j indices represent the x and y grid locations of the vorticity, so

each (i,j) pair represents a single point in the grid of data (i.e. $\omega_{ij} = \omega(x_i, y_j)$, where $x_i = i \bullet \Delta x - 0.012$ and $y_j = j \bullet \Delta y - 0.022$, See Figure 3c). The ΔA term is the differential area or sub-division of the regular grid of 4mm by 4mm, so $dA = \Delta x \bullet \Delta y = 16\ mm^2$. The circulation could then be calculated as follows:

Circulation:

$$\Gamma = \int_A (\omega_z) dA \approx \Delta A \sum_{i,j} (\omega_z)_{ij} \quad \begin{cases} \text{i=3 to 10,} \\ \text{j=1 to 15} \end{cases} \tag{2.7}$$

Ensemble averaging the circulation from multiple engine cycles leads to mean and the RMS components of circulation, which were calculated from the relations:

Mean and RMS Circulation:

$$\bar{\Gamma} = \frac{1}{N} \sum_{k=1}^{N} \Gamma_k \qquad \tilde{\Gamma} = \sqrt{\left(\left(\frac{1}{N} \sum_{k=1}^{N} \Gamma_k^2 \right) - \left(\frac{N}{N-1} \cdot \bar{\Gamma}^2 \right) \right)} \tag{2.8}$$

where N is the number of engine cycles, and k refers to the k^{th} cycle in the average.

The kinetic energy per unit mass in its general form is:

Kinetic Energy:

$$KE = \frac{1}{V} \int_V \frac{1}{2} (u^2 + v^2) dV \approx \frac{\sum_{i,j} x_i (u^2 + v^2)_{ij}}{(j_{max} - j_{min}) \cdot (i_{max} - i_{min})^2} \quad \begin{cases} \text{i=3 to 10,} \\ \text{j=1 to 15} \end{cases} \tag{2.9}$$

The dV term is the differential volume, where $dV = \Delta A(2\pi x_i) = \Delta x \Delta y(2\pi x_i)$, and V is the total volume enclosed by the data, and $V = H(\pi R^2) = [(j_{max} - j_{min})\Delta y][\pi((i_{max} - i_{min})\Delta x)^2)]$. The ratio of $dV/(2V)$ is therefore $x_i/[(j_{max} - j_{min})(i_{max} - i_{min})]$.

The cycle averaged mean and RMS components of the kinetic energy were calculated as follows:

Mean and RMS Kinetic Energy:

$$\overline{KE} = \frac{1}{N}\sum_{k=1}^{N} KE_k \qquad \tilde{KE} = \sqrt{\left(\left(\frac{1}{N}\sum_{k=1}^{N} KE_k^2\right) - \left(\frac{N}{N-1}\cdot\overline{KE^2}\right)\right)} \tag{2.10}$$

where again, N is the number of engine cycles, and k refers to the k^{th} cycle in the average.

The tumble ratio for the x-y plane is the z-component of the angular momentum per unit mass of the flow, H_z, divided by the moment of inertia of the fluid about the z-axis, I_{zz}, normalized by the angular speed of the crank shaft, Ω. It is developed as follows:

Tumble Ratio:

$$T_Z = \frac{H_Z}{I_Z \cdot \Omega} \tag{2.11}$$

The angular speed of the crank shaft is $\Omega = 2\pi(\text{RPM})/60$, and the z-components of the angular momentum per unit mass, H_z, and moment of inertia, I_{zz}, are defined as:

Angular Momentum, H
Moment of Inertia, I

$$H_z = \int_V ((\underline{r}\times\underline{v})\cdot\underline{k})dV \qquad I_{zz} = \int_V |\underline{r}\times\underline{k}|^2 dV \tag{2.12}$$

where $\underline{\mathbf{k}}$ is the unit vector in the z-direction. Expanding the expression $\underline{r}\times\underline{v}$ in the angular momentum, H_z. yields:

$$[\underline{r}\times\underline{v}]\bullet\underline{\mathbf{k}} = [(x\underline{\mathbf{i}} + y\underline{\mathbf{j}} + z\underline{\mathbf{k}}) \times (u\underline{\mathbf{i}} + v\underline{\mathbf{j}} + w\underline{\mathbf{k}})] \bullet \underline{\mathbf{k}} = xv - yu \tag{2.13}$$

and evaluating the cross product in the moment of inertia, I_{zz} yields:

$$|\underline{r}\times\underline{\mathbf{k}}|^2 = |(x\underline{\mathbf{i}} + y\underline{\mathbf{j}} + z\underline{\mathbf{k}}) \times \underline{\mathbf{k}}|^2 = |-y\underline{\mathbf{i}} + x\underline{\mathbf{j}}|^2 = x^2 + y^2 \tag{2.14}$$

Taking the results of equations 2.13 and 2.14, equation 2.12 can be re-written as

Angular Momentum, Hz
Moment of Inertia, Izz

$$H_Z = \int_V (xv - yu)dV \qquad I_{zz} = \int_V (x^2 + y^2)dV \tag{2.15}$$

Now the tumble ratio from equation 2.11 can be re-expressed in a summation form as follows:

Tumble Ratio:

$$T_Z = \frac{\int_V (xv - yu)dV}{\Omega \cdot \int_V (x^2 + y^2)dV} \approx \frac{\sum_{i,j}\{(x_i)v_{i,j} + (y_j)u_{i,j}\}}{\Omega \cdot \sum_{i,j}\{(x_i)^2 + (y_j)^2\}} \quad \begin{cases} \text{i=3 to 10,} \\ \text{j=1 to 15} \end{cases} \tag{2.16}$$

In equation 2.16, the Ω term refers to the angular speed of the crank shaft as in equation 2.11. The differential volume, $dV = (2\pi x_i)\Delta A = (2\pi x_i)\Delta x \Delta y$, appears in the cancels from the numerator and denominator.

With the definition of T_z from equation 2.16, the tumble ratio was ensemble averaged over N engine cycles to calculate mean and RMS expressions as shown in equation 2.17:

Mean and RMS Tumble Ratio:

$$\overline{T_Z} = \frac{1}{N}\sum_{k=1}^{N}(T_Z)_k \qquad \tilde{T_Z} = \sqrt{\left(\left(\frac{1}{N}\sum_{k=1}^{N}(Tz)_k^2\right) - \left(\frac{N}{N-1}\cdot\overline{Tz^2}\right)\right)} \tag{2.17}$$

2.4.1 Optical Distortions - Correction Method 1

The curvature of the cylinder causes distortion of the images; the distortion becomes progressively larger towards the cylinder's edge. To measure the distortion, a target with a printed grid of 1 mm spacing was placed inside the cylinder before the image acquisition

took place. This allowed for a mapping from pixel locations to actual locations within the cylinder. The mapping of the target lines to pixel locations was done by locating the pixel location for the peak intensity at each target line within integer pixel accuracy. In the y-direction, the pixel per mm ratio was found to vary by less than one pixel/mm, so it was assumed to be constant. The x-direction had a non-linear relationship, see Figure 4C.

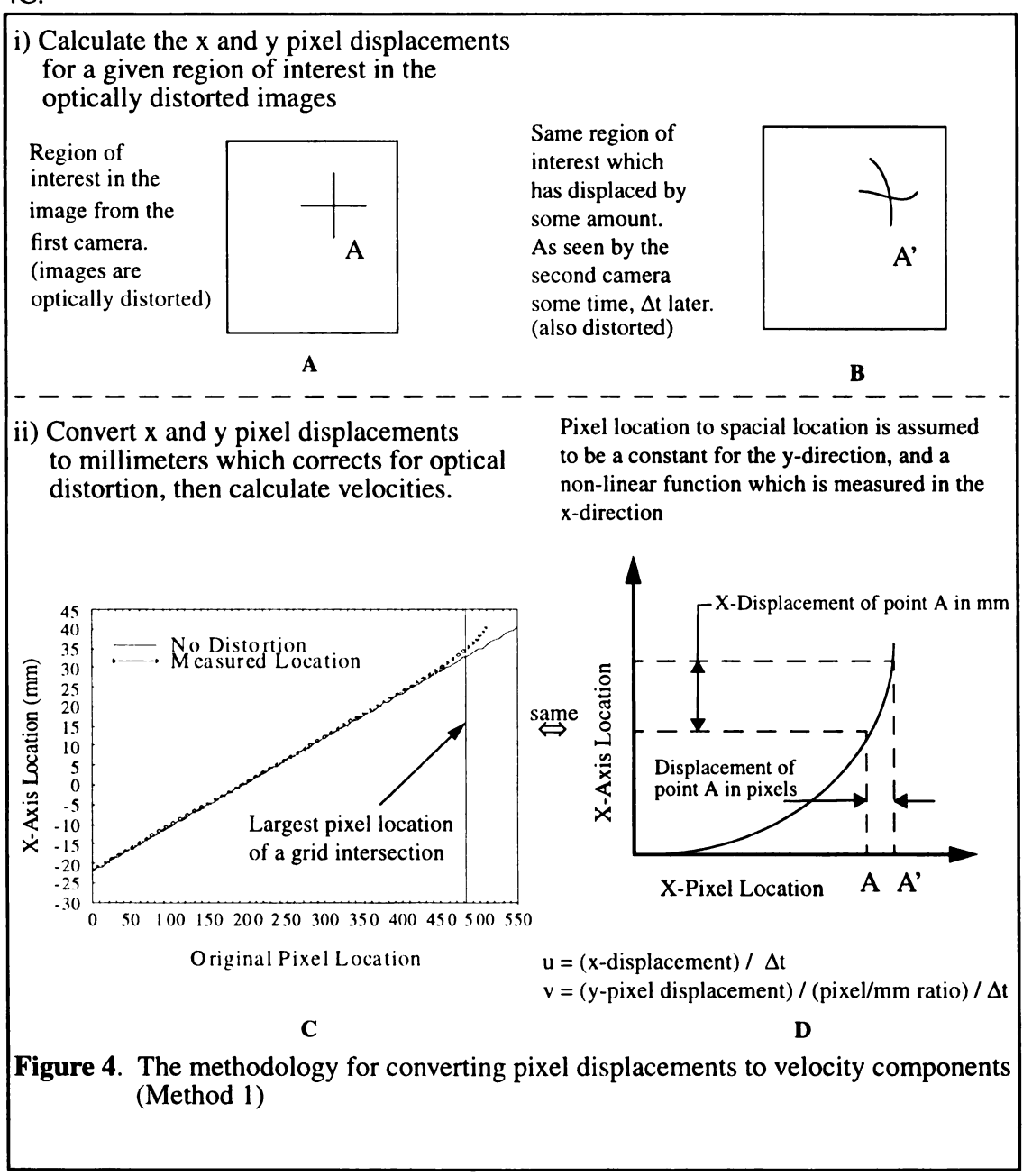

Figure 4. The methodology for converting pixel displacements to velocity components (Method 1)

In this method of correcting for the distortion, first the instantaneous x and y displacements from a pair of *distorted images* is measured in pixels, see Figure 4 A,B. Next the two pixel locations corresponding to a displacement are converted to spacial locations through the pixel to spacial mapping (Figure 4C,D), which corrects for the cylinders distortion. The two spacial locations are then used to calculate a new displacement and velocity. This correction method was used for the data presented in the Results section.

2.4.2 Optical Distortions - Correction Method 2

Another distortion correction approach would be to first re-map the images themselves into undistorted images. Pixel displacements calculated from the pairs of undistorted images could then be converted directly to millimeters with a constant pixel to millimeter ratio, see Figure 5. This approach would produce more accuracy, since the sub-pixel displacement calculations would not be affected by the intensity variations from the optical distortions. The downside to this approach is the increased computational time to redistribute the intensities of each image in a way that conserves the total intensity present and removes the cylinders optical distortion.

Since the optical distortion does not change the amount of light in the image, the total intensity contained within a distorted image should be the same as its corresponding corrected image after the re-mapping has be done. In the case of the cylinder's distortion, the distorted image is compressed in the x-direction, so during its re-mapping process, the total intensity of the image will be redistributed over a larger area (since the width of the corrected image will be larger). So the re-mapping process of the images will

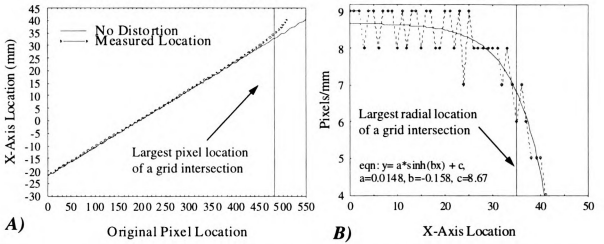

i) measure the pixel to actual location in the cylinder. This provides a direct pixel to spacial mapping, and its derivative provides a pixel/mm relationship across the radius of the cylinder.

ii) Calculate the pixel re-mapping required to correct for the distortion. The re-mapped pixel values are calculated from a constant pixel per mm ratio and the pixels spacial locations in Figure A.

The line labeled "No Distortion" is a one-to-one mapping that would occur if there were no optical distortions.

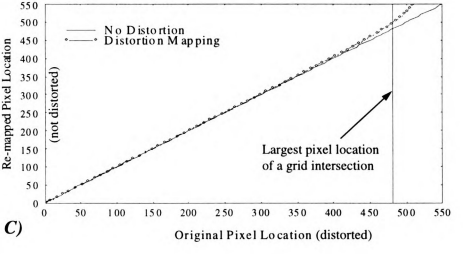

iii) Re-map the pixel locations of original images based on the function in Figure C, resulting in an image which closely appear as if it were acquired without the cylinder present. See Figure D for an example pair of images. (Total intensity in the image is not held constant when re-mapped, in this case.)

The resulting pixel displacements and the delay time between the cameras, are then used to calculate velocity

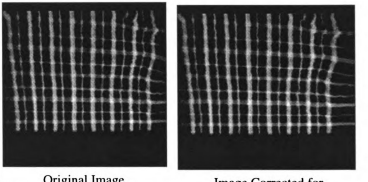

Figure 5. Method for Distortion Correction by Correcting the Images Directly (Method 2).
A,B) Optical distortion present in the images due to the curvature of the cylinder.
C) Re-mapping function used to adjust for the optical distortions.
D) An example of a distorted and a corrected image.

decrease the signal to noise ratio of the images, which would introduce some new error into their displacement calculations.

A comparison of these methods was done at a crank angle of 120 degrees, f = 60 Hz, A = 0.35 mm, and Δ = 0-18 crank angle degrees, see Table 3 for a summary of the results. In this comparison the re-mapping did not conserve the total amount of intensity. The re-mapping would first relocate the intensities of two adjacent pixels from the distorted image to new locations in the corrected image, based on Figure 5a. Next, if the two new pixel locations were not adjacent, then their intensities were used to linearly interpolate for any intermediate pixel location intensity values. Figure 5d shows a distorted image and its corresponding image which has been corrected in this manner. By not conserving the total intensity in the corrected image, the signal to noise ratio was not changed, so it is not a factor in the results in Table 3.

Table 3: Comparison of Cylinder Distortion Correction Techniques (% Change from Method 1 to Method 2)

Parameter	% Change* in Mean Value	% Change* in RMS Value
Circulation	0.955	5.61
Tumble Ratio	-4.31	-4.83
Kinetic Energy	8.42	9.72
Minimum Vorticity	-1.07	-
Maximum Vorticity	-6.80	-

* % Change = 100 x ($\text{Parameter}_{(\text{Method 1})}$ - $\text{Parameter}_{(\text{Method2})}$)/$\text{Parameter}_{(\text{Method1})}$

The results in Table 3 show a fairly small change in mean values of the given parameters,

a larger change in the RMS values. This would be expected since the distortion is only significant at the edge of the cylinder, and effects only a small portion of the data set. As a result, the use of the Method 1 for the correction of the optical distortion from the cylinder was seen as an approach with acceptable results

Chapter 3

RESULTS AND DISCUSSION

The organization of the flow visualization and MTV experiments was done in a way to attempt to isolate the effects, if any, of the valve forcing parameters on the development of the flow. The valve excitation parameters were the peak to peak amplitude(A), the excitation frequency(f), and the duration of the intake stroke when the excitation is active(Δ). Flow visualization was performed at two speeds, 170 and 340 RPM, but the main focus was on the 340 RPM speed because it is closer to a true operating engine speed. The only discussion of 170 RPM flow visualization data will be contained in §3.1 to demonstrate some of the flow features observed in the flow visualization.

The intake stroke was the focus of the study (i.e. CA range of 0-180 degrees), but in some of the flow visualization data sets, data are shown through 210 degrees (referenced to TDC of intake). This was done since there was interest in the resulting flow structures at the end of the stroke, and very little linear piston displacement has occurred between 180 and 210 degrees, so it is similar to the beginning of the compression stroke, even though the valve is open. The MTV data sets cover the intake range of 90-180 crank angle degrees, which focuses on the end of the intake stroke as well.

Due to the number of pages of images and plots referred to in the results sections, the flow visualization figures will be located at the end of the flow visualization discussion (after section §3.1.3 Effects of the Duration of the Excitation - Flow Visualization), and

the MTV figures will be located after the CONCLUSIONS in Chapter 4 (Figures start on page 57).

3.1 Flow Visualization Results

In general, the main feature that could be observed to change in the flow was the size and strength of the main vortex, especially near the end of the stroke, which was used as the main qualitative comparator between the various forcing cases. However, other characteristics were noticed when the flow was excited. One flow feature which was greatly changed was the inclination angle of the intake annular jet as it entered the cylinder. In comparing Figure 6A and 6B at 170 RPM, the change in the inclination angle of the intake annular jet can be observed with the excitation of: f = 40 Hz, A = 1.00 mm, and Δ = 0-180 degrees. Initially, at CA = 30 degrees, the inclination angle is smaller (if measured from the horizontal), and later becomes larger compared to the unperturbed case at CA = 60 degrees. Another flow feature observed was the near absence of large scale formations in the flow, as seen in Figure 6C, but that occurred at only one combination of excitation conditions (f = 60 Hz, A = 1.00 mm, and Δ = 0-180 degrees). It is possible the flow has became very three dimensional in this case and may have large scale motions in the swirl plane, but it is not certain if that is true.

The effects of the forcing parameters (Amplitude, Frequency, and Duration) on the development of the large main vortex at an engine speed of 340 RPM are described in detail in the next three sections (§3.1.1 through §3.1.3).

3.1.1 Amplitude effects - Flow Visualization

The amplitudes used were 0.35 mm, 0.50, and 1.00 mm. Since 0.35 mm was the smallest reliable amplitude produced with the valve-shaker apparatus, it was hoped that this would be small enough to have no effect on the bulk flow so that gradual changes in the bulk flow could be observed with increasing amplitude. See Figures 7, 8, and 9 for the effect of amplitude and frequency at CA = 180 degrees. The amplitudes of 0.35 mm and 1.00 mm intensified the main vortex formation when excited at 30, 40 and 60 Hz for many of the cases, see Figures 7, 8, and 9, so the minimum amplitude threshold was never found.

In Figure 7 (Δ=0-180), comparing amplitude effects, the amplitude of 0.35 mm appears to have higher vorticity levels at all forcing frequencies, with the possible exception of 50 Hz, which in either case is similar to that of no excitation. The same tends are also seen in Figures 8 (Δ=0-60) and 9 (Δ=0-18). Some exceptions to this trend can be seen in Figures 8b,h (20 Hz) and Figures 9d,j (40 Hz), where A=1.00mm appears to be causing more large scale motions than A= 0.35mm. In most cases though, A=0.35mm appears to have amplified the large scale motions more than the amplitude of 1.00 mm.

Figures 11 (A=0.35mm) and 12 (A=1.00mm), show the amplitude effect through the entire intake stroke with f=40Hz and Δ=0-180 degrees. When comparing these in the early part of the intake stroke (CA:40-80 degrees), the large scale vortices appear stronger with the lower amplitude (Figure 11), but they also are also about the same as the unperturbed case in Figure 10. When comparing these in the later part of the intake stroke (CA:150-200 degrees), the 0.35mm amplitude (Figure 11) is much stronger than

both the 1.00mm amplitude (Figure 12) and the natural case (Figure 10).

The forcing configurations of:

i) A=1.0mm, f=30Hz, Δ=0-180 degrees (Figure 7i),

ii) A=0.35mm, f=60Hz, Δ=0-60 degrees (Figure 8f), and

iii) A=0.35mm, f=60Hz, Δ=0-18 degrees (Figure 9f)

had the most favorable effects on the formation of large vortex structures in the tumble plane. These three best cases show that the smallest and largest amplitudes chosen have an effect on the development of the turbulence, and the smallest amplitude has just as much if not more of an effect at later crank angles than the largest amplitude. Part of this could be due to the oscillating valve motion generating a circulation pattern in the opposite directions that the intake flow causes, and this effect starts to counteract the benefits of the pertubation at the large amplitudes. This is supported by the case of 170 RPM, f=60Hz, A=1.00mm, and Δ=0-180 degrees greatly attenuated the large scale motions (Figure 6C), and this was the case of the maximum amplitude at its maximum frequency, which would cause the strongest opposing recirculation pattern. The same effect can be seen to some degree at 340 RPM with f=60Hz, A=1.00mm, and Δ=0-180 in Figure 13 from CA: 20-60.

The 0.50 mm amplitude was excluded from the MTV analysis of the flow. Since the minimum required amplitude to create substantial changes in the bulk flow had not been found, it was decided for MTV to only analyze the smallest and largest amplitudes (0.35 and 1.00mm) with MTV since the flow visualization results showed the most amplification of the large vortex formations.

3.1.2 Frequency Effects - Flow Visualization

Varying the frequency in 10 Hz increments had an effect on the flow in each case to some minor degree at least, see Figures 7, 8, and 9. The preferred forcing frequencies seemed to be at 30 or 40 Hz and 60 Hz. The most dramatic results came at these frequencies, but not at all amplitudes or durations of excitation. Comparing Figures 12, and 13 show an attenuation effect of the vorticity during 130 to 180 degrees crank angle, when the frequency changed from 40 Hz to 60 Hz (A=1.00mm, Δ=0-180 degrees). On the other hand, comparing Figures 14 and 15 show an amplification of vorticity when the frequency changed from 40 Hz to 60 Hz (A=0.35 mm, Δ=0-18 degrees). Figures 15 and 16 are two examples at 60 Hz, which were two of the best cases observed. These show that through the entire intake stroke, the main vortex formation is more concentrated and localized versus a larger and less intense vortex when no excitation is applied (Figure 10). Since 60 Hz was the maximum frequency that could be produced at an amplitude of 1.00 mm, the frequencies of 40 and 60 Hz were chosen the main focus in the MTV data to be ensemble averaged and compared to the natural case.

It should also be noted that a Strouhal number ($St_D=fD/U$) for the piston-cylinder configuration could be based on the mean velocity of the flow through the intake valve opening, the diameter of the intake valve and the forcing frequency. The mean velocity of the flow through the intake valve opening varies with the speed of the piston which is a function of the crank angle, so St_D would also vary as a function of crank angle. So if a constant St_D was desired, the forcing frequency would have to change as a function of the crank angle in a sinusoidal fashion ($f \propto U$; $U \propto sin(CA)$). The result of Tang and Ko [2] with the

maximum turbulence amplification of an excited coaxial jet occurring at St_D = 1.16, could be applied to the piston-cylinder geometry by approximated by applying a varying forcing frequency which starts the stroke at 0 Hz, reaches a maximum value of 36.3 Hz at 90 degrees, and goes back to 0 at 180 degrees. The diagram to describe this is shown below:

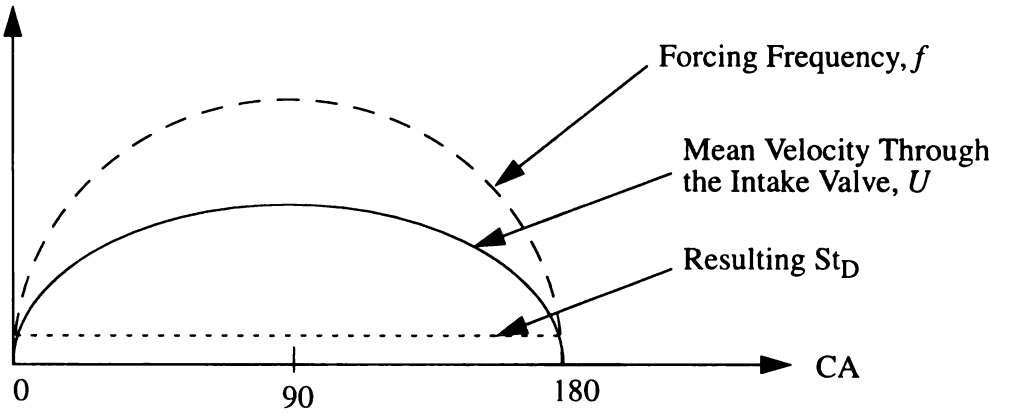

Data was not taken for any of those forcing frequency strategies, but it could provide more insight to the best approach for a forcing frequency condition.

3.1.3 Duration of Excitation - Flow Visualization

The duration of the intake stroke during which the excitation was active, Δ, had values of 0-180, 0-60, 0-18, 40-180, and 40-180 degrees. The 0-180 degree excitation was initially examined, and produced some of the strongest appearing turbulence near the end of the stroke. Exciting from 40-180 degrees had some similar results, but not as strong as the 0-180 degree results. Therefore, the exclusion of the excitation in the early portion of the stroke seemed to have a lesser effect on the vortex amplification. The question of how much does the early potion of the cycle affect the flow structures at the end of the stroke was investigated by looking at Δ = 0-18 and 0-60 degrees. With Δ of 0-18 and 0-60

degrees, A=0.35mm, and f=60Hz (Figures 8f, 9f, 15 and 16), had substantially larger tumble oriented vortex activity with the appearance of much more mixing occurring at the end of the stroke than any of the other durations. The same appeared but at lesser degrees when the amplitude was changed to 1.00 mm, or if the frequency was changed to 40 Hz. This shows that the excitation does not need to be on all of the time for the best results.

These results from varying Δ demonstrate that the early formations of the flow entering the cylinder have long term effects on the development of the large scale structures, and the results from the excitation during this period do not just dissipate once the excitation is turned off and the non-excited flow enters the cylinder.

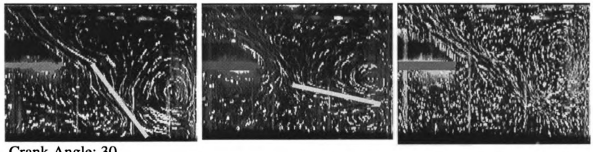

Crank Angle: 30

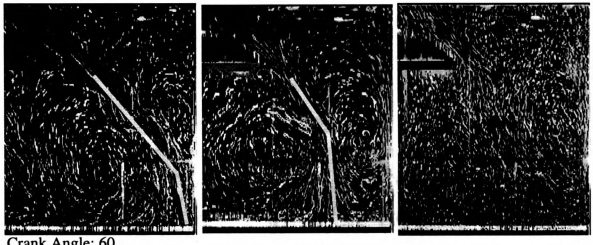

Crank Angle: 60

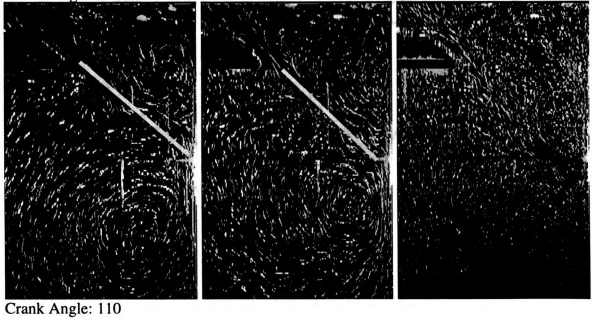

Crank Angle: 110

A) No Excitation

B) f = 40 Hz, A = 1.00 mm, Δ = 0-180 deg

C) f = 60 Hz, A = 1.00 mm, Δ = 0-180 deg

Figure 6. Flow Visualization at 170 RPM. (Note the change in the inclination angle at 40 Hz, and the lack of the formation of large scale structures at 60 Hz)

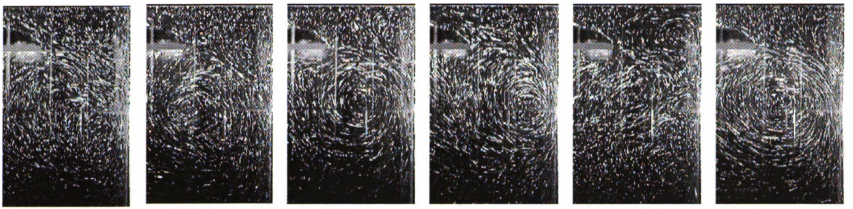

a) No Excitation b) 20 Hz c) 30 Hz d) 40 Hz e) 50 Hz f) 60 Hz

Valve Excitation: Amplitude: 0.35 mm, Duration: 0-180 degrees

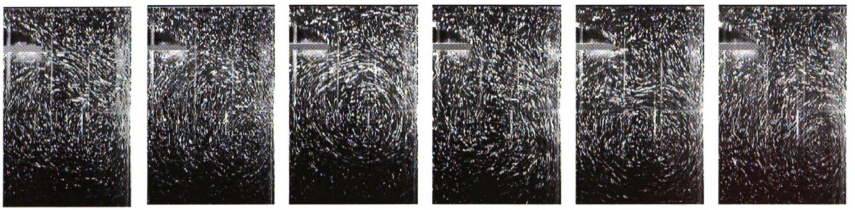

g) No Excitation h) 20 Hz i) 30 Hz j) 40 Hz k) 50 Hz l) 60 Hz

Valve Excitation: Amplitude: 1.00 mm, Duration: 0-180 degrees

Figure 7. Comparison of Flow Visualization at 180 Degrees Crank Angle.
RPM: 340, A: 0.35 and 1.00 mm, Δ: 0-180 degrees

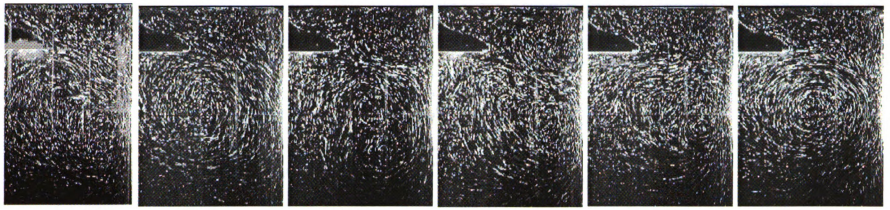

a) No Excitation b) 20 Hz c) 30 Hz d) 40 Hz e) 50 Hz f) 60 Hz

Valve Excitation: Amplitude: 0.35 mm, Duration: 0-18 degrees

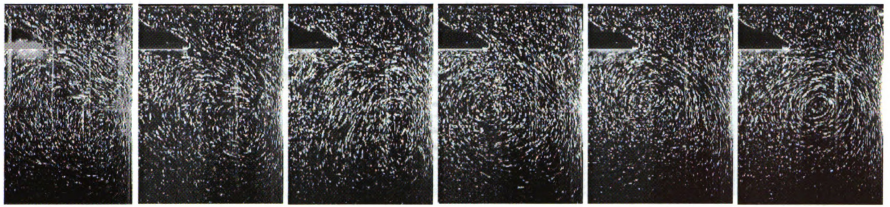

g) No Excitation h) 20 Hz i) 30 Hz j) 40 Hz k) 50 Hz l) 60 Hz

Valve Excitation: Amplitude: 1.00 mm, Duration: 0-18 degrees

Figure 9. Comparison of Flow Visualization at 180 Degrees Crank Angle.
RPM: 340, A: 0.35 and 1.00 mm, Δ: 0-18 degrees

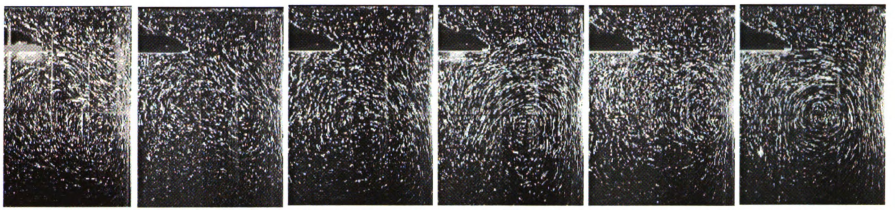

a) No Excitation b) 20 Hz c) 30 Hz d) 40 Hz e) 50 Hz f) 60 Hz

Valve Excitation: Amplitude: 0.35 mm, Duration: 0-60 degrees

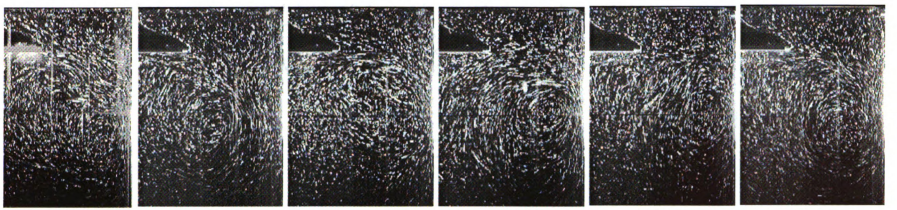

g) No Excitation h) 20 Hz i) 30 Hz j) 40 Hz k) 50 Hz l) 60 Hz

Valve Excitation: Amplitude: 1.00 mm, Duration: 0-60 degrees

Figure 8. Comparison of Flow Visualization at 180 Degrees Crank Angle.
RPM: 340, A: 0.35 and 1.00 mm, Δ: 0-60 degrees

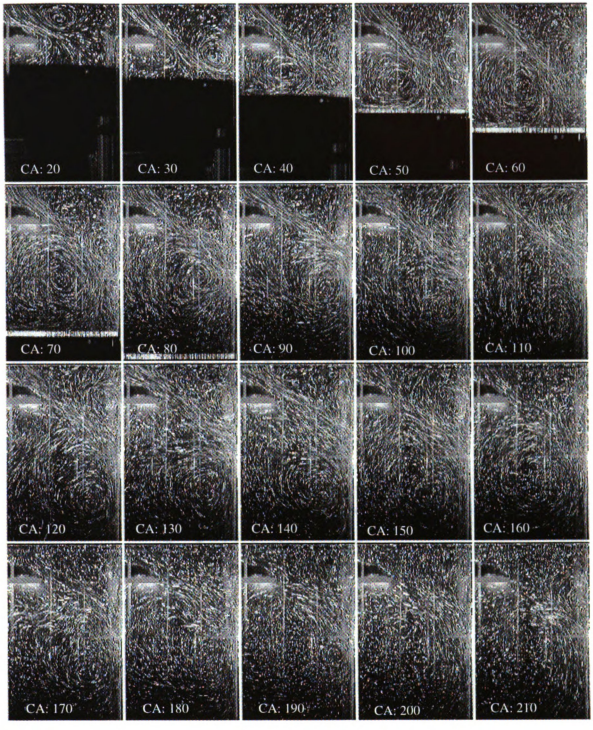

Figure 10. Flow Visualization with No Excitation

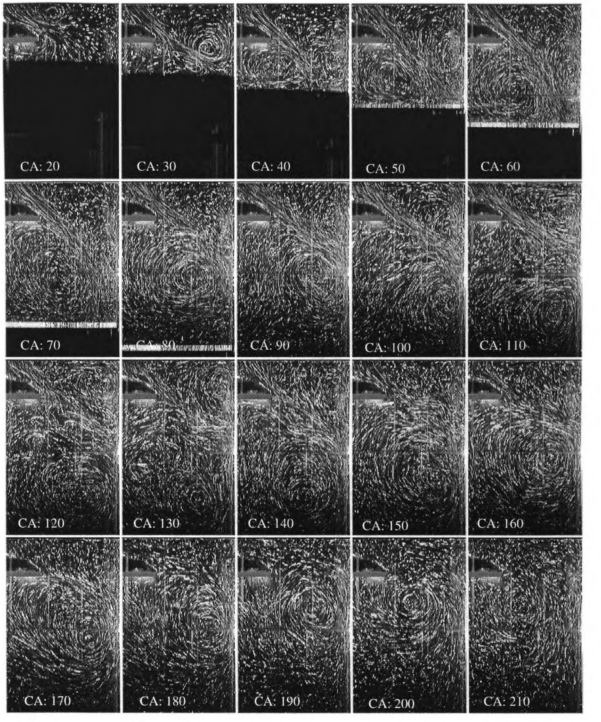

Figure 11. Flow Visualization with Excitation Conditions
f: 40 Hz *A*: 0.35 mm Δ: 0-180 degrees

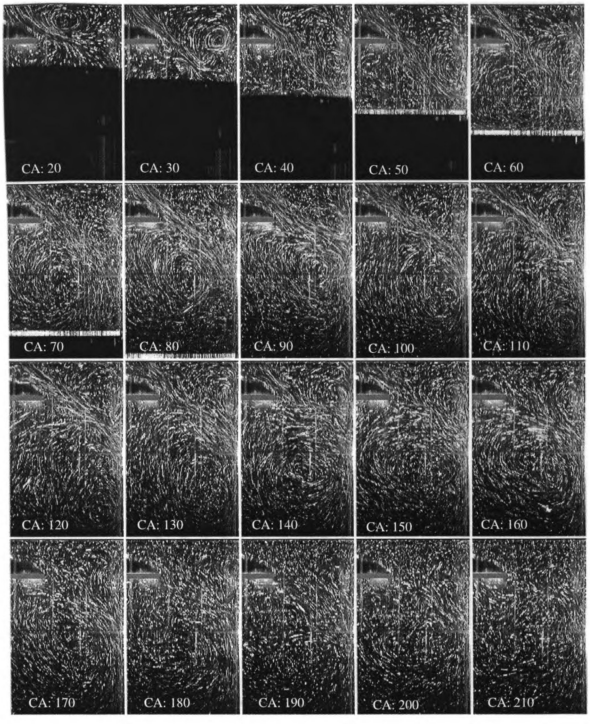

Figure 12. Flow Visualization with Excitation Conditions:
f: 40 Hz *A*: 1.00 mm Δ: 0-180 degrees

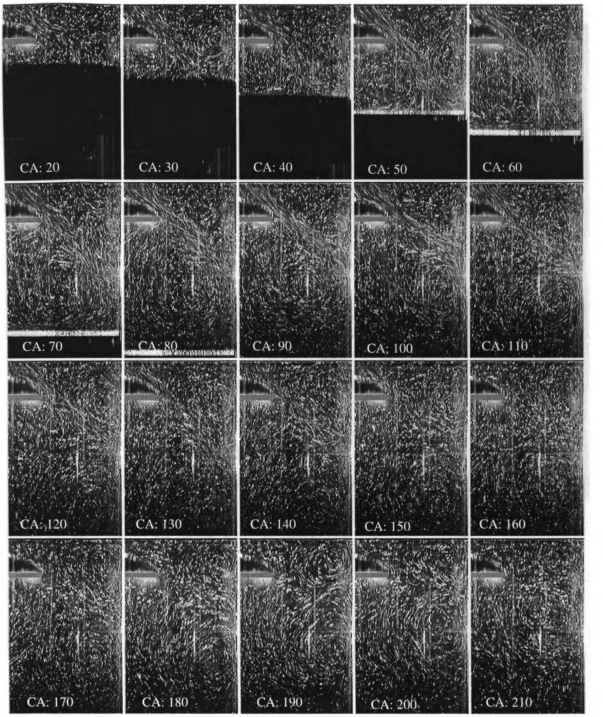

Figure 13. Flow Visualization ExcitationConditions:
f: 60 Hz *A*: 1.00 mm Δ: 0-180 degrees

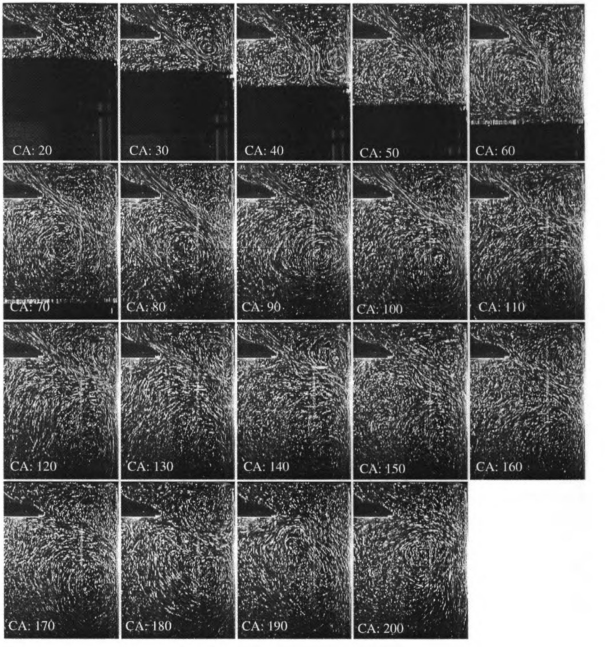

Figure 14. Flow Visualization Excitation Conditions:
f: 40 Hz *A*: 0.35 mm Δ: 0-18 degrees

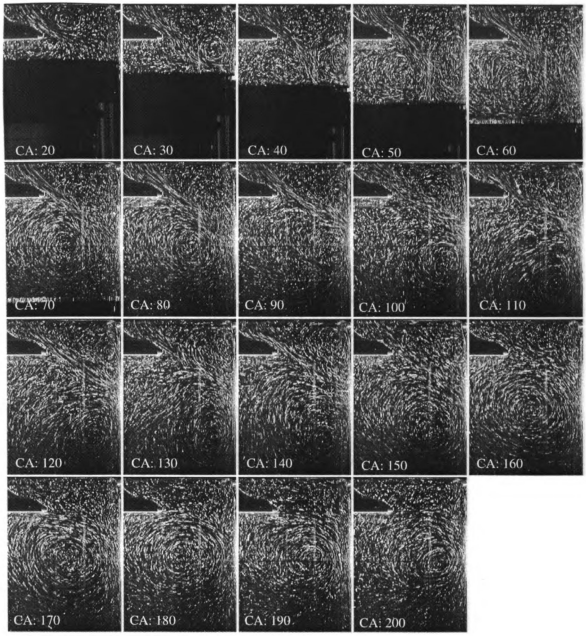

Figure 15. Flow Visualization with Excitation Conditions:
f: 60 Hz *A*: 0.35 mm Δ: 0-18 degrees

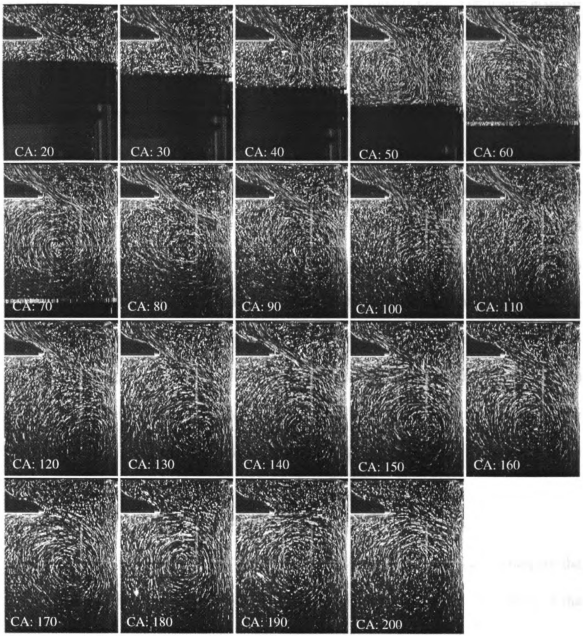

Figure 16. Flow Visualization with Excitation Conditions:
f: 60 Hz *A*: 0.35 mm Δ: 0-60 degrees

3.2 MTV Results

The MTV data were taken for 35 engine cycles of each forcing case. The image acquisition rate (frames/sec) and the crank angle rate (crank angles/sec) were an integer ratio of each other, but not phase locked with each other, so each crank angle was not sampled 35 times. The two rates would eventually become out of synchronization, resulting in some crank angle positions being skipped within in an engine cycle of data. The data were ensemble averaged at 10 degree increments from 90 to 180 degrees. The sample size was increased by allowing data to be averaged if it was within ±1 degree from the intended crank angle. This generated sample sizes which varied from 15 to 34 and on average was 25. The parameters calculated from the MTV data were the peak (maximum and minimum) vorticity levels, and the mean and RMS of the following: average vorticity, circulation, kinetic energy, and tumble ratio. In the region of the cylinder which the MTV data was taken, the main vortex region has a negative sign of vorticity. This means that a more negative value of circulation, average vorticity, or minimum vorticity indicates a favorable condition.

A discussion of the cycle averaged velocity and vorticity fields is done to compare the MTV results to the flow visualization results. For the examination of the effects of the forcing parameters (A, f, and Δ) the mean values of the circulation and the kinetic energy are used for the main comparators, and for easier comparison, the percent change in these parameters are looked at in detail. The other parameters which were calculated are found in Appendix C. Also, note that the MTV figures will be grouped after CONCLUSIONS section.

3.2.1 Cycle Averaged Velocity and Vorticity Fields

The cycle averaged velocity and vorticity fields corresponding to the flow visualization in Figures 10 through 16 can be found in Figures 17 through 23. All of the vorticity contours are plotted on the same scale from -120 sec^{-1} to 120 sec^{-1}, and the velocity vectors, which are on a 4mm by 4mm grid, all have the same length scale, so a visual comparison between Figures 17 through 23 is valid. The main vortex in the field of view in these figures has a negative sign of vorticity, so a more negative value indicates an increase in the vorticity.

When comparing Figure 17 (no excitation) and Figure 18 (A=1.00mm, f=40Hz, and Δ=0-180 degrees) over the range of CA=90-110 degrees, the annular intake jet's inclination angle is observed to be much steeper for the forced case. The forced case in Figure 18 has higher velocities and vorticity levels, than the natural case in Figure 17, and this could be due to the forced annular jet not loosing as much of its momentum from impinging on the cylinder wall because of its steeper inclination angle. Another feature in the forced case (Figure 18) is the center of the main vortex is approximately 4 mm closer to the center of the cylinder as compared to the unperturbed case (Figure 17). Through out the rest of the cycle, higher levels of vorticity can be seen at the core of the main vortex in the forced case.

In Figures 18 and 19, the amplitude changes from 0.35mm to 1.00mm, with f=40Hz and Δ=0-180 degrees. The amplitude of 1.00mm (Figure 19) shows higher vorticity over a larger region of space within the cylinder, and the inclination angle is steeper at CA=100

and 110 degrees. This effect of higher vorticity and velocities at 1.00mm was not observed in the flow visualization results of the same forcing cases in Figures 11 and 12, which showed the opposite trend for the same forcing conditions.

In Figures 19 and 20, the frequency was changed from 40 Hz to 60 Hz with A=1.00mm and Δ=0-180 degrees. Increasing to 60 Hz dramatically reduces the intensity of the vorticity throughout the cycle for this case. The annular intake jet has about the same inclination angle at CA=90 degrees, but the magnitude of the velocity vectors is smaller. The center of the vortex is approximately at the same radial location, but is about 2 to 3 mm lower than the 40 Hz case at CA=90 degrees, and at CA=180 degrees, it is about 10 mm lower. The 60 Hz case of Figure 20 has lower peak vorticity levels than the unperturbed case shown in Figure 17, while the 40 Hz case (Figure 19) has higher levels. These basically agree with the flow visualization in Figures 12 and 13, which show an attenuation of large scale motion at 60 Hz for this case.

Figures 21 through 23 are excited at A=0.35 and have short excitation durations of Δ=0-18 or 0-60 degrees. These have similar results which are large improvements over the natural case in Figure 17. Figure 23 (A=0.35mm, f=60Hz, and Δ=0-60 degrees) overall is the weakest of the three, while Figure 21 (A=0.35mm, f=40Hz, and Δ=0-18 degrees) and Figure 22 (A=0.35mm, f=60Hz, and Δ=0-18 degrees) are extremely similar, however, Figure 21 has slightly higher vorticity levels at CA=180 degrees. These results and the flow visualization results in Figures 15 and 16 agree very well. However, the case of A=0.35mm, f=40Hz, and Δ=0-18 degrees in Figures 14 and 21 do not concur, because

the flow visualization does not display much of a change from the unperturbed case, while the MTV results show a large change.

3.2.2 Effects of the Number of Cycles used to Ensemble Average

To examine the minimum number of cycles necessary for the convergence of the calculated variables, they were calculated starting with 5 samples and increasing by steps of 5 up to 25 samples, if available. This was done for the natural case and one of the forced cases, see Figures 24 through 27. The mean quantities of the values changed very little when the sample size was greater than 5 to 10 engine cycles. The RMS quantities started to converge after 15 engine cycles. Even though a larger sample size would be preferred for better accuracy of RMS quantities, the sample sizes used still show some convergence and should make meaningful comparisons. The scatter in the plots of Figures 24 through 27 is fairly consistent between the natural and excited cases. It was anticipated that the excited cases would have lower RMS values than the natural case due to the forced flow expecting to respond in a more consistent way due to the excitation, but that did not appear to take place.

3.2.3 Mean Circulation and Mean Kinetic Energy Results

Plots of the mean circulation and kinetic energy versus crank angle are shown in

- Figures 28 (A=0.35mm, f=40,60 Hz, Δ=0-180, 0-60, 0-18),
- Figure 29 (Same as Fig. 28, except A=1.00mm), and
- Figure 30 (A=1.00mm, f=20,30,40,60 Hz, Δ=0-180).

The mean kinetic energy drops from CA=90 to 110 degrees. This is due to the inclination

angle of the jet becoming smaller, which causes the annular intake jet to loose more energy as it impinges more directly into the cylinder wall and decreasing the magnitude of the velocity vectors. The mean kinetic energy starts to rise after 110 degrees because the upper region of the main vortex is entering the range where data was taken, and once the entire region of the main vortex is in the range of the data, the kinetic energy starts to decrease as the crank angle position goes from 140 to 180 degrees. The mean circulation plots show the same trends as the mean kinetic energy. Lower values of circulation represent high negative vorticity, due to the negative sign of vorticity for the large scale vortex in the field of view, so note that magnitudes of the mean circulation and kinetic energy increase at the same crank angles and decrease at the same crank angles.

In Figure 28 a clear grouping can be seen, where the cases with Δ=0-180 are similar to the unperturbed case, and the forcing cases of Δ=0-60 and 0-18 degrees have a clear increase in mean kinetic energy and mean circulation (*again note that "increase" refers to an increase in magnitude of these parameters; meaning the circulation has become more negative and the kinetic energy has become more positive*). When the amplitude is increased to 1.00mm, in Figure 29, the grouping observed in Figure 28 is no longer present, and a wider spread in the data is present. The strongest trend present is an increase in both the mean circulation and mean kinetic energy for cases with Δ=0-18 degrees.

Figure 30 shows the frequency effect for A=1.00mm and Δ=0-180 degrees. It shows that 40 Hz is the preferred forcing frequency (it generally has the largest magnitude of circu-

lation and kinetic energy), while 20 and 30 Hz cause little change and 60 Hz attenuates the mean circulation and kinetic energy.

3.2.4 Amplitude effects - MTV

The effects of amplitude from the MTV results corresponded to the results from the flow visualization, where the lowest amplitude had the highest levels of vorticity, see Figures 17, and 21 through 23. However, not all cases examined with the amplitude of 0.35mm produced higher levels of vorticity. For example, in Figure 19, the case of f=40Hz, A=0.35 mm, Δ=0-180 degrees, the resulting vorticity fields are very similar to the unforced case (Figure 17).

The percent change in mean circulation and mean kinetic energy between no excitation and cases with A=0.35mm is found in Figure 31, and the comparison of no excitation to cases with A=1.00mm is found in Figure 32. *Note that a positive percentage change represents an improvement for either the mean circulation or the mean kinetic energy.* In Figure 31, the forcing amplitude of 0.35 mm generally increased circulation and kinetic energy versus no excitation, except for the cases with Δ=0-180 which had little change. In Figure 32 with the forcing amplitude at 1.00mm, increases in these parameters versus no excitation appear to be dependent upon the other forcing parameters, because of the large spread in the data. The excitation duration of 0-18 degrees does the most amplification of these parameters overall with A=0.35mm.

Figure 33 shows the percent change in mean circulation and kinetic energy when the

amplitude is changed from 0.35mm to 1.00mm, and the other forcing parameters are held constant. Figure 33 confirms that increasing the amplitude to 1.00mm, decreases the mean circulation and kinetic energy, and the only case which shows an increase is f=40Hz and Δ=0-180. Since the smallest amplitude used in this study produced the most amplification, it is difficult to globally say which amplitude would do this best, but it does show that a small amount of energy introduced into the flow at the proper conditions will cause a resonance effect and amplify the disturbance. The best cases for amplification of circulation and kinetic energy with the amplitude of 0.35 mm had a 30% to 40% increase in mean circulation and kinetic energy at 180 degrees as compared to the natural case (see Figure 31).

3.2.5 Frequency Effects - MTV

The percent change in mean circulation and mean kinetic energy were examined at A=1.00mm and Δ=0-180 degrees with the following frequencies: 20, 30, 40, and 60 Hz. The results are displayed in Figure 34, which shows 40 Hz had the larest effect for increasing kinetic energy and circulation from CA=150-180 degrees. To examine the effects of 40 Hz, Figure 35 shows the change between no excitation and forcing cases at 40 Hz. A wide range of amplification is possible with 40 Hz, depending upon the amplitude and duration of the excitation. In general from CA=140-180 degrees, there was an increase in mean circulation and kinetic energy, which was largest at Δ=0-18 degrees.

The other forcing frequencies of 20 Hz and 30 Hz, in Figure 34, exhibited little change from the unperturbed state, while 60 Hz has an attenuation effect. However, other forcing

conditions at 60 Hz displayed amplifications as seen in Figure 31. Figure 36 shows the change of going from no excitation to pertubations that are at 60 Hz. At 60 Hz, a separation appears in the data where amplifications are only seen in the smaller amplitude and shorter excitation duration cases, and the other cases with higher amplitudes and longer durations attenuate the circulation and kinetic energy.

As observed in the flow visualization, increases in vorticity occur when the forcing is done with the shortest duration and the frequencies of 40 Hz and 60 Hz. To examine the differences between 40 Hz and 60 Hz forcing frequencies, Figure 37 displays the percent change in mean circulation and mean kinetic energy when the forcing frequency is increased from 40 to 60 Hz. When Δ=0-18 or A=0.35, the response of the flow seems to be insensitive to a change from 40 to 60 Hz, but if the amplitude is large (except when Δ=0-18), then 60 Hz produces less amplification than 40 Hz.

3.2.6 Duration of Excitation - MTV

The duration of the excitation is the most dominant parameter of the excitation along with the amplitude. In the comparisons from various excitation durations with the unforced case in Figures 35 and 36, Δ=0-180 is consistently attenuates the circulation and kinetic energy or has little change when compared to the other durations. Looking at CA=150-180 degrees in Figures 35A and 36A, the mean circulation increases as the duration of the excitation is reduced. These plots tend to show a trend of the Δ=0-18 and 0-60 degree cases having the largest increase in mean circulation, while the Δ= 0-180 degree forcing shows much less.

Comparing the forcing durations of 0-180 and 0-60 degrees helps to show the attenuation effect of applying the excitation throughout the entire intake stroke. In Figure 36, a comparison of Δ=0-180 and 0-60 degrees duration at 1.00 mm, show that these two durations have similar effects through CA=120-130 degrees, then from CA=140-180 degrees, the difference between the two grows with the Δ=0-60 duration increasing at a faster rate in circulation and kinetic energy. Hence, the amount of amplification for Δ=0-60 compared to Δ=0-180 grows as the crank angle increases beyond 140 degrees.

When compared to the natural case, all of the durations examined had an amplification effect from 90 to 110 degrees, which is probably due to the increased inclination angle of the annular intake jet causing less energy lost from impinging on the cylinder wall, and the increased inclination angle relocating the center of the main vortex lower in the cylinder where data was acquired (compare Figures 17 and 23 at CA = 100 degrees).

When comparing the unperturbed case to the forced cases at the end of the intake stoke, the largest amplification came from the forced cases which were excited for a short in the beginning of the stroke (Δ=0-18). As observed in the flow visualization, the excitation early in the intake stroke have long term effects on the large scale motions, and excitation early in the stroke does not just dissipate.

A summary of the percent change in the mean values of the calculated quantities at CA = 180 degrees are listed in Table 4 (Figures listed with an A or B refer to Appendix A or B).

Table 4: Percent Change* in Mean Circulation, Mean Tumble Ratio, Mean Kinetic Energy, and Minimum Vorticity from No Excitation at 180 Degrees Crank Angle

Freq. f (Hz)	Amp. A (mm)	Duration Δ (deg)	Mean Circulation	Mean Tumble Ratio	Mean Kinetic Energy	Peak Vorticity (minimum)	Figure Number(s)
20	1.00	0-180	3.1	2.02	5.64	5.1	A2, B2
30	1.00	0-180	-1.1	-26.8	-5.29	13.3	A3, B3
40	1.00	0-180	25.3	-17.1	8.3	44.0	A4, B4, 19
60	1.00	0-180	-17.7	-44.0	-33.5	-11.2	A5, B5, 20
40	0.35	0-180	8.0	9.01	-3.67	0.7	A6, B6, 18
60	0.35	0-180	11.1	-23.2	2.23	1.0	A7, B7
40	0.35	0-18	43.2	33.9	37.6	29.5	A8, B8, 21
60	0.35	0-18	31.0	-16.4	36.4	27.5	A9, B9, 22
90	0.35	0-18	24.3	17.6	36.0	33.9	A10, B10
40	1.00	0-18	37.5	3.6	19.3	20.5	A11, B11
60	1.00	0-18	30.9	4.75	29.7	20.6	A12, B12
40	0.35	0-60	28.4	1.73	27.8	20.5	A13, B13
60	0.35	0-60	32.2	5.82	26.5	29.8	A14, B14, 23
90	0.35	0-60	36.9	12.9	23.8	31.0	A15, B15
40	1.00	0-60	28.0	-1.73	21.0	35.2	A16, B16
60	1.00	0-60	25.9	-6.87	8.31	31.4	A17, B17

* % Change = 100 x (Parameter$_{(Excited)}$ - Parameter$_{(No\ Excitation)}$)/Parameter$_{(No\ Excitation)}$

3.3 Other Parameters that could be Examined and Applications

A study of the details near the flow as it enters the cylinder would be useful in trying to understand the causes for the changes observed in the flow structures when it is excited. Various pertubation strategies could also be used to further examine the effects of A, f, and Δ. For example, the forcing frequency could be sinusoidal; starting at TDC at 0Hz

progressing to a maximum frequency at mid-stoke, and then decreasing back to 0 at BDC to maintain a constant St_D based on the mean flow entering through the intake valve (see §3.1.2). Another pertubation strategy could have the amplitude gradually decrease throughout the intake stroke to reduce the counteracting circulation patters generated by the motion of the valve. A further examination of smaller amplitudes and other excitation durations, not done in this study, could also give more insight into the effects of the excitation. The interactions between two excited intake annular jets from a four valve configuration would be another complex aspect that could be studied.

It is also important to note that this study focused on one engine speed, so that is an additional parameter which would change all of the preferred excitation parameters. Therefore, the application of this technique to an operating engine would require a calibration to map the optimum forcing parameters versus speed and load for the engine. In applying an excitation in an operational engine, the method of using the valve to excite the flow may not be practical. It would require a complicated redesign of the valve train (cams, rocker arms, etc...) to implement, which could have wear problems, and a host of other issues. However, the implementation of the excitation could be introduced in a number of different ways, such as acoustically in the intake manifold runners. As a result, these issues are not seen as unfeasible. Steady state fuel consumption and power output under firing conditions could then be used to directly compare between the natural and perturbed engine configurations, leading directly to the applicability of excited flows to internal combustion engines.

Chapter 4

CONCLUSIONS

1. The objective of this study was to examine the effects of introducing disturbances in to the flow of a piston-cylinder arrangement with the emphasis on flow features that might enhance combustion in an internal combustion engine. It was determined that the introduction of small disturbances increase the peak vorticity levels, circulation, and tumble ratio, with the overall best case increasing the mean circulation 43% at CA=180 degrees.

2. The earlier the applied disturbance is terminated, then generally the greater the amplification of the peak vorticity levels, circulation, and tumble ratio through the end of the stroke. Specifically looking at amplification of the mean circulation at 180 degrees, applying the disturbance during the first 18 degrees of the stroke provides up to a 43% increase, a disturbance over the first 60 degrees provides up to a 32% increase, and applying disturbances during the first 180 degrees provides up to a 25% increase in circulation.

3. The smaller the peak to peak amplitude, then generally the larger the amplification of the peak vorticity levels, circulation, and tumble ratio through. For the amplitude of 0.35 mm, was found to increase the mean circulation up to 43% while the amplitude of 1.00 mm increased it up to 28% for the best cases seen.

4. The amount of amplification of the measured parameters as a function of frequency generally showed the preferred frequency was 40 Hz or a Strouhal Number of 1.19 based upon the maximum velocity of the flow entering through the valve inlet.

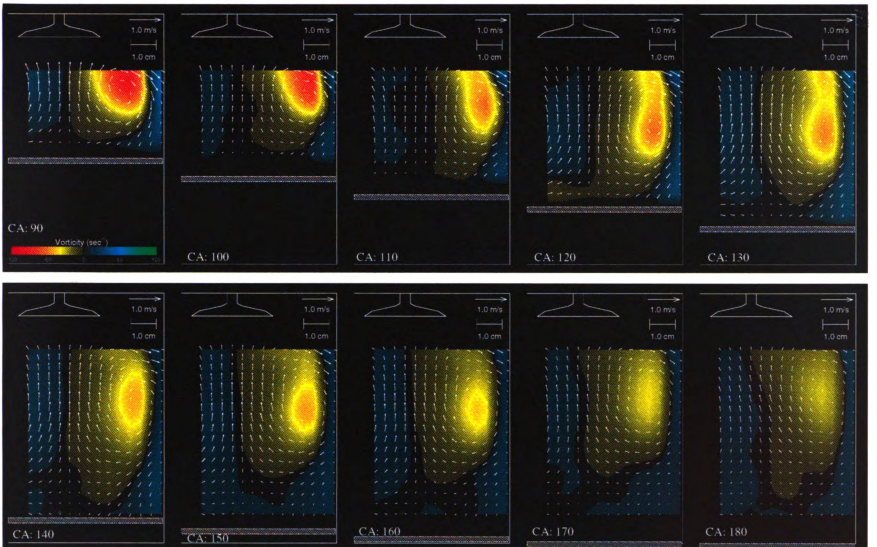

Figure 17. Cycle Averaged Velocity and Vorticity Fields with No Excitation

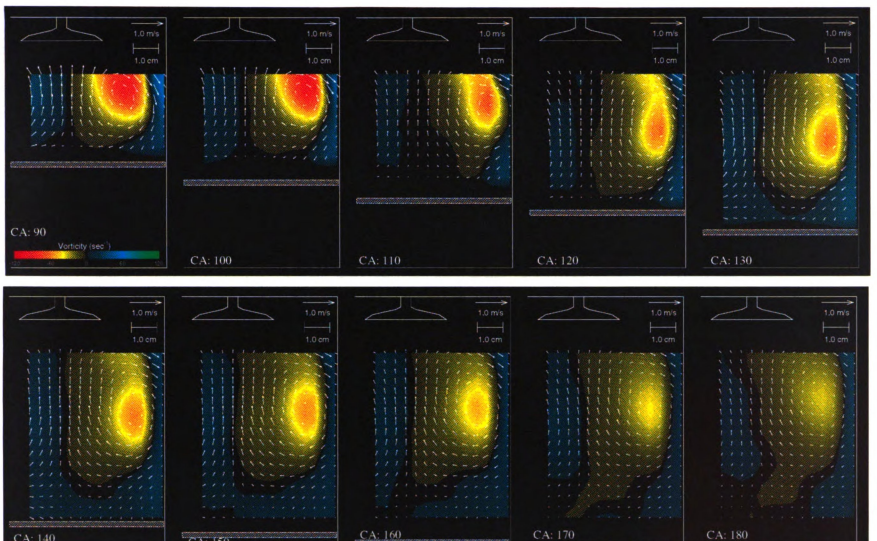

Figure 18. Cycle Averaged Velocity and Vorticity Fields with Excitation Conditions:
f: 40 Hz A: 0.35 mm Δ: 0-180 degrees

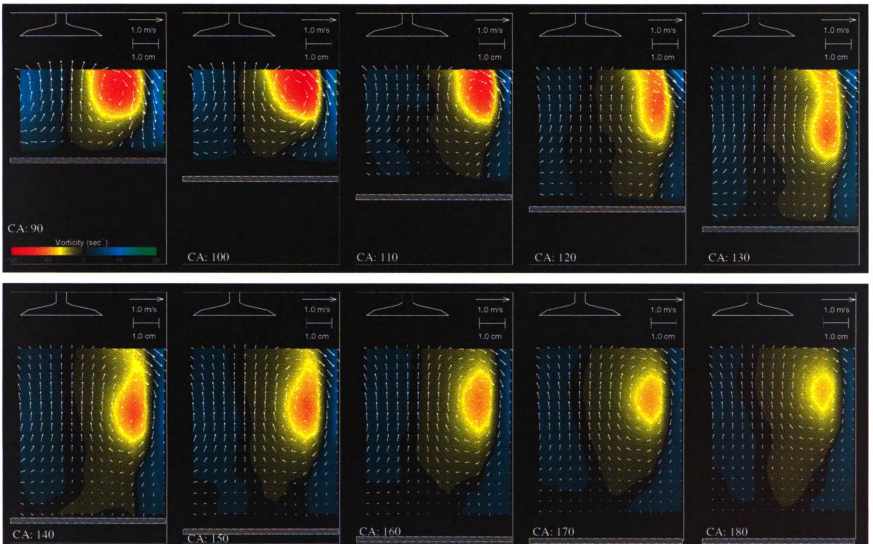

Figure 19. Cycle Averaged Velocity and Vorticity Fields with Excitation Conditions:
f: 40 Hz A: 1.00 mm Δ: 0-180 degrees

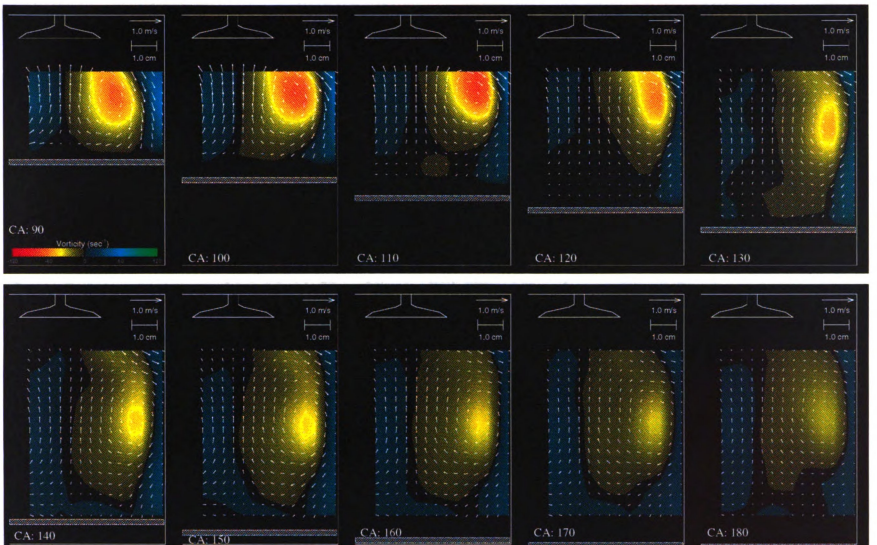

Figure 20. Cycle Averaged Velocity and Vorticity Fields with Excitation Conditions:
f: 60 Hz *A*: 1.00 mm Δ: 0-180 degrees

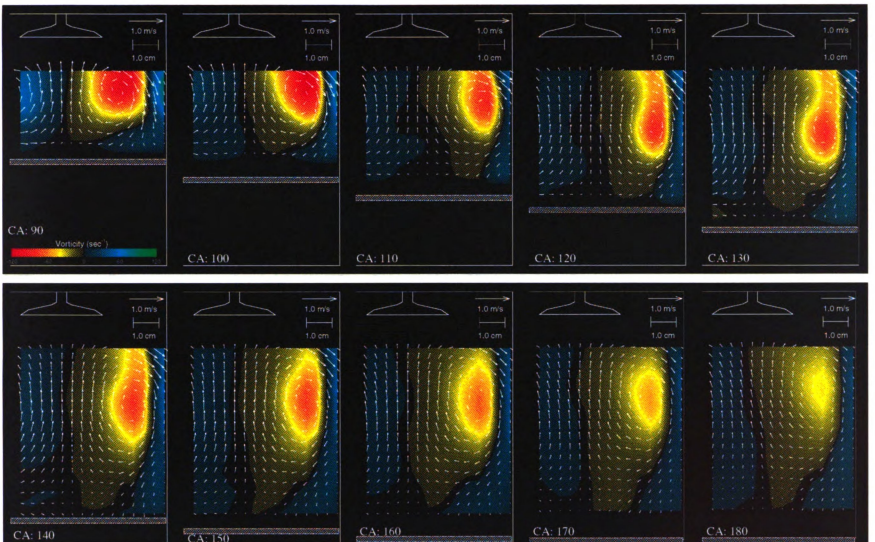

Figure 21. Cycle Averaged Velocity and Vorticity Fields with Excitation Conditions:
f: 40 Hz A: 0.35 mm Δ: 0-18 degrees

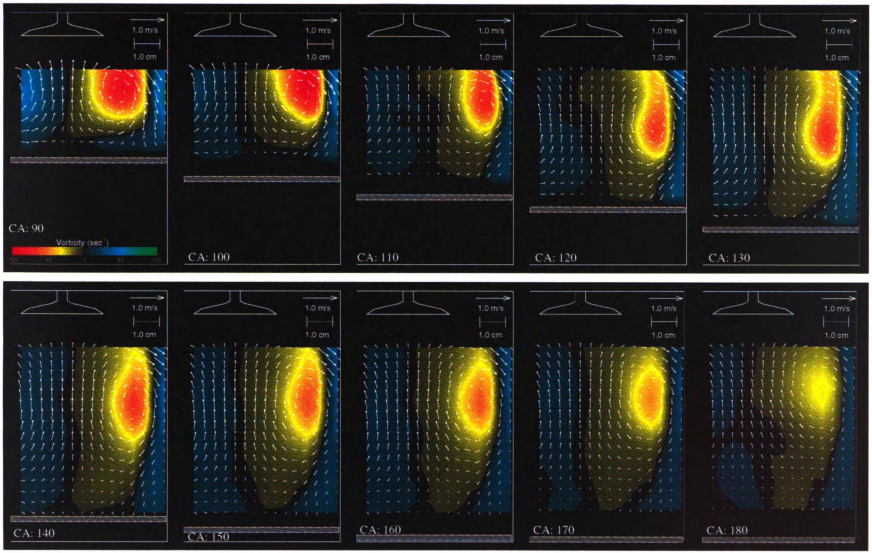

Figure 22. Cycle Averaged Velocity and Vorticity Fields with Excitation Conditions:
f: 60 Hz A: 0.35 mm Δ: 0-18 degrees

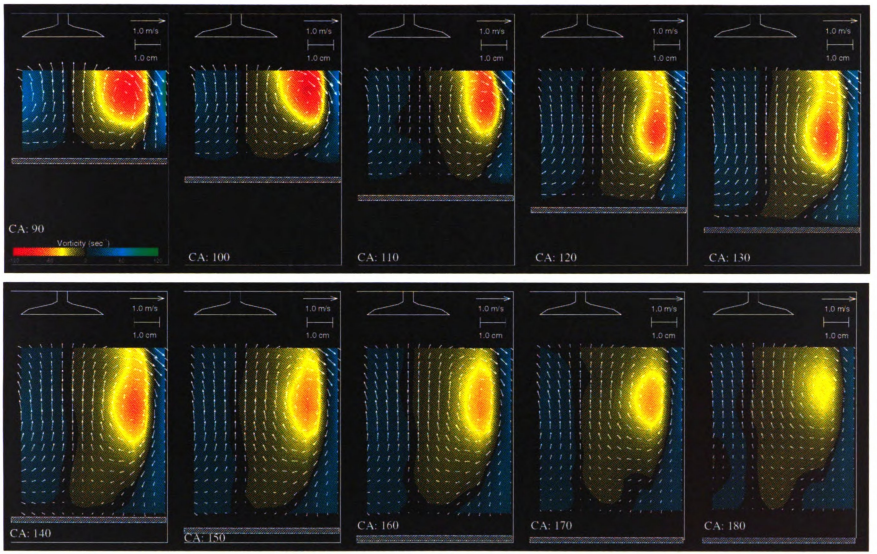

Figure 23. Cycle Averaged Velocity and Vorticity Fields with Excitation Conditions:
f: 60 Hz A: 0.35 mm Δ: 0-60 degrees

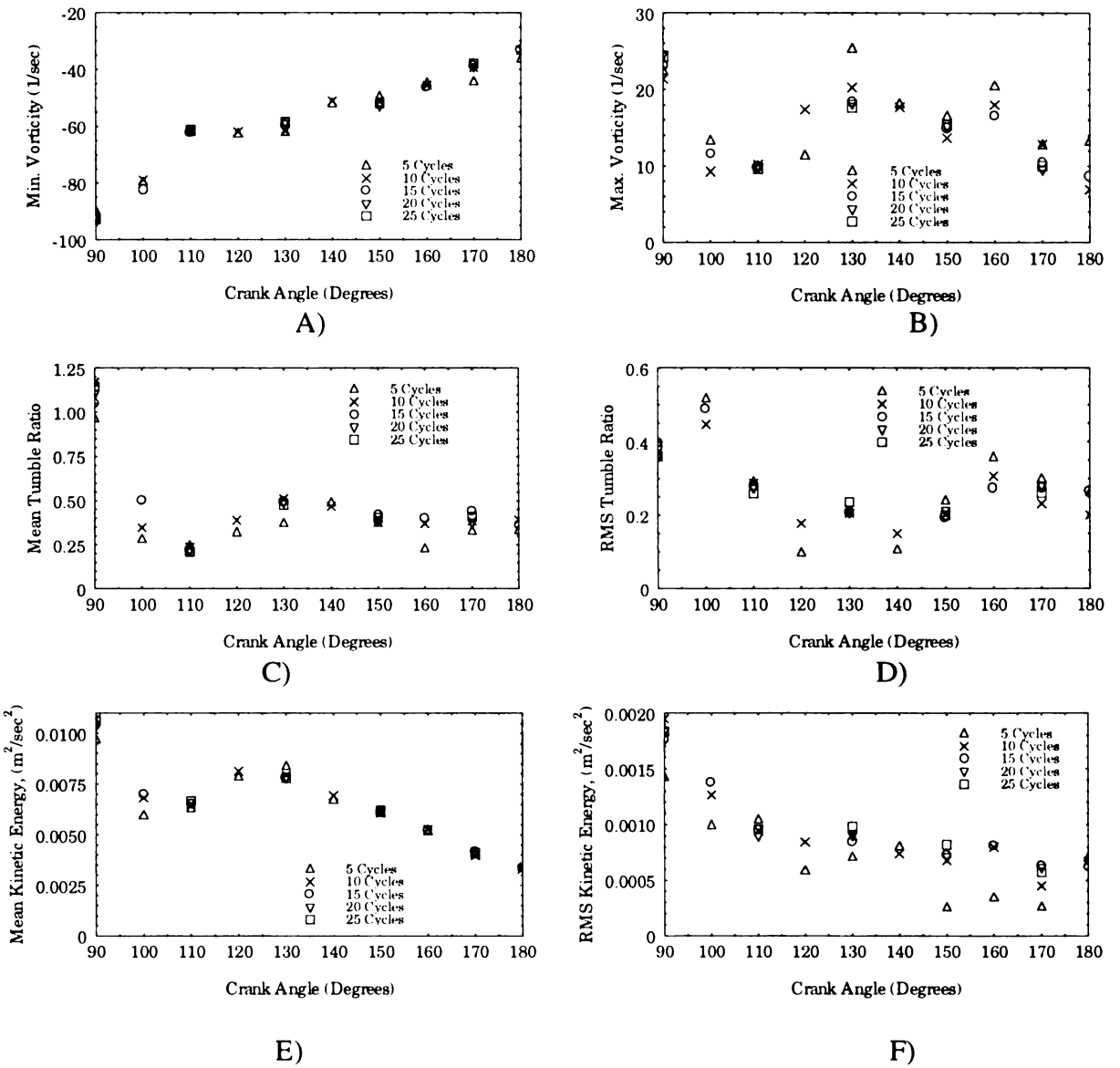

Figure 24. Effects of the Sample Size of Engine Cycle used for Ensemble Averaging of Peak Vorticity, Tumble Ratio, and Kinetic Energy - No Valve Excitation

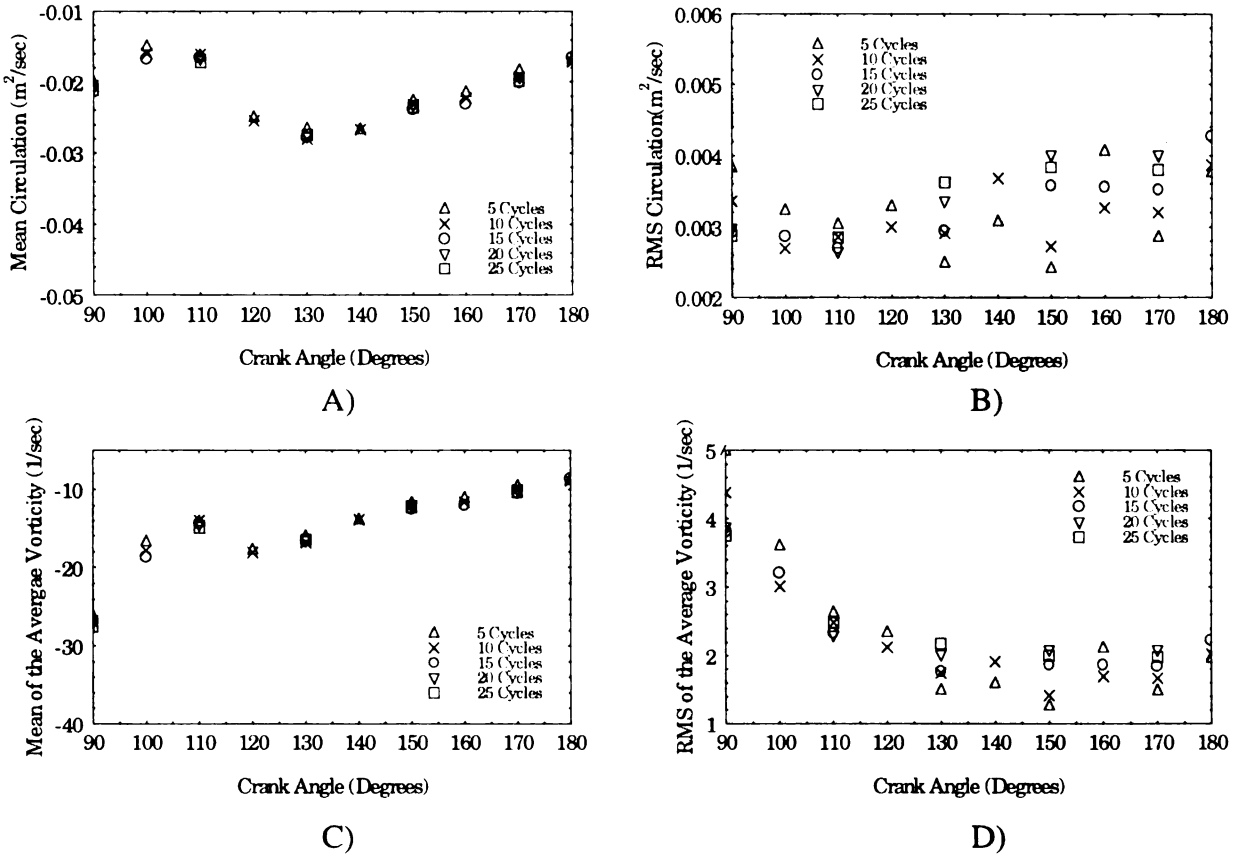

Figure 25. Effects of the Sample Size of Engine Cycle used for Ensemble Averaging of Circulation and Average Vorticity - No Excitation

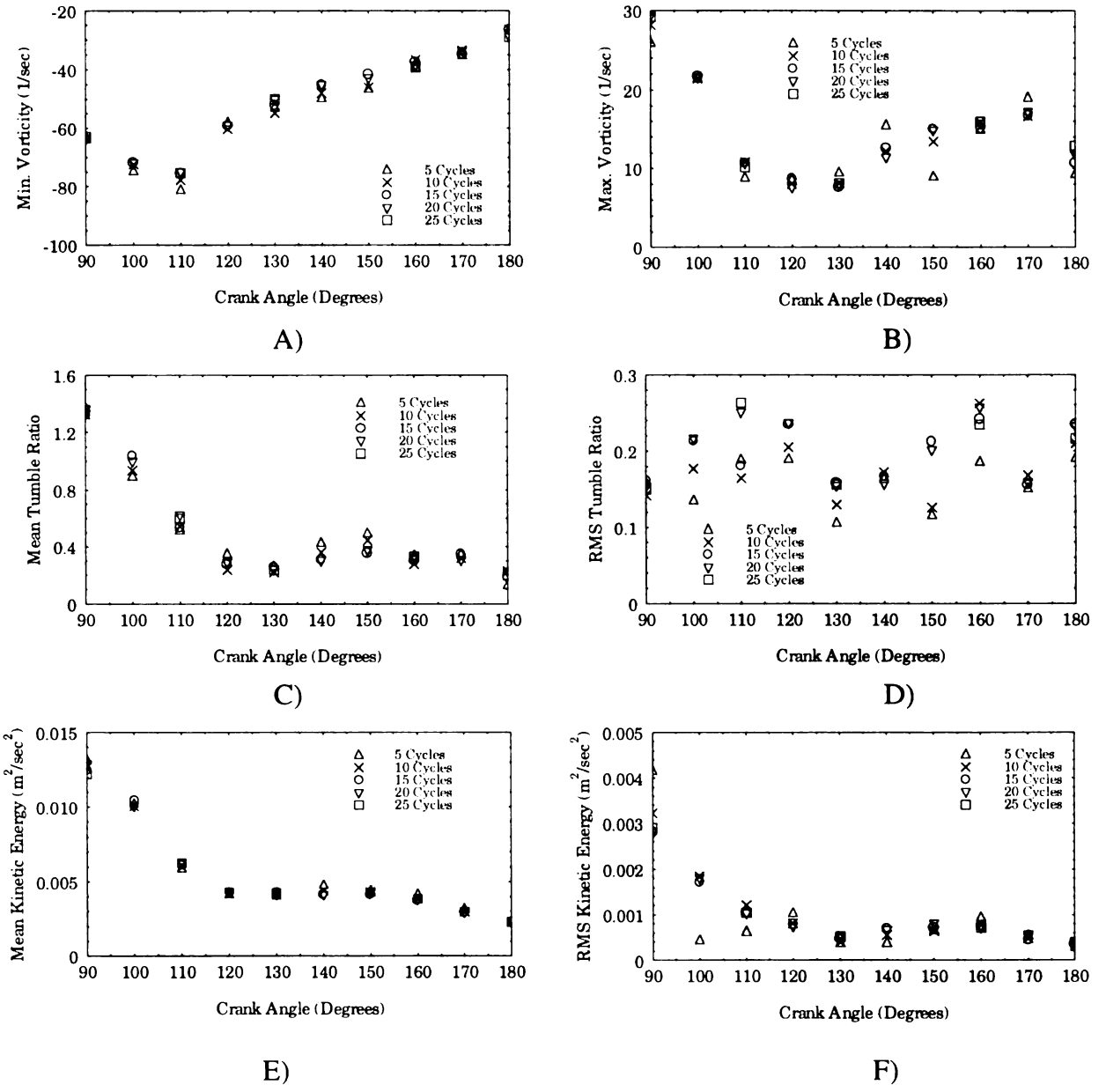

Figure 26. Effects of the Sample Size of Engine Cycle used for Ensemble Averaging of Peak Vorticity, Tumble Ratio, and Kinetic Energy Valve Excitation: f = 60 Hz, A = 1.00mm, Δ = 0-180 degrees

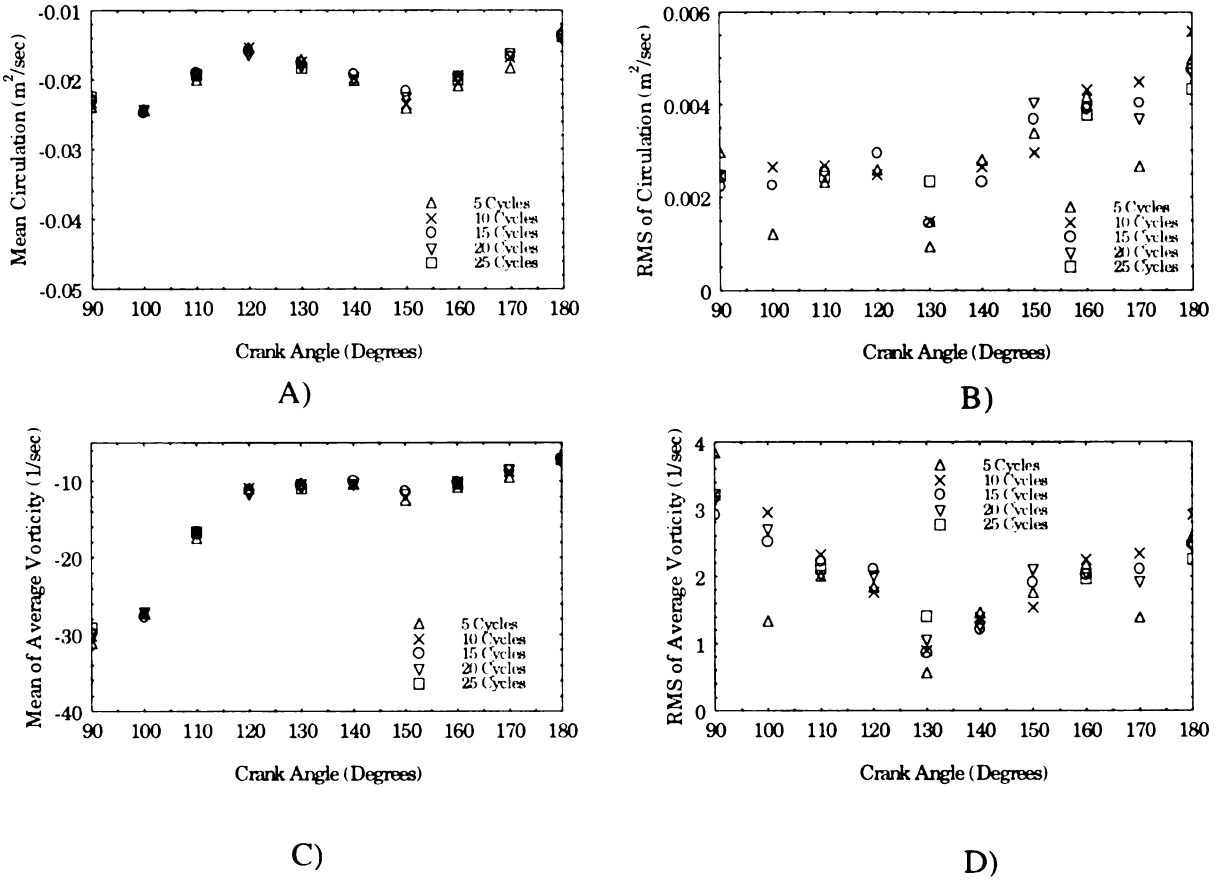

Figure 27. Effects of the Sample Size of Engine Cycle used for Ensemble Averaging of Circulation and Average Vorticity - Valve Excitation: f = 60 Hz, A = 1.00mm, Δ = 0-180 degrees

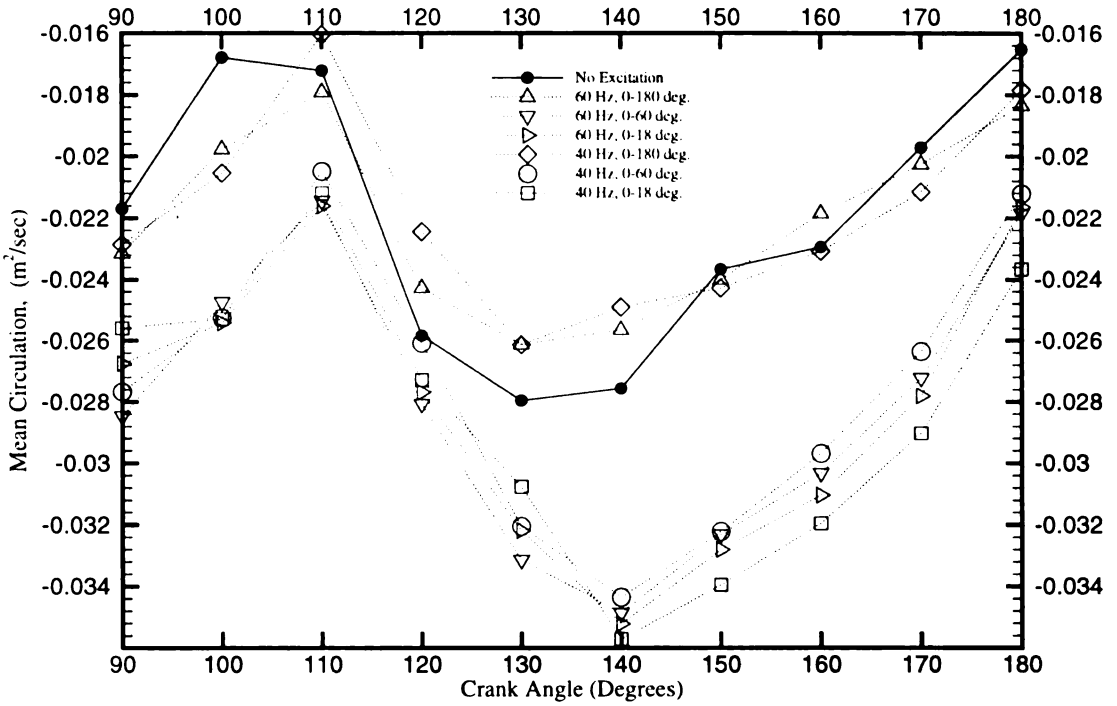

A

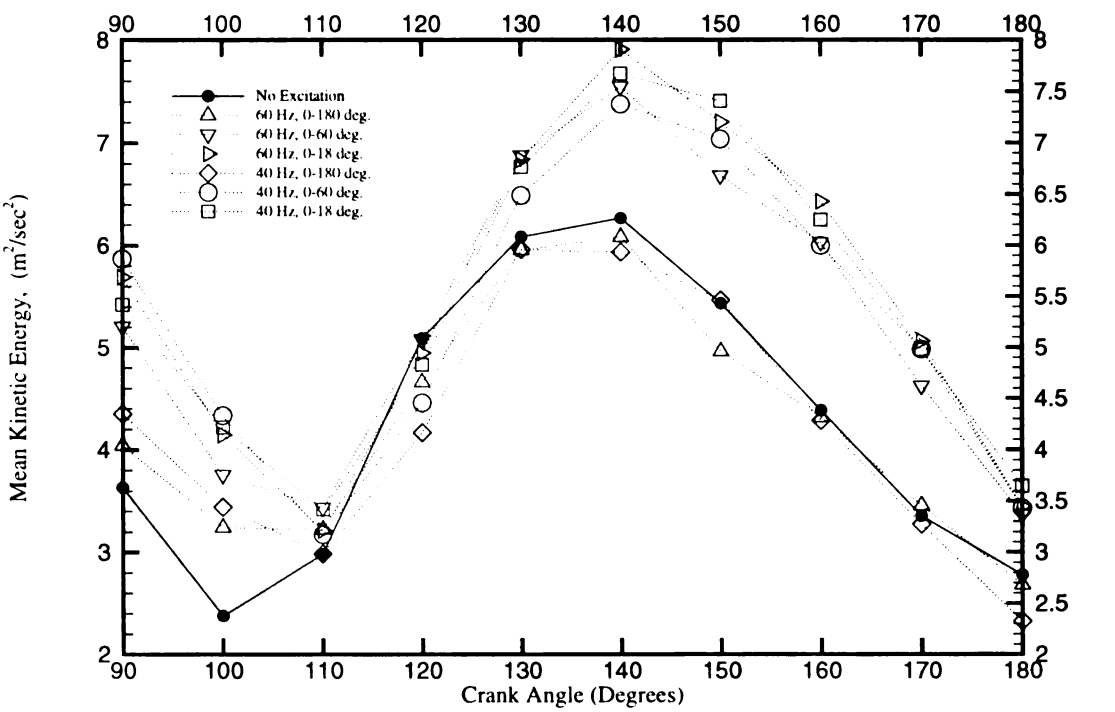

B

Figure 28. Mean Circulation and Mean Kinetic Energy for A=0.35 mm, and All Conditions with f=40 and 60 Hz, Δ = 0-180, 0-60, and 0-18 degrees

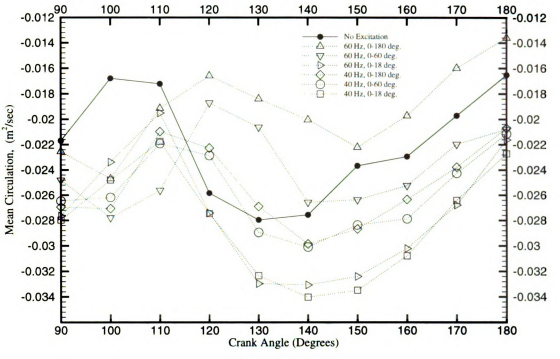

A

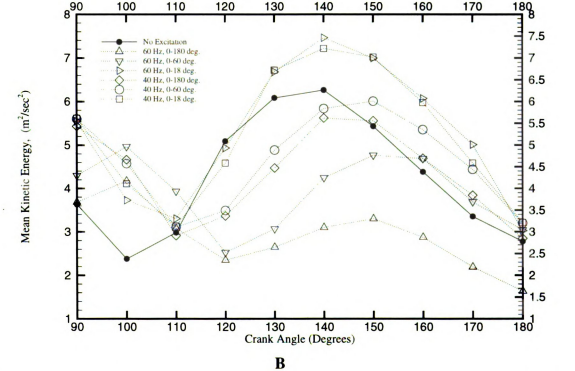

B

Figure 29. Mean Circulation and Mean Kinetic Energy for A=1.00 mm, and All Conditions with f=40 and 60 Hz, Δ = 0-180, 0-60, and 0-18 degrees

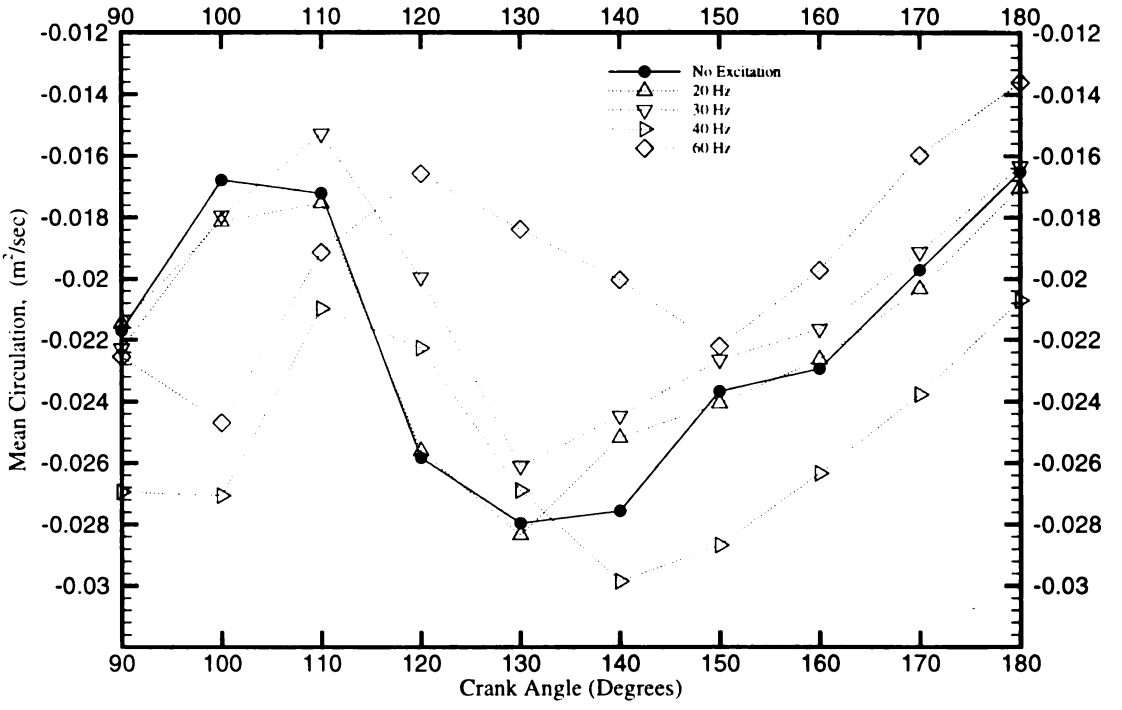

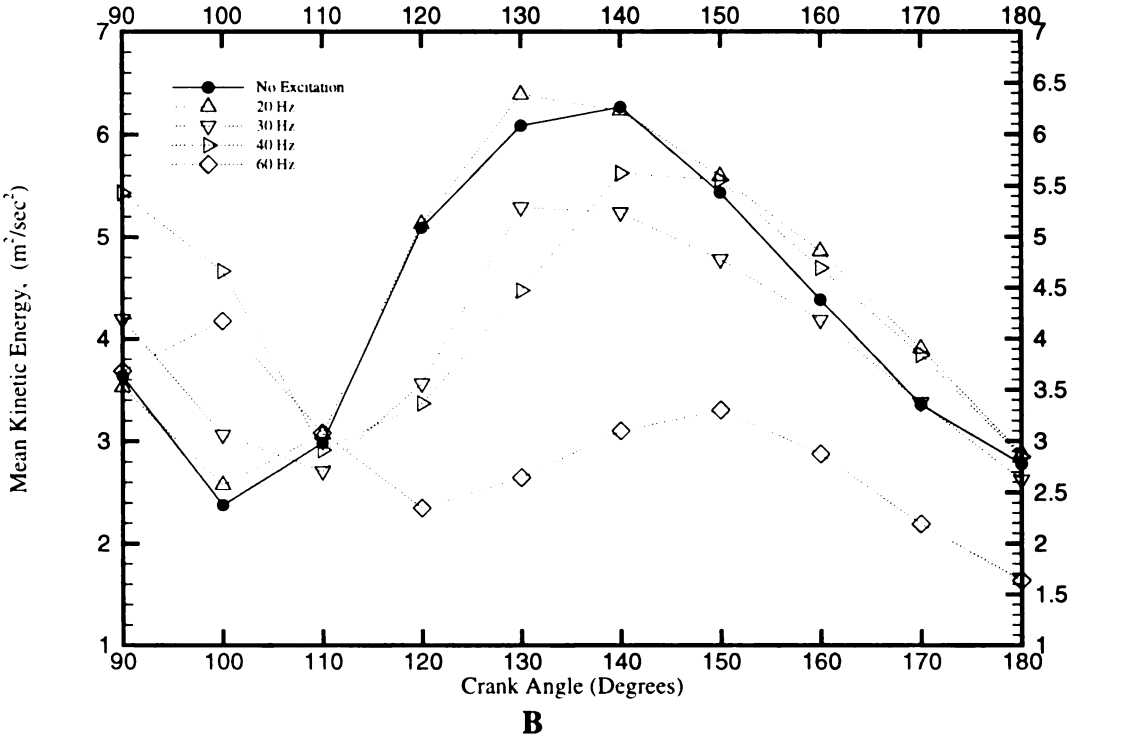

Figure 30. Mean Circulation and Mean Kinetic Energy for f= 20, 30, 40, and 60 Hz, with A=1.00 mm and, Δ = 0-180 degrees

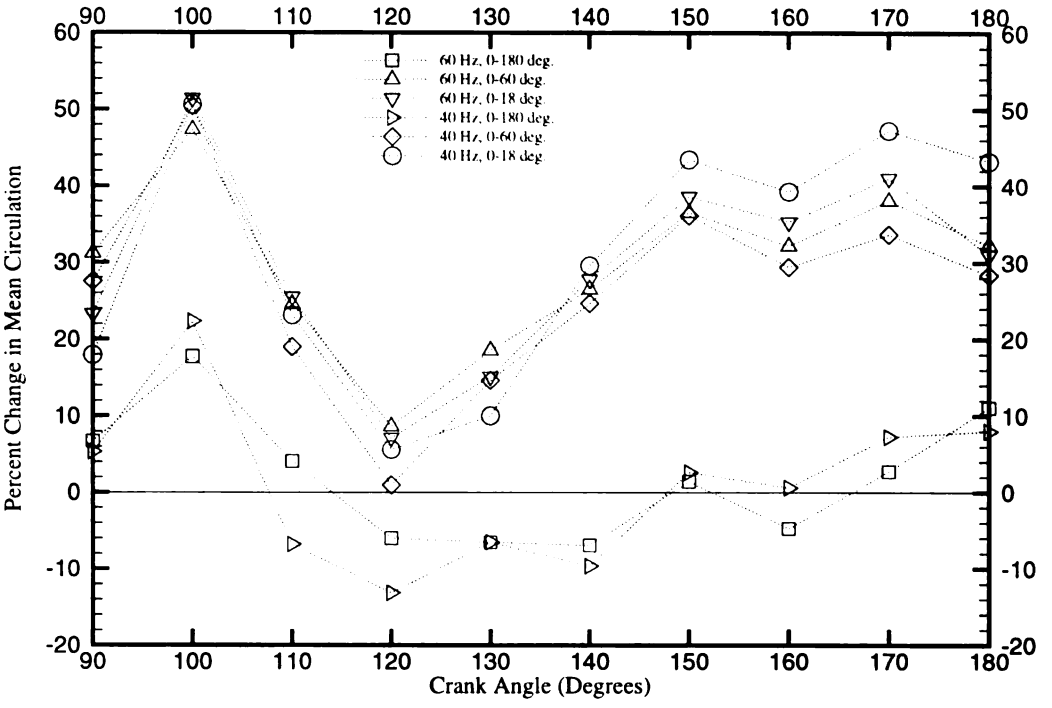

A

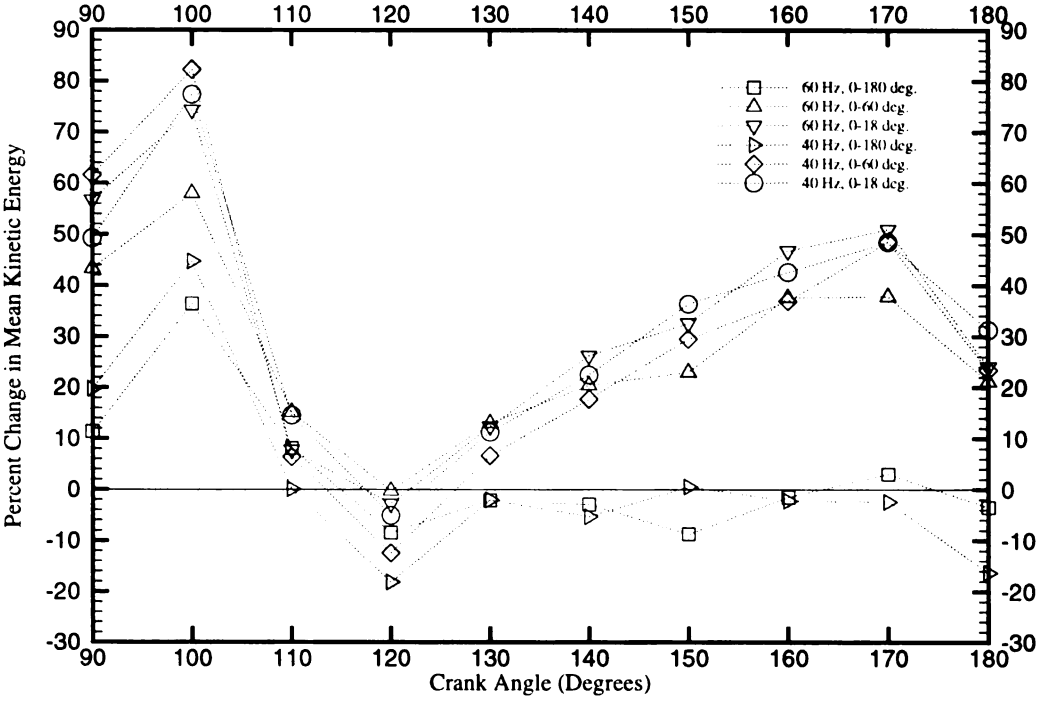

B

Figure 31. Percent Changes* in Mean Circulation and Mean Kinetic Energy between No Excitation to Cases with Forcing Amplitudes of 0.35 mm

* % Change = 100 x (Parameter$_{(0.35\ mm)}$ - Parameter$_{(No\ Excitation)}$)/Parameter$_{(No\ Excitation)}$

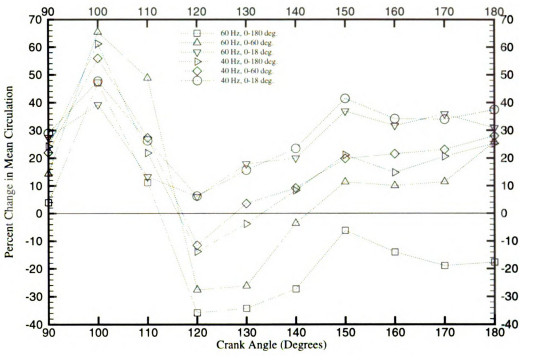

A

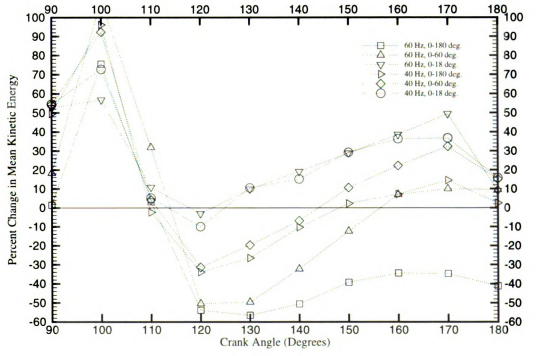

B

Figure 32. Percent Changes* in Mean Circulation and Mean Kinetic Energy between No Excitation to Cases with Forcing Amplitudes of 1.00 mm

* % Change = 100 x (Parameter$_{(1.00\ mm)}$ - Parameter$_{(No\ Excitation)}$)/Parameter$_{(No\ Excitation)}$

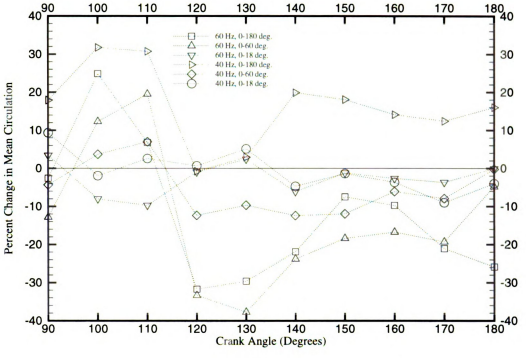

A

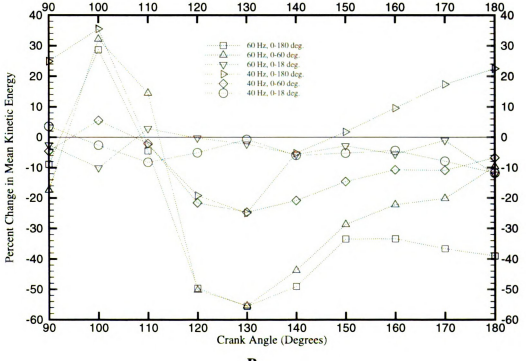

B

Figure 33. Percent Changes* in Mean Circulation and Mean Kinetic Energy from Increasing the Forcing Amplitude from 0.35 mm to 1.00 mm.

* % Change = 100 x (Parameter$_{(1.00\ mm)}$ - Parameter$_{(0.35\ mm)}$)/Parameter$_{(0.35\ mm)}$

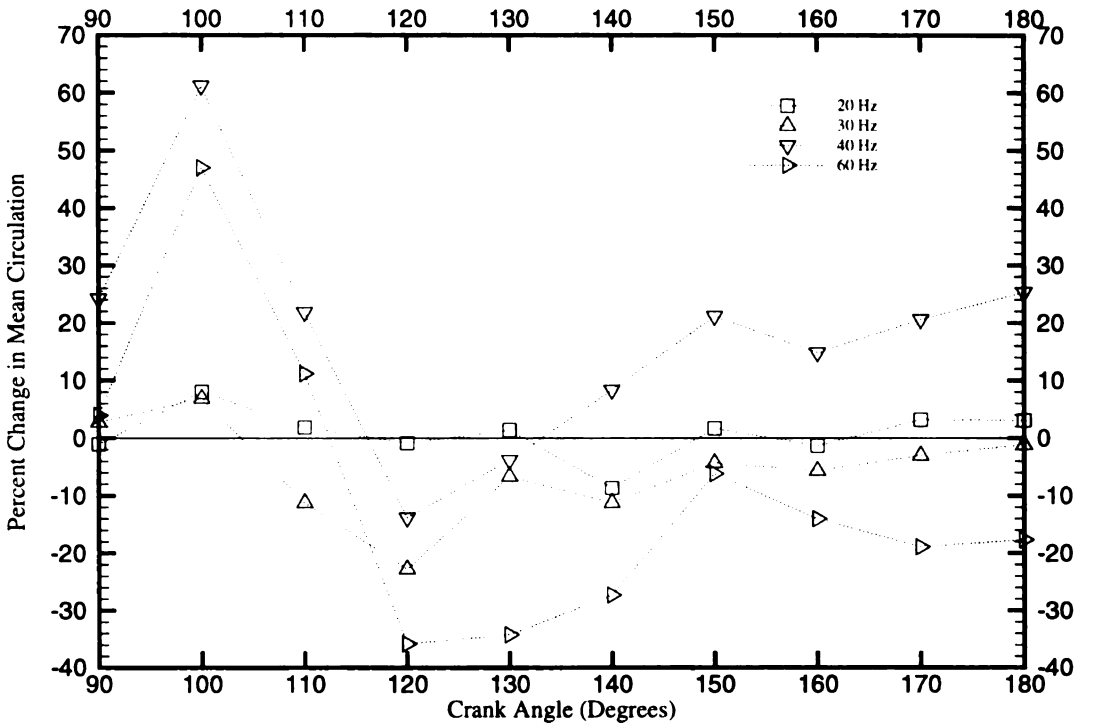

A

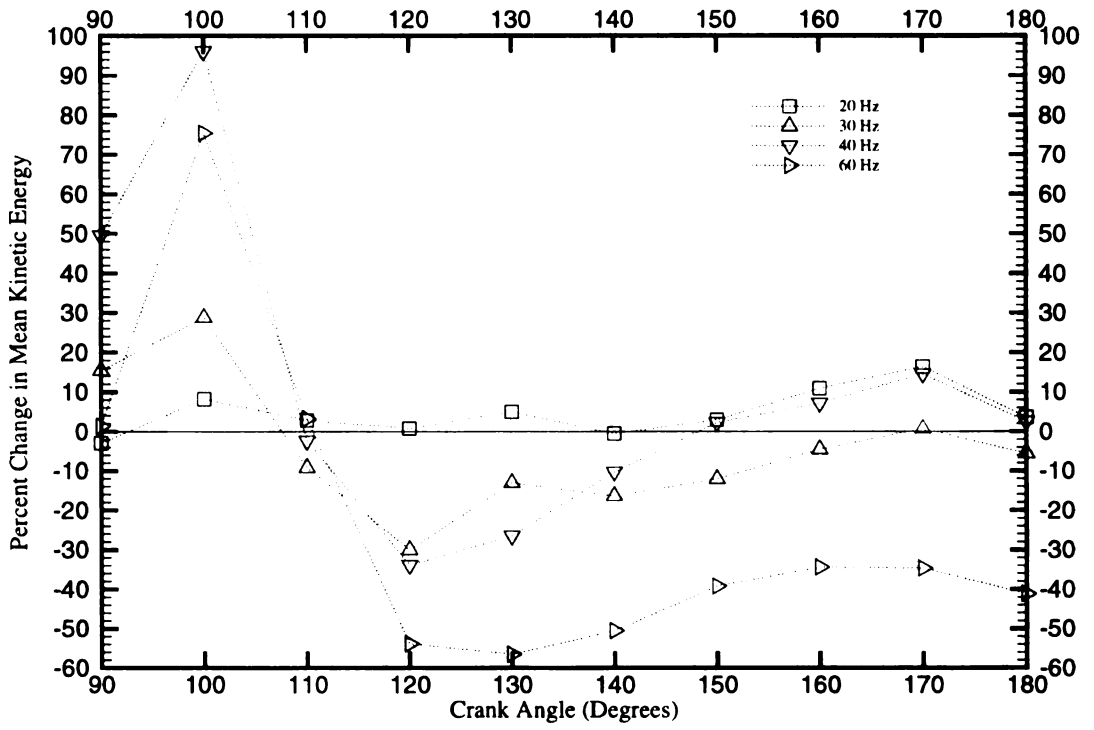

B

Figure 34. Percent Changes* in Mean Circulation and Mean Kinetic Energy between No Excitation and 20, 30, 40, and 60 Hz at A=1.00 mm, Δ=0-180 degrees.

* % Change = 100 x (Parameter$_{\text{(At Given Frequency)}}$ - Parameter$_{\text{(No Excitation)}}$)/Parameter$_{\text{(No Excitation)}}$

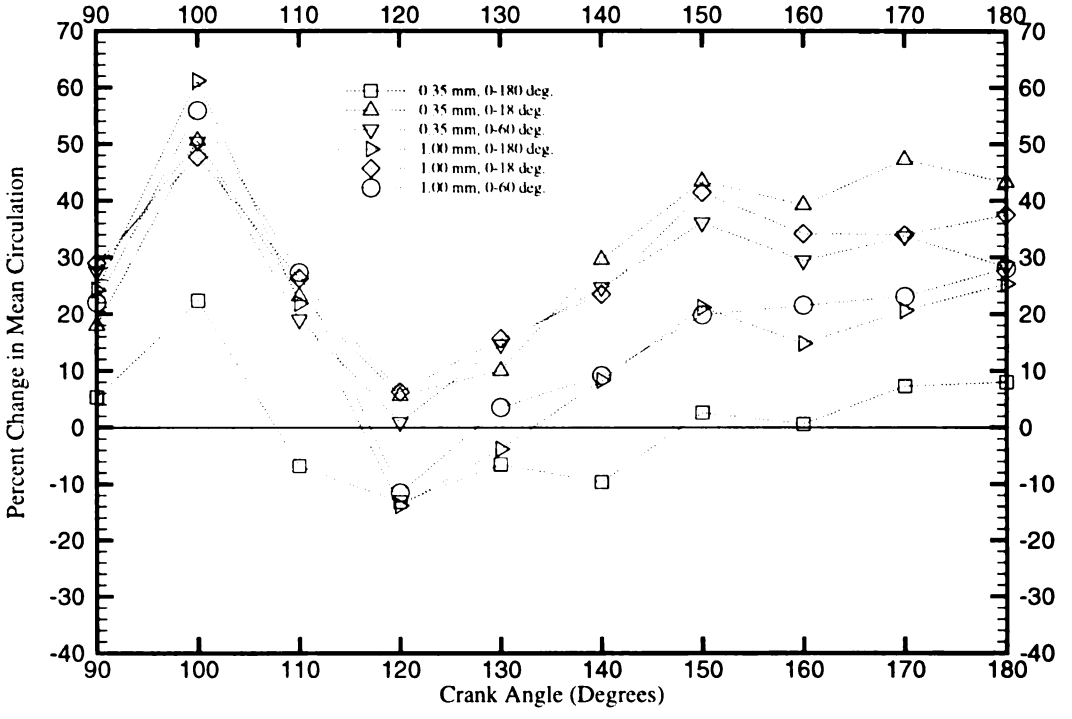

A

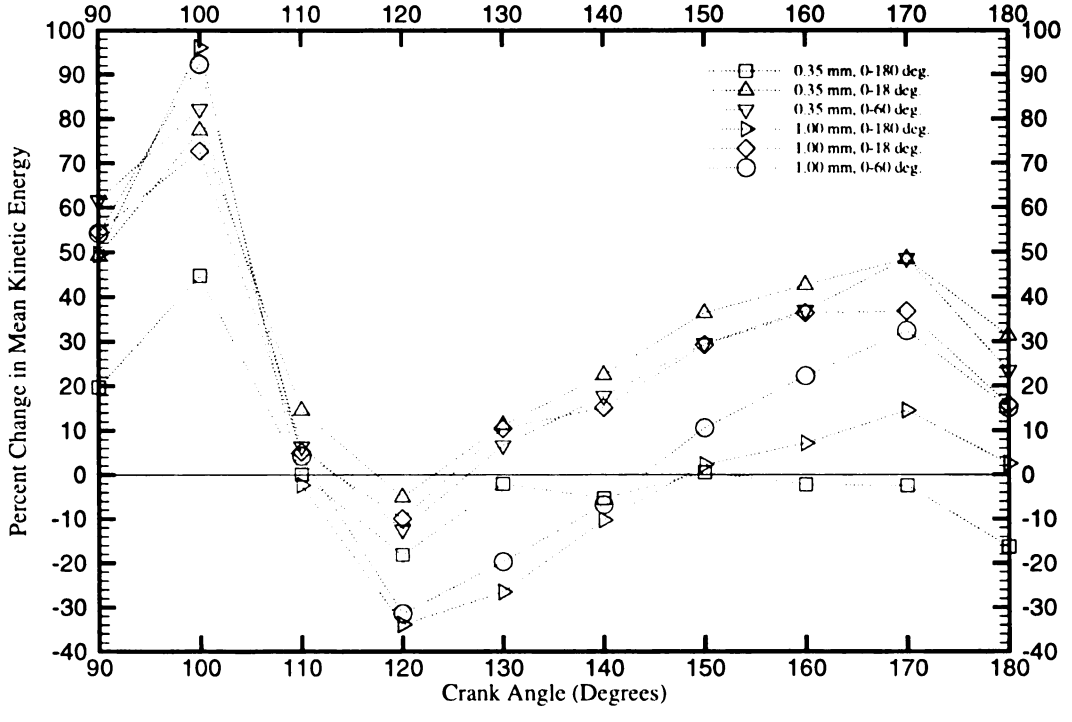

B

Figure 35. Percent Changes* in Mean Circulation and Mean Kinetic Energy between No Excitation and Different Excitation Durations at 40 Hz

* % Change = 100 x (Parameter$_{(40\ Hz)}$ - Parameter$_{(No\ Excitation)}$)/Parameter$_{(No\ Excitation)}$

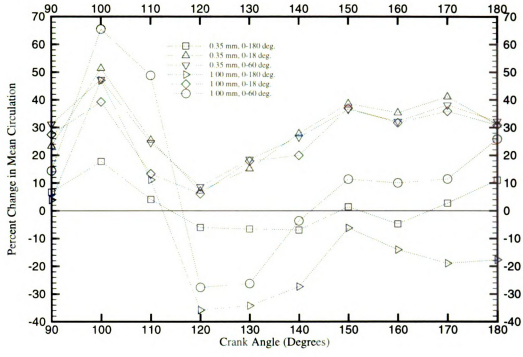

A

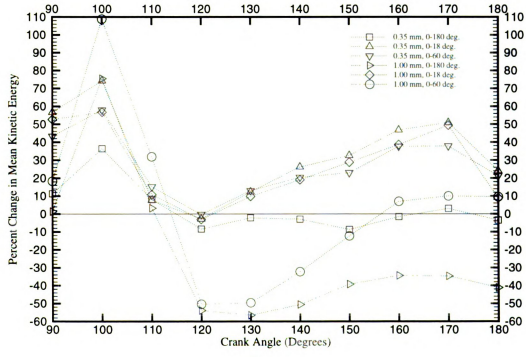

B

Figure 36. Percent Changes* in Mean Circulation and Mean Kinetic Energy between No Excitation and Cases with Forcing Frequencies of 60 Hz

* % Change = 100 x (Parameter$_{(60\ Hz)}$ - Parameter$_{(No\ Excitation)}$)/Parameter$_{(No\ Excitation)}$

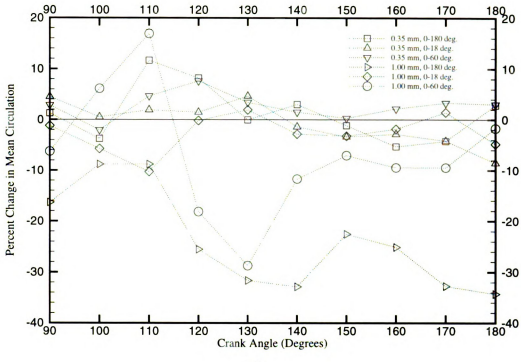

A

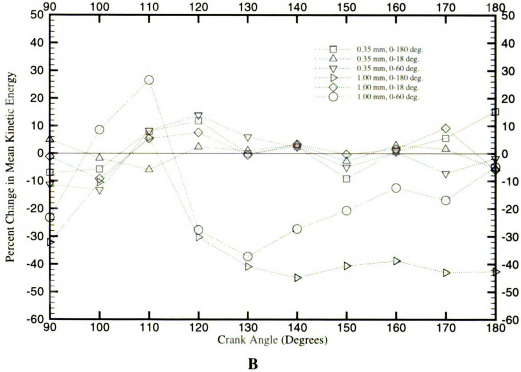

B

Figure 37. Percent Changes* in Mean Circulation and Mean Kinetic Energy when Increasing the Excitation Frequency from 40 Hz to 60 Hz.

* % Change = 100 x (Parameter$_{(60\ Hz)}$ - Parameter$_{(40\ HZ)}$)/Parameter$_{(40\ Hz)}$

APPENDICES

APPENDIX A

Flow Visualization Images at 340 RPM

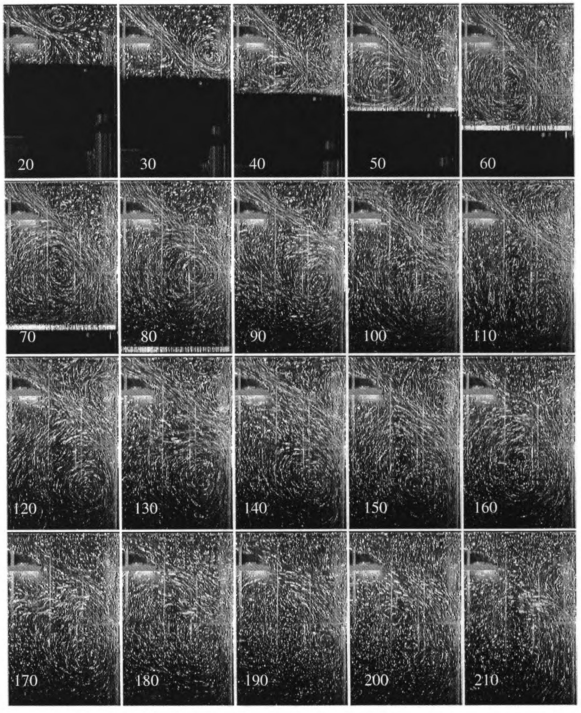

Figure A1. No Valve Excitation

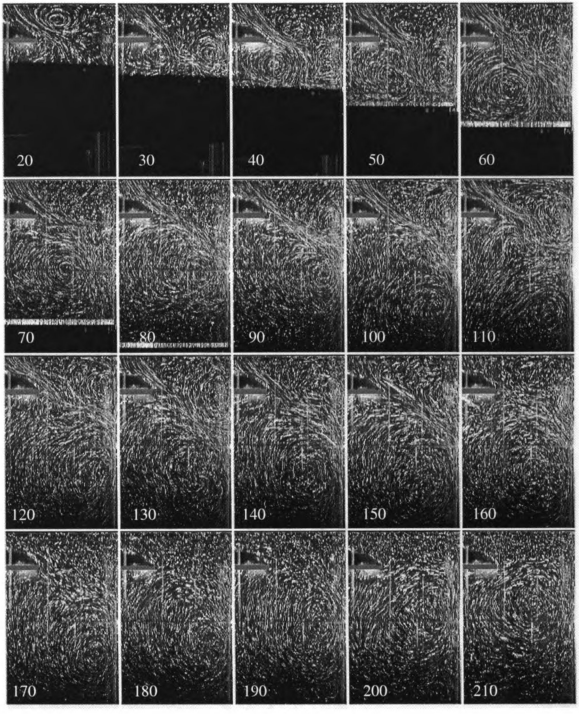

Figure A2. *f*: 20 Hz, *A*: 1.00mm, Δ: 0-180 degrees

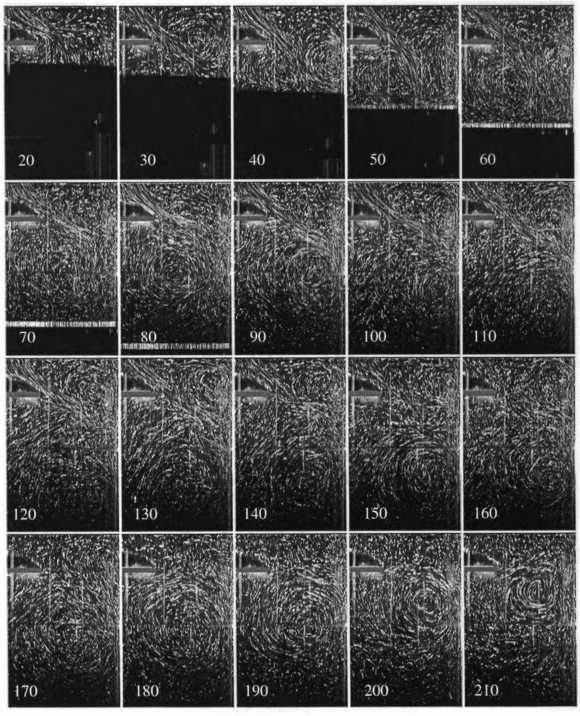

Figure A3. *f*: 30 Hz, *A*: 1.00mm, Δ: 0-180 degrees

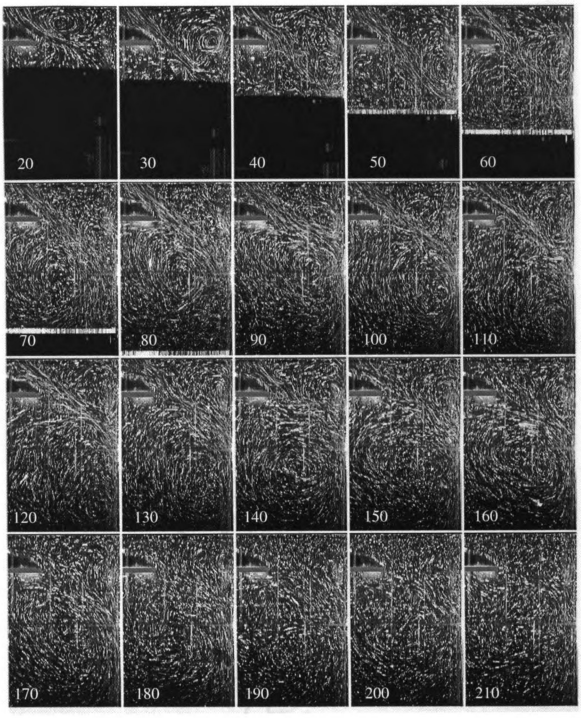

Figure A4. f: 40 Hz, A: 1.00mm, Δ: 0-180 degrees

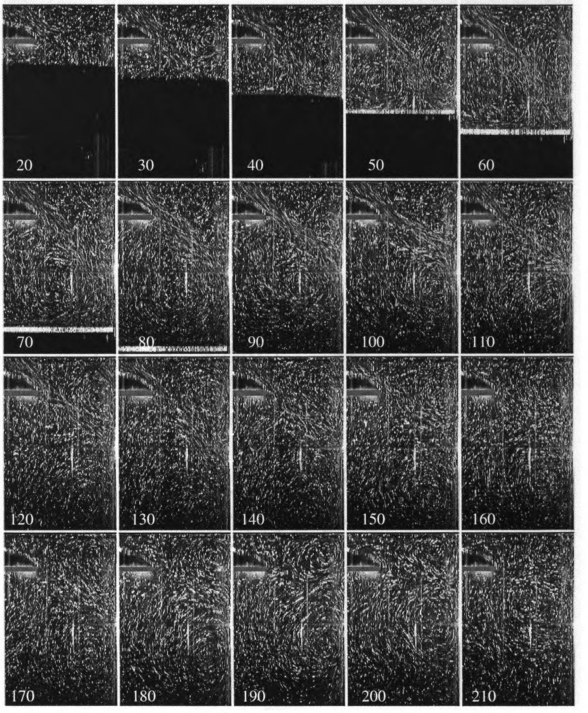

Figure A5. *f*: 60 Hz, *A*: 1.00mm, Δ: 0-180 degrees

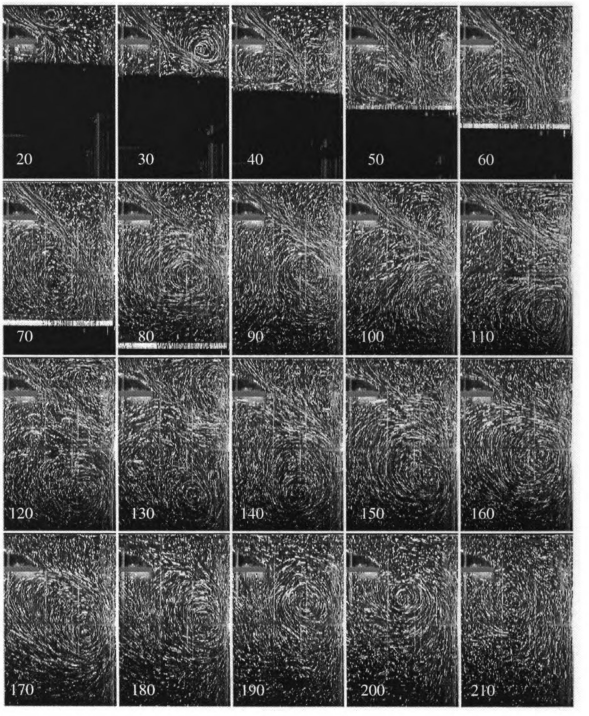

Figure A6. *f*: 40 Hz, *A*: 0.35mm, Δ: 0-180 degrees

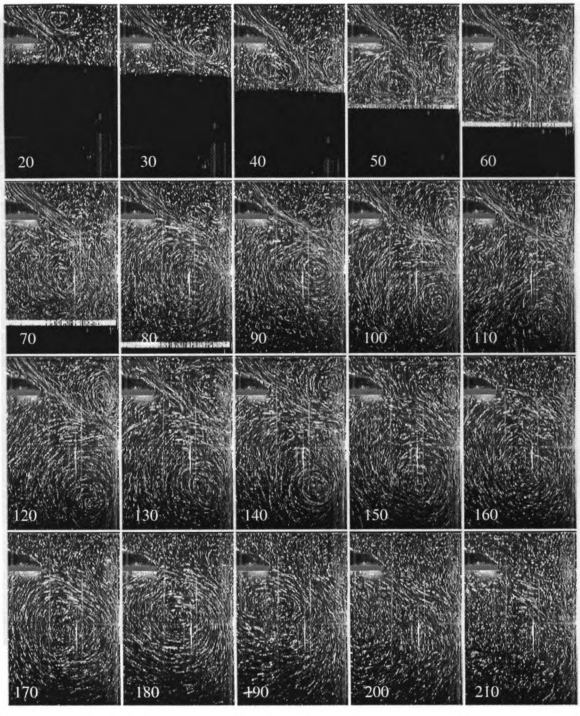

Figure A7. *f*: 60 Hz, *A*: 0.35mm, Δ: 0-180 degrees

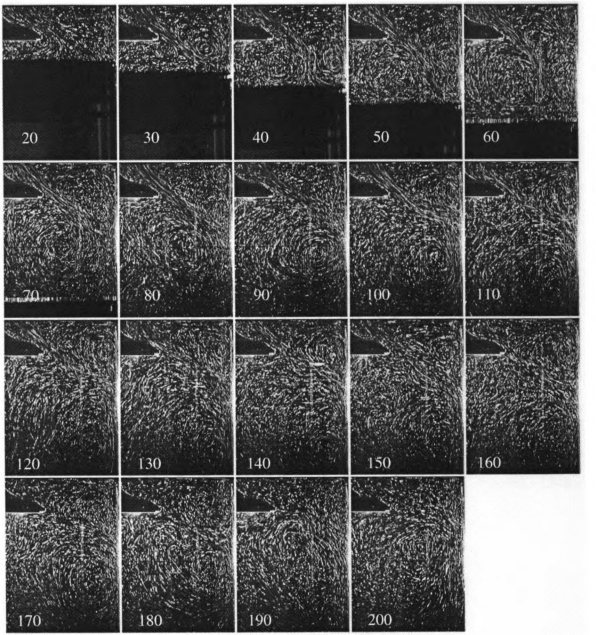

Figure A8. *f*: 40 Hz, *A*: 0.35mm, Δ: 0-18 degrees

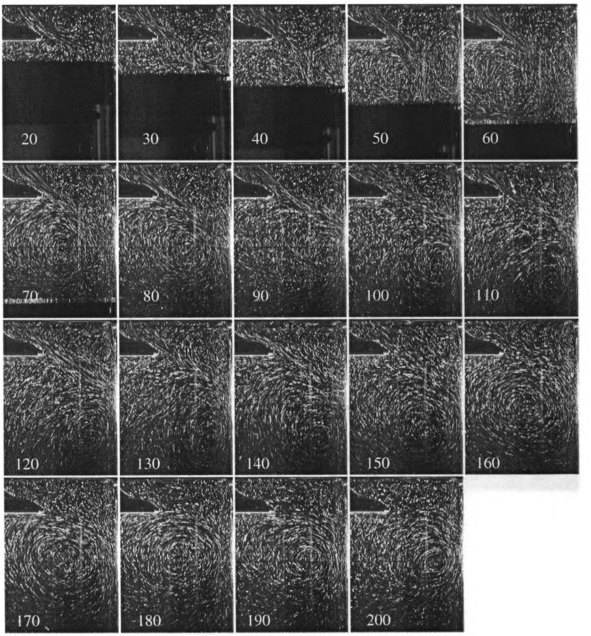

Figure A9. f: 60 Hz, A: 0.35mm, Δ: 0-18 degrees

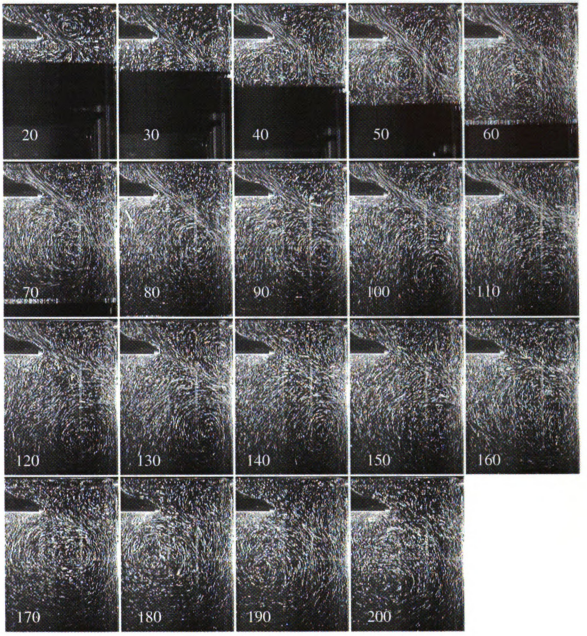

Figure A10. *f*: 90 Hz, *A*: 0.35mm, Δ: 0-18 degrees

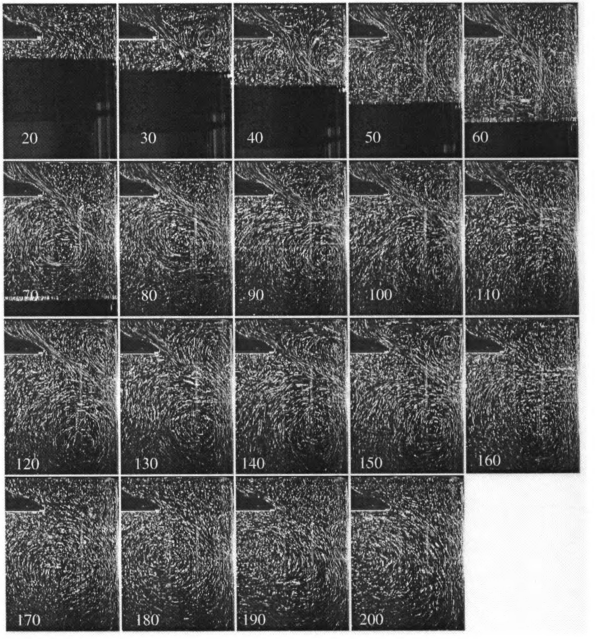

Figure A11. *f*: 40 Hz, *A*: 1.00mm, Δ: 0-18 degrees

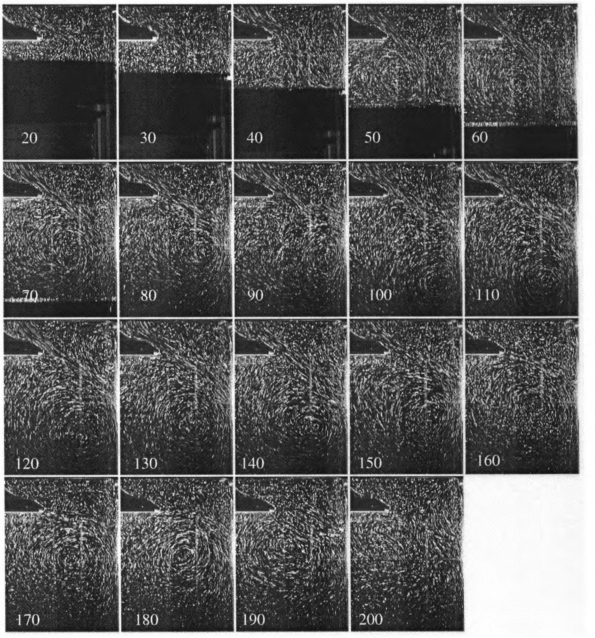

Figure A12. *f*: 60 Hz, *A*: 1.00mm, Δ: 0-18 degrees

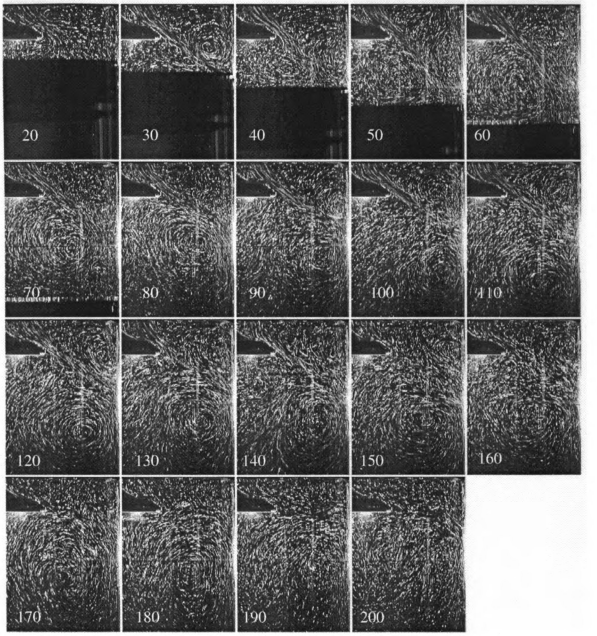

Figure A13. f: 40 Hz, A: 0.35mm, Δ: 0-60 degrees

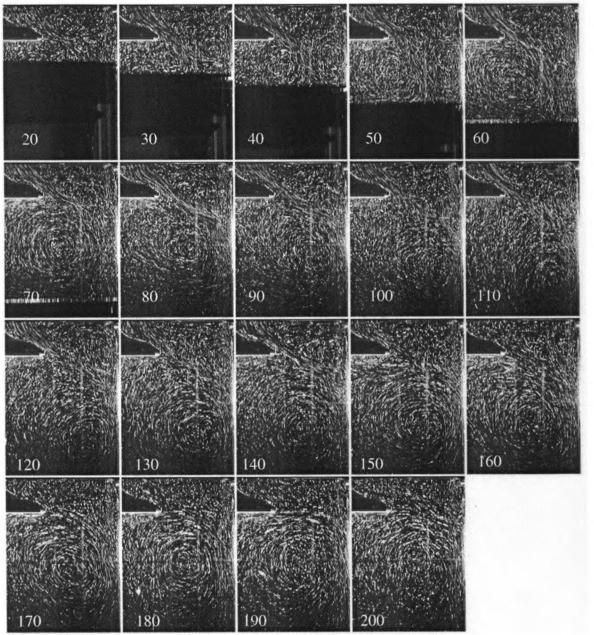

Figure A14. *f*: 60 Hz, *A*: 0.35mm, Δ: 0-60 degrees

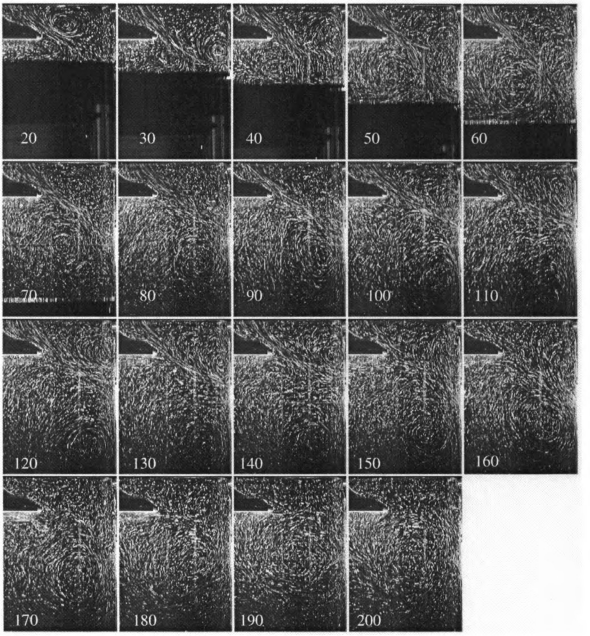

Figure A15. *f*: 90 Hz, *A*: 0.35mm, Δ: 0-60 degrees

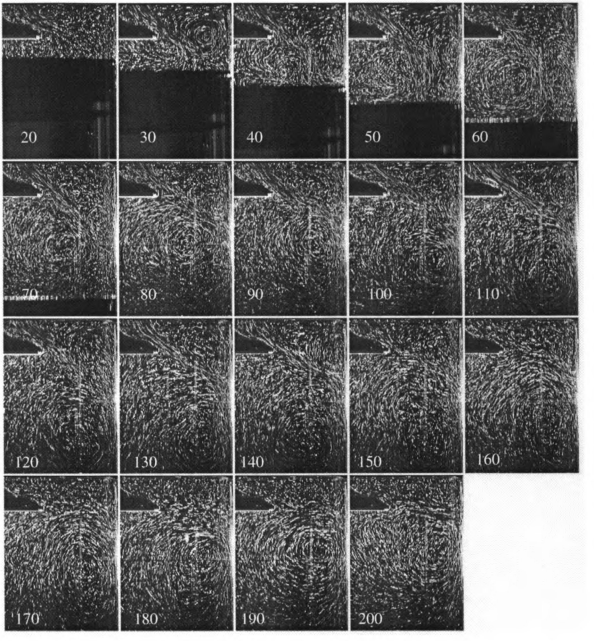

Figure A16. *f*: 40 Hz, *A*: 1.00mm, Δ: 0-60 degrees

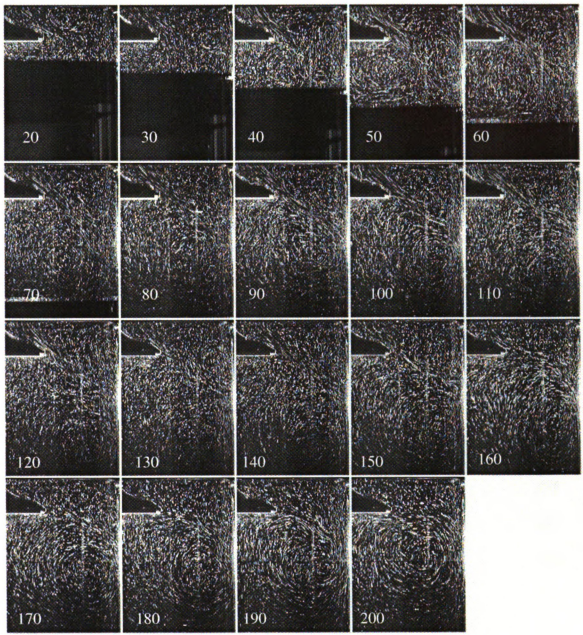

Figure A17. *f*: 40 Hz, *A*: 1.00mm, Δ: 0-60 degrees

APPENDIX B

MTV Ensemble Averaged Velocity Fields at 340 RPM

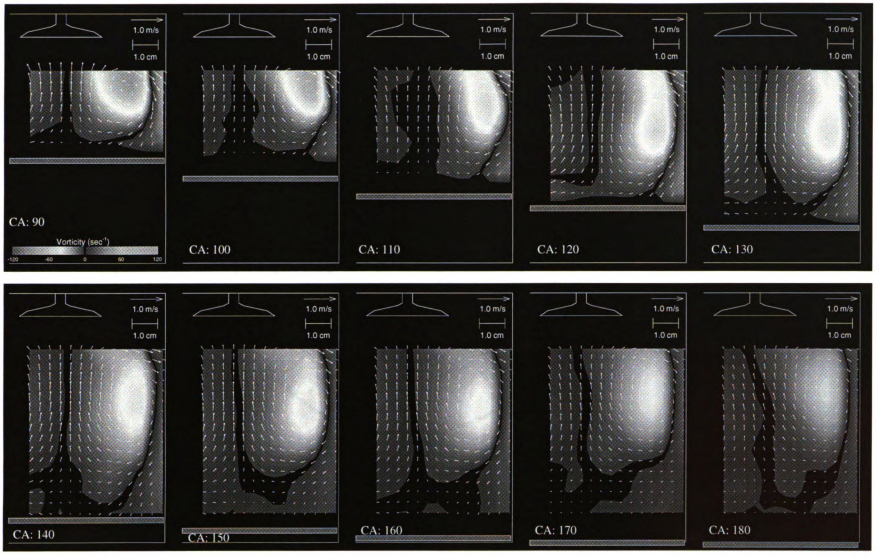

Figure B1. Cycle Averaged Velocity and Vorticity Fields with No Excitation

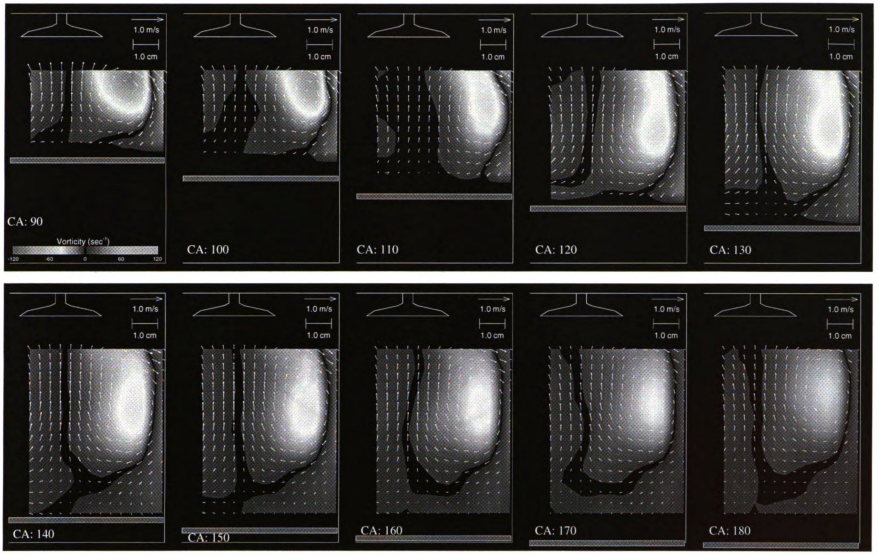

Figure B2. Cycle Averaged Velocity and Vorticity Fields with Excitation Conditions:
f: 20 Hz A: 1.00 mm Δ: 0-180 degrees

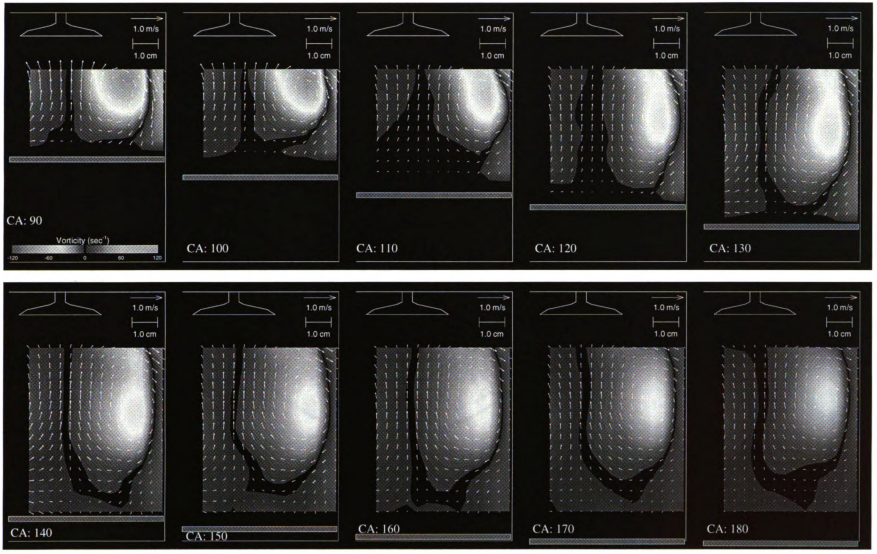

Figure B3. Cycle Averaged Velocity and Vorticity Fields with Excitation Conditions:
f: 30 Hz A: 1.00 mm Δ: 0-180 degrees

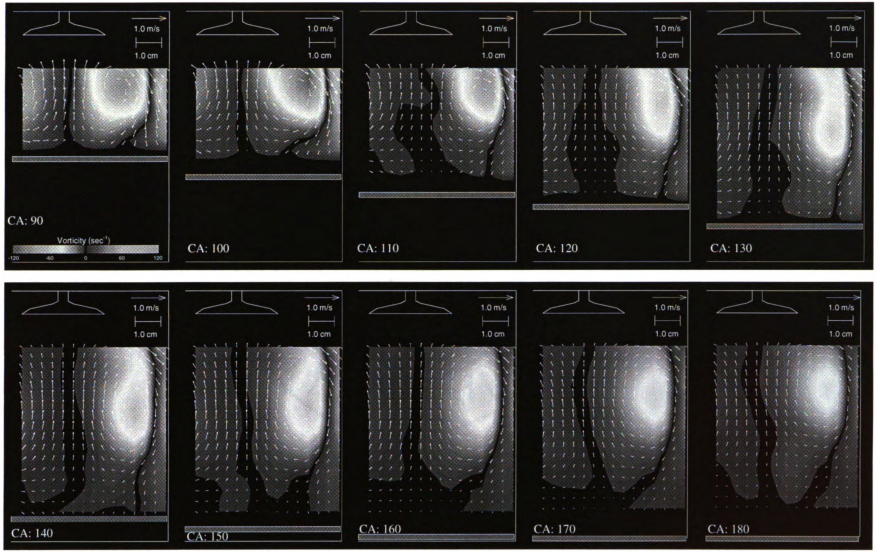

Figure B4. Cycle Averaged Velocity and Vorticity Fields with Excitation Conditions:
f: 40 Hz A: 1.00 mm Δ: 0-180 degrees

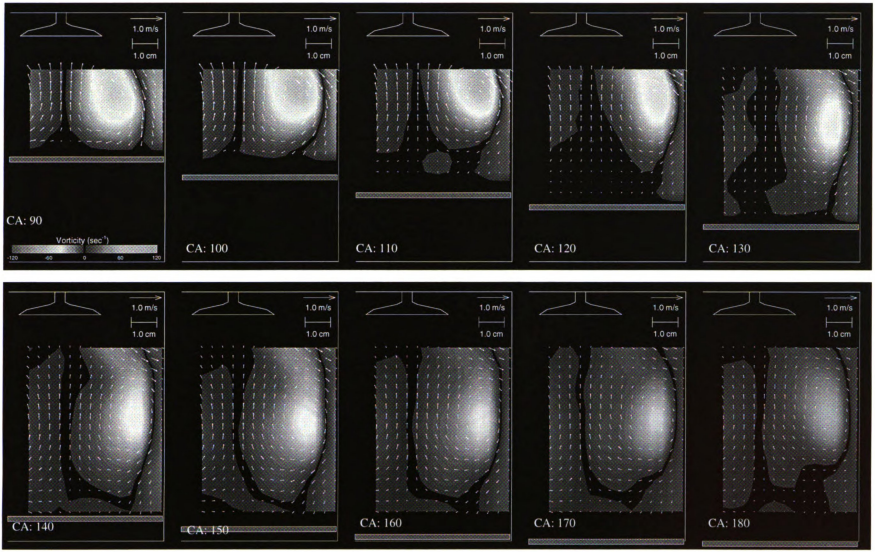

Figure B5 Cycle Averaged Velocity and Vorticity Fields with Excitation Conditions:
f: 60 Hz A: 1.00 mm Δ: 0-180 degrees

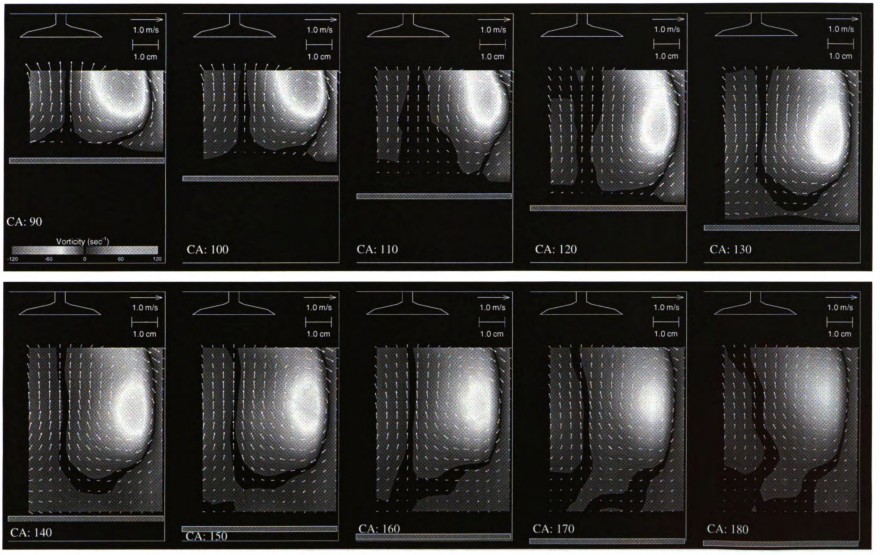

Figure B6. Cycle Averaged Velocity and Vorticity Fields with Excitation Conditions:
f: 40 Hz A: 0.35 mm Δ: 0-180 degrees

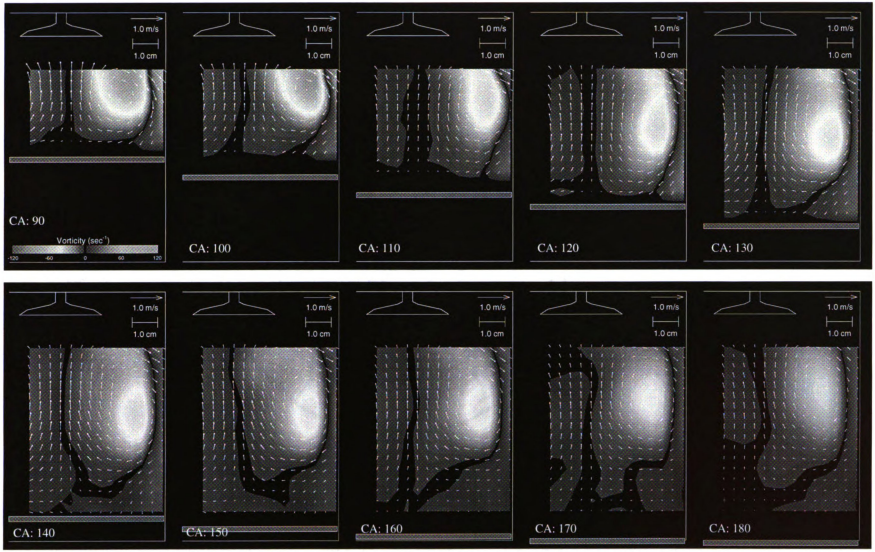

Figure B7. Cycle Averaged Velocity and Vorticity Fields with Excitation Conditions:
f: 60 Hz A: 0.35 mm Δ: 0-180 degrees

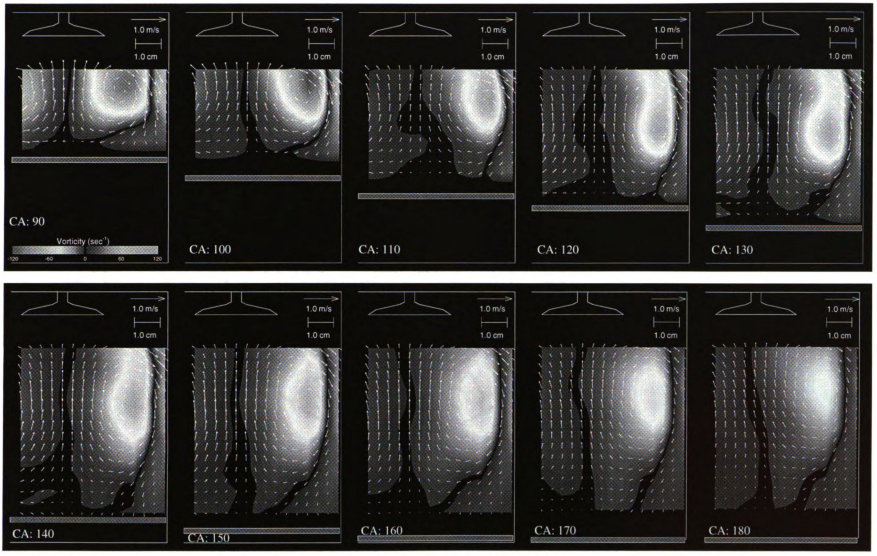

Figure B8. Cycle Averaged Velocity and Vorticity Fields with Excitation Conditions:
f: 40 Hz A: 0.35 mm Δ: 0-18 degrees

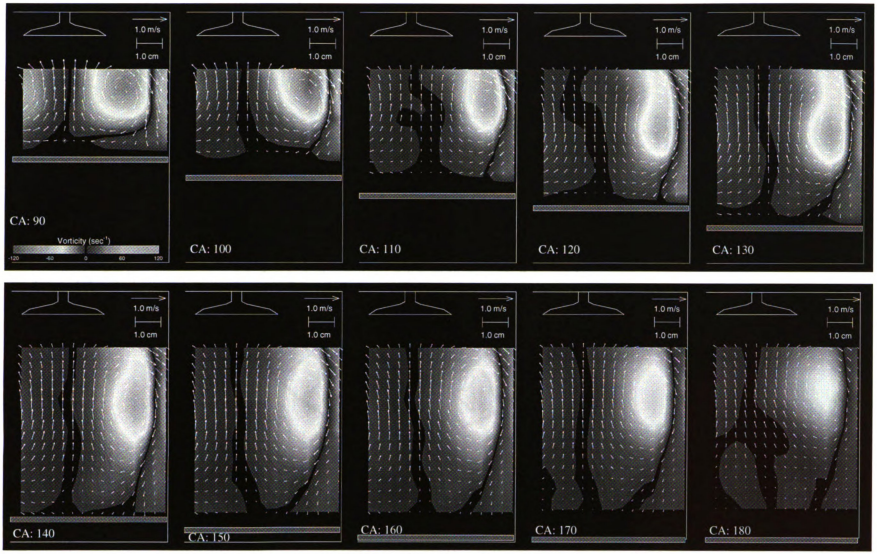

Figure B9 Cycle Averaged Velocity and Vorticity Fields with Excitation Conditions:
f: 60 Hz A: 0.35 mm Δ: 0-18 degrees

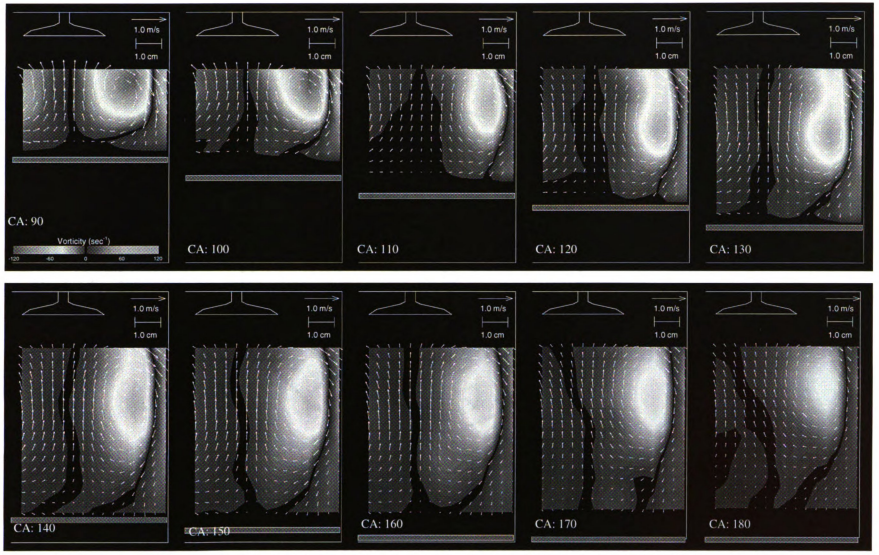

Figure B10. Cycle Averaged Velocity and Vorticity Fields with Excitation Conditions:
f: 90 Hz A: 0.35 mm Δ: 0-18 degrees

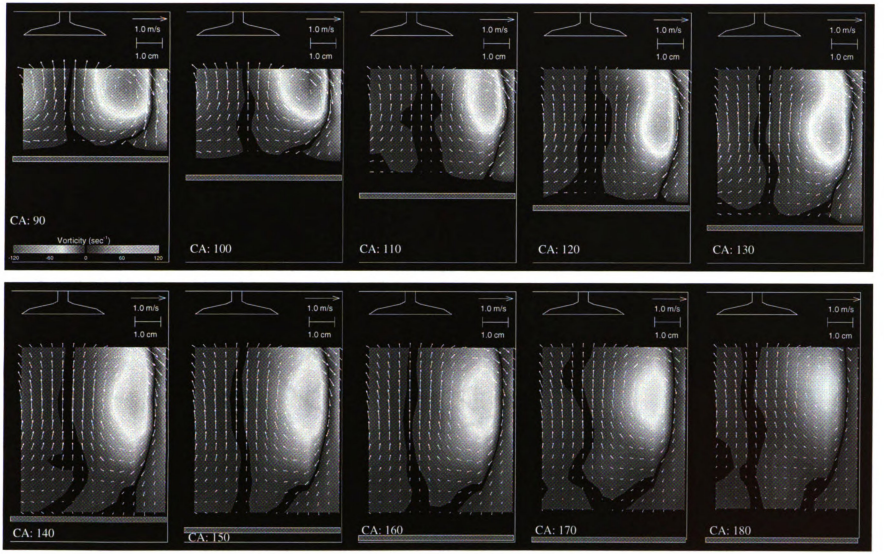

Figure B11. Cycle Averaged Velocity and Vorticity Fields with Excitation Conditions:
f: 40 Hz A: 1.00 mm Δ: 0-18 degrees

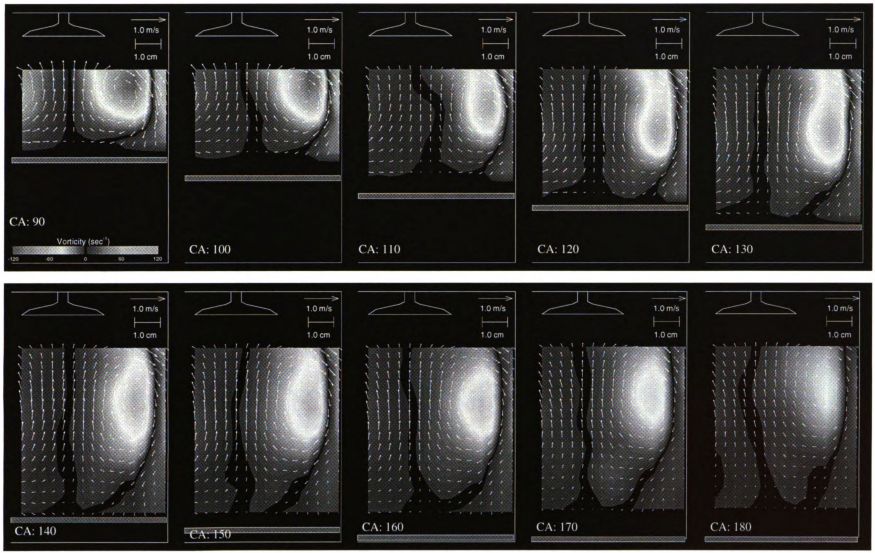

Figure B12. Cycle Averaged Velocity and Vorticity Fields with Excitation Conditions:
f: 60 Hz A: 1.00 mm Δ: 0-18 degrees

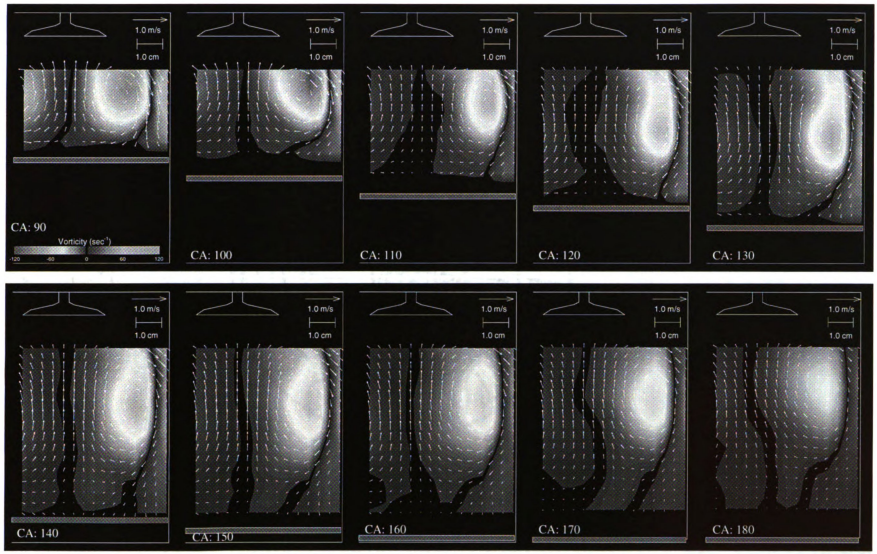

Figure B13. Cycle Averaged Velocity and Vorticity Fields with Excitation Conditions:
f: 40 Hz A: 0.35 mm Δ: 0-60 degrees

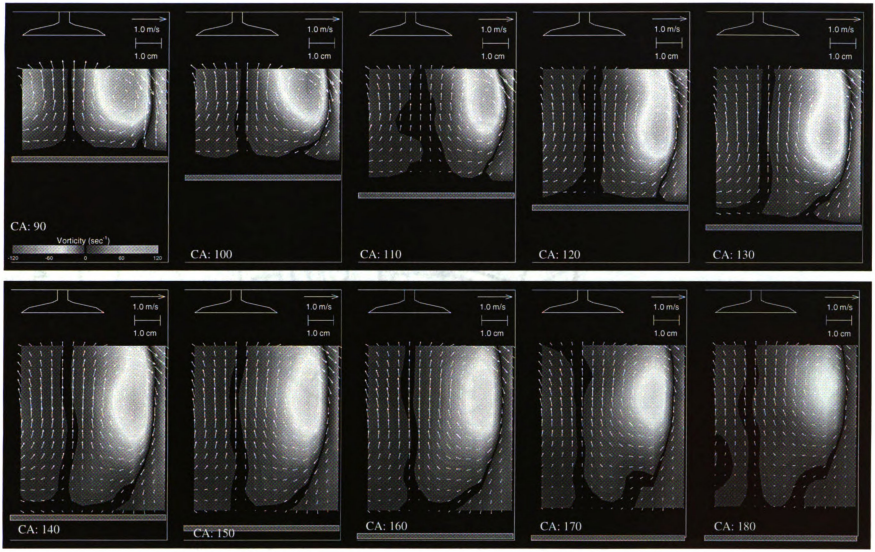

Figure B14. Cycle Averaged Velocity and Vorticity Fields with Excitation Conditions:
f: 60 Hz A: 0.35 mm Δ: 0-60 degrees

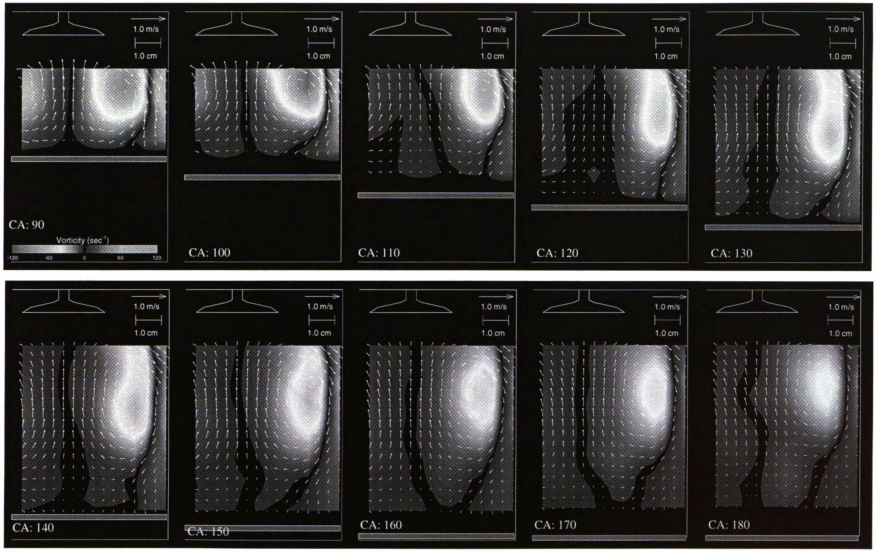

Figure B15. Cycle Averaged Velocity and Vorticity Fields with Excitation Conditions:
f: 90 Hz A: 0.35 mm Δ: 0-60 degrees

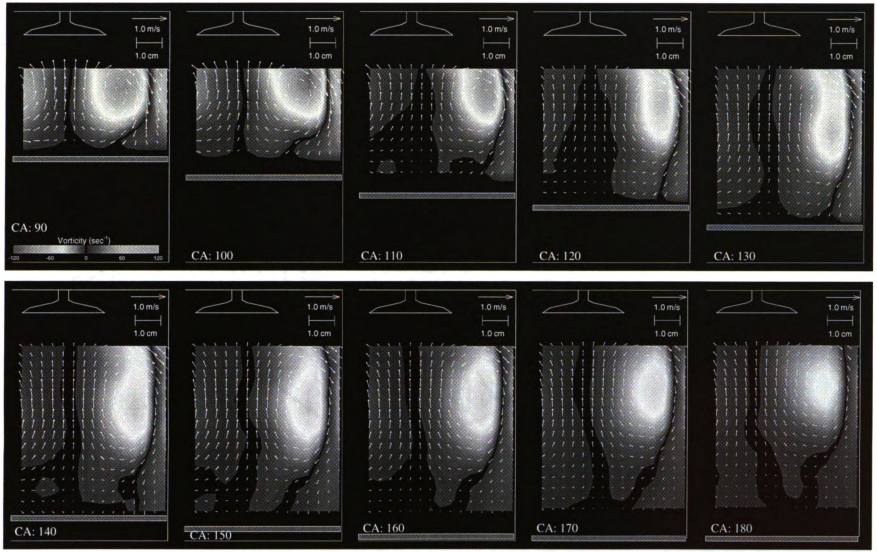

Figure B16 Cycle Averaged Velocity and Vorticity Fields with Excitation Conditions:
f: 40 Hz A:1.00 mm Δ: 0-60 degrees

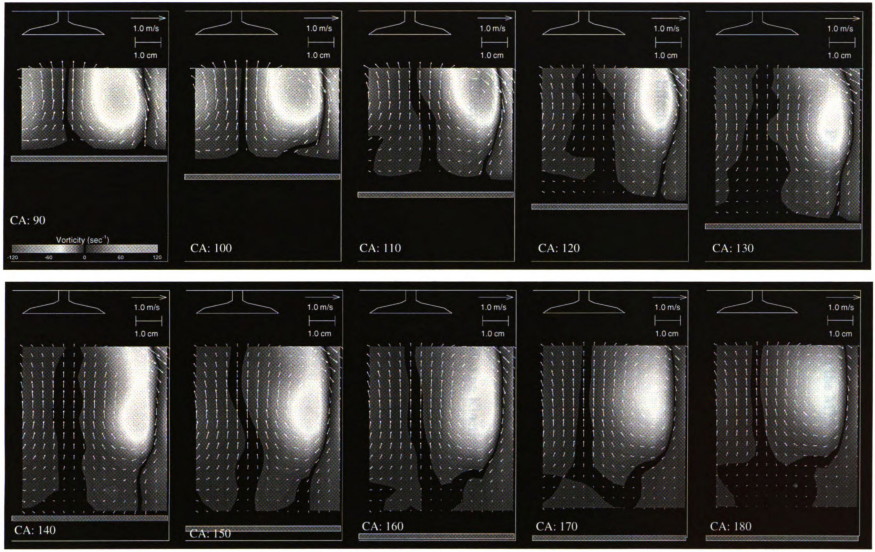

Figure B17 Cycle Averaged Velocity and Vorticity Fields with Excitation Conditions:
f: 60 Hz A:1.00 mm Δ: 0-60 degrees

APPENDIX C

Plots of Statistical Quantities from the MTV data

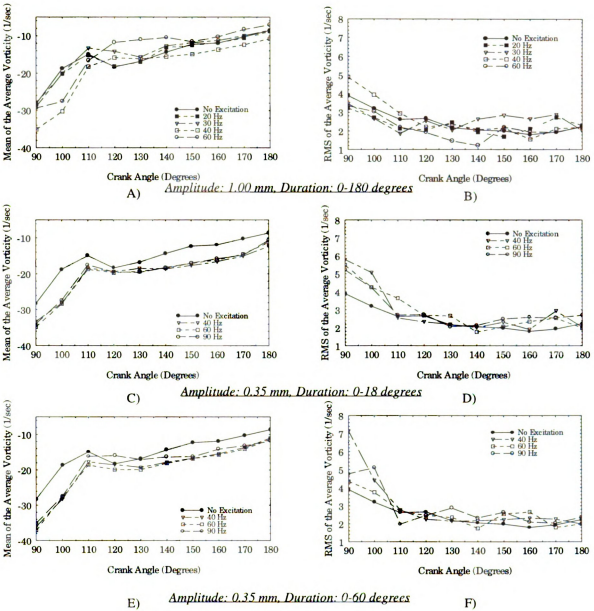

Figure C1. Effects of Frequency on the Mean and RMS of the Average Vorticity (Circulation Normalized by Area)

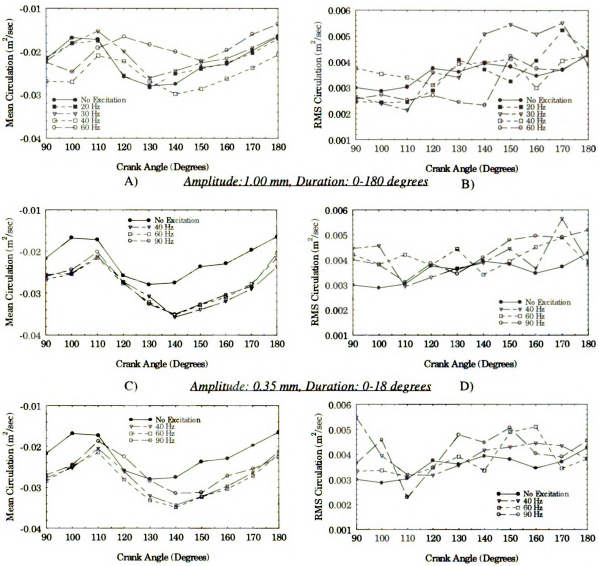

Figure C2. Effects of Frequency on Mean and RMS Circulation.

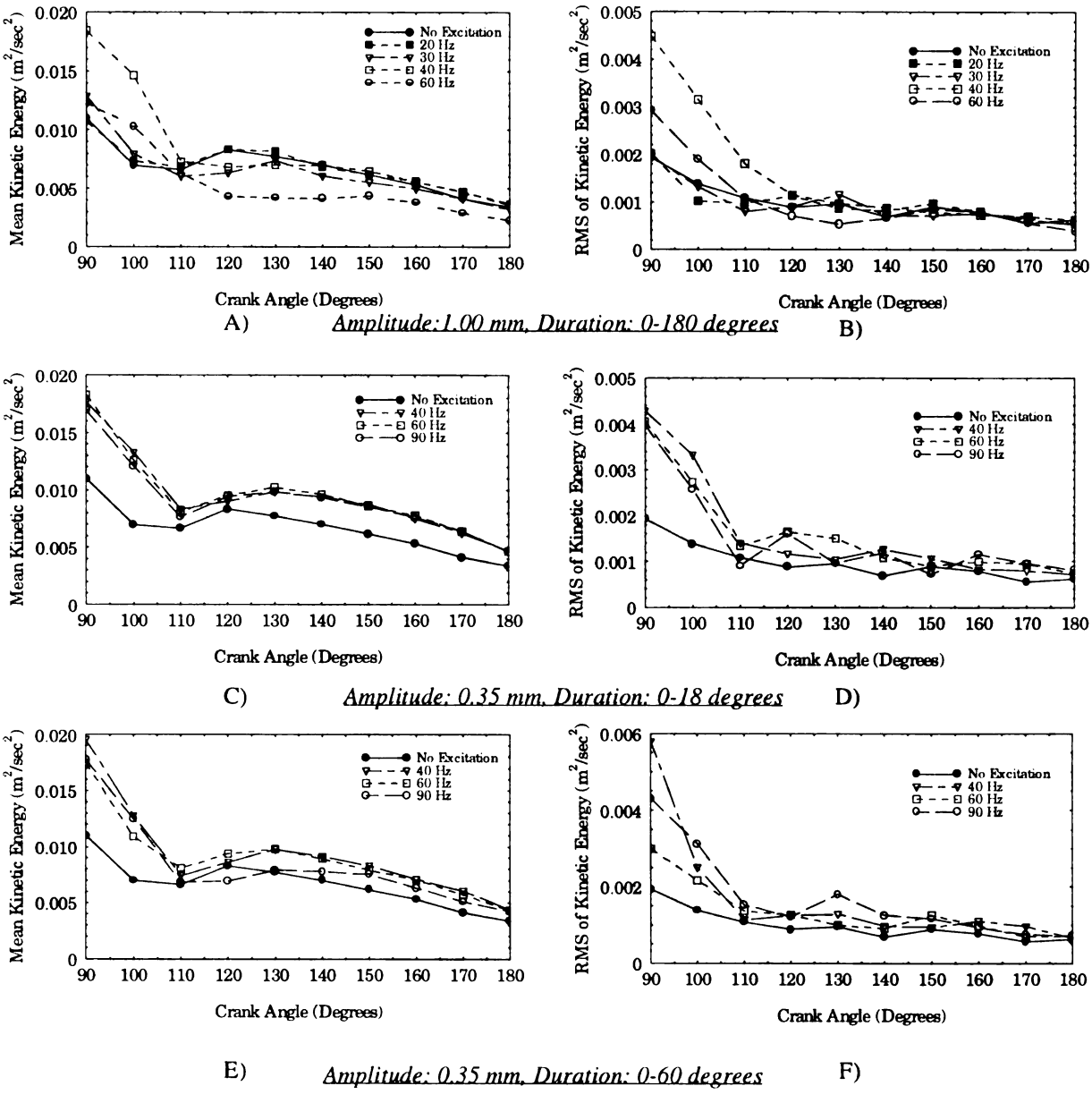

Figure C3. Effects of Frequency on Kinetic Energy per Unit Mass.

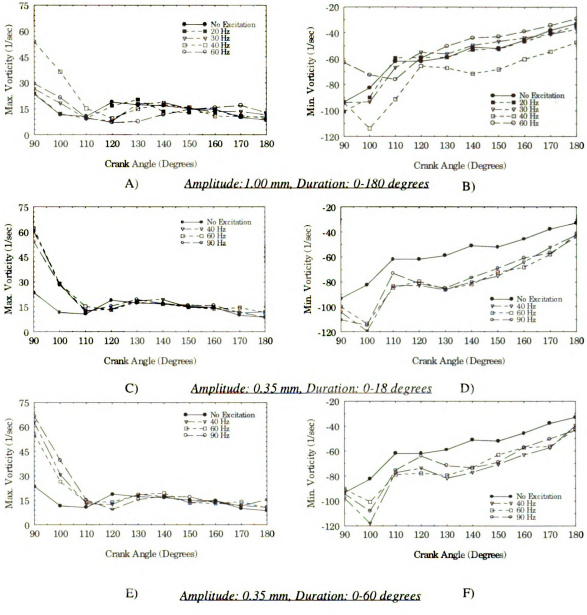

Figure C4. Effects of Frequency on Peak Vorticity Levels.

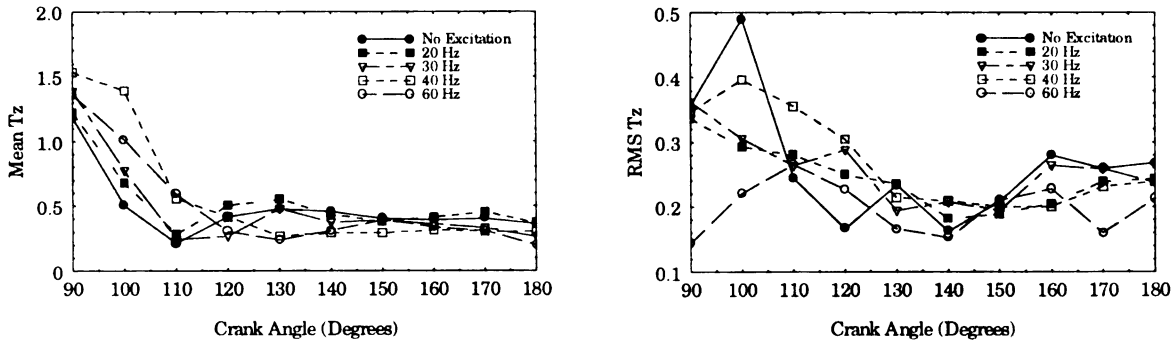

A) *Amplitude:1.00 mm, Duration: 0-180 degrees* B)

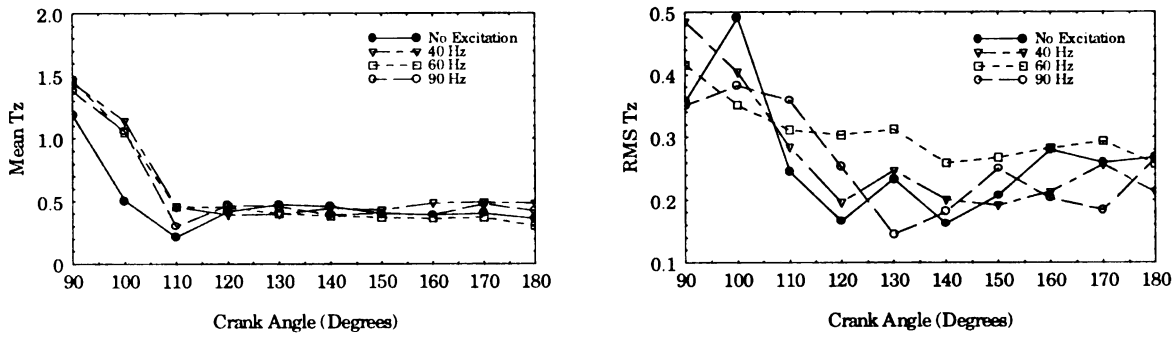

C) *Amplitude: 0.35 mm, Duration: 0-18 degrees* D)

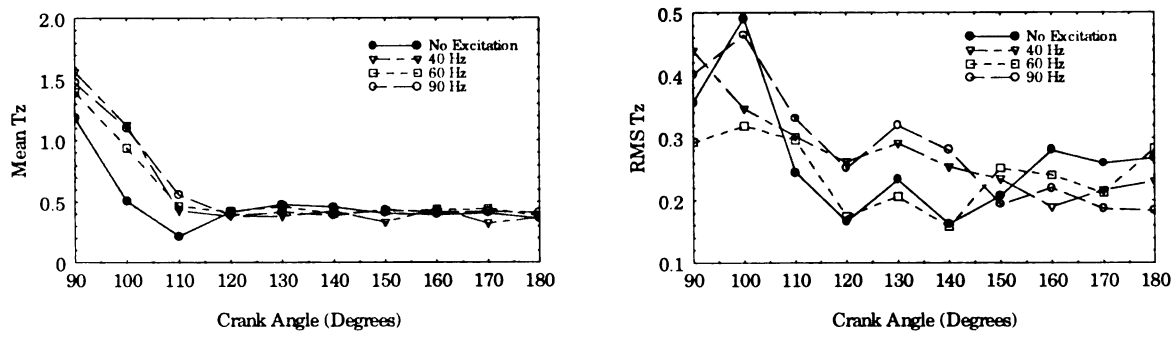

E) *Amplitude: 0.35 mm, Duration: 0-60 degrees* F)

Figure C5. Effects of Frequency on Tumble Ratio.

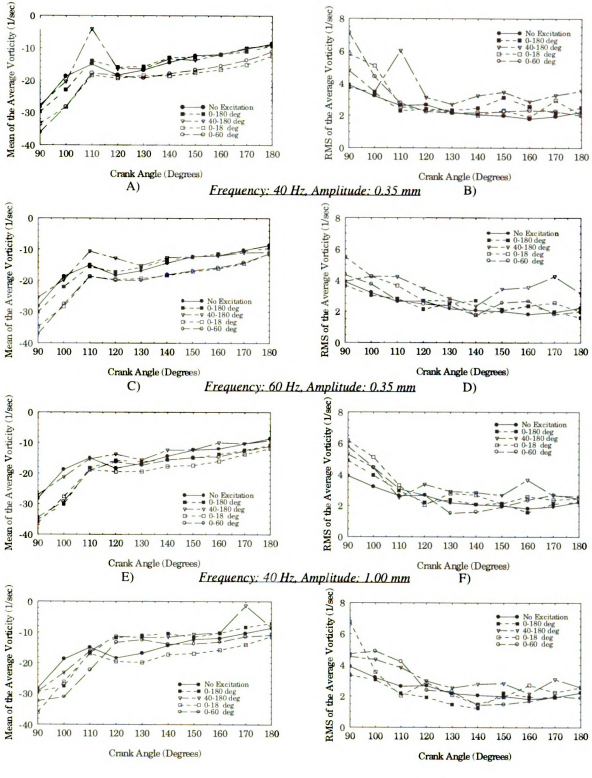

Figure C6. Effects of Amplitude and Excitation Duration on Mean and RMS of the Avergae Vorticity (Circulation/Area)

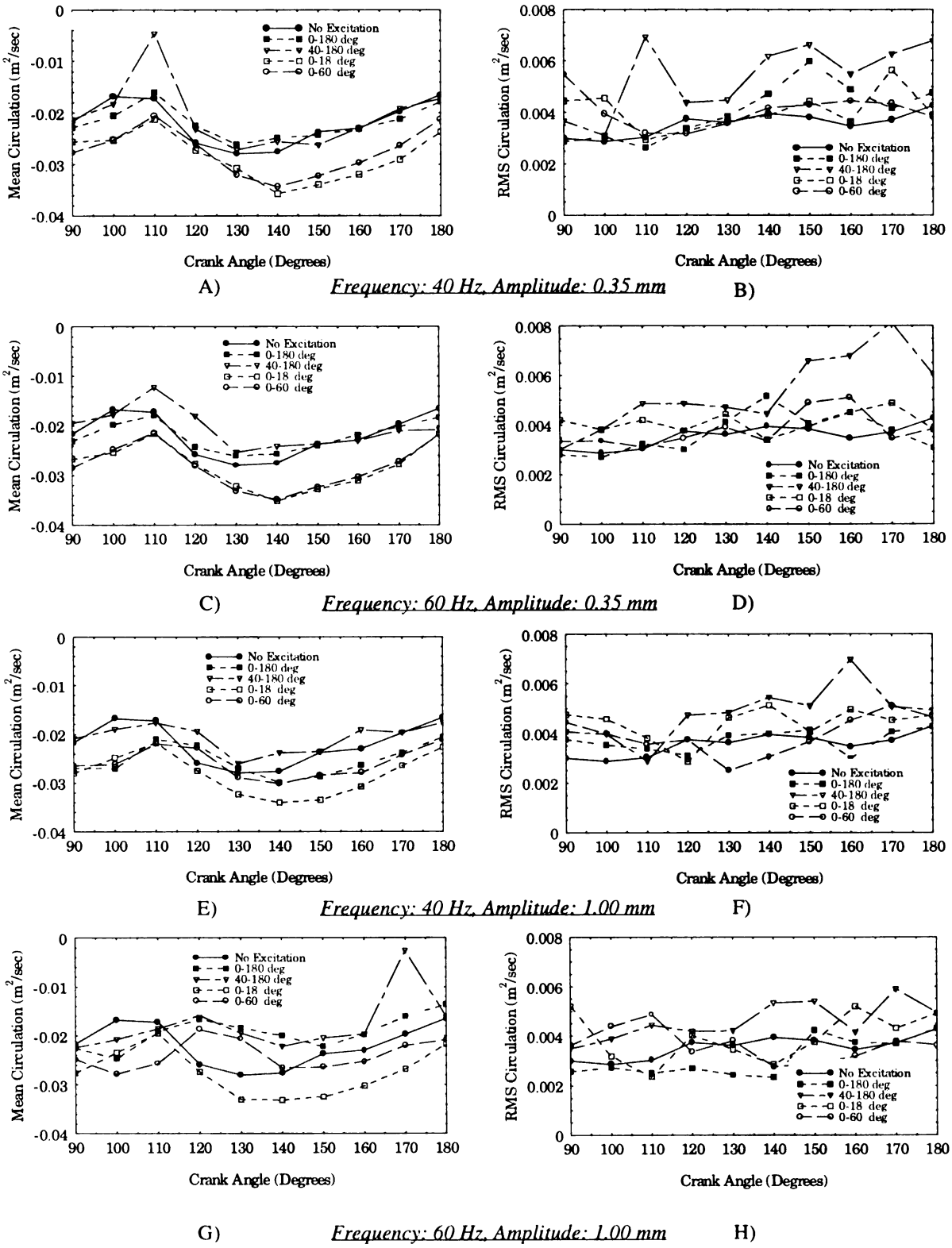

Figure C7. Effects of Amplitude and Excitation Duration on Mean and RMS Circulation.

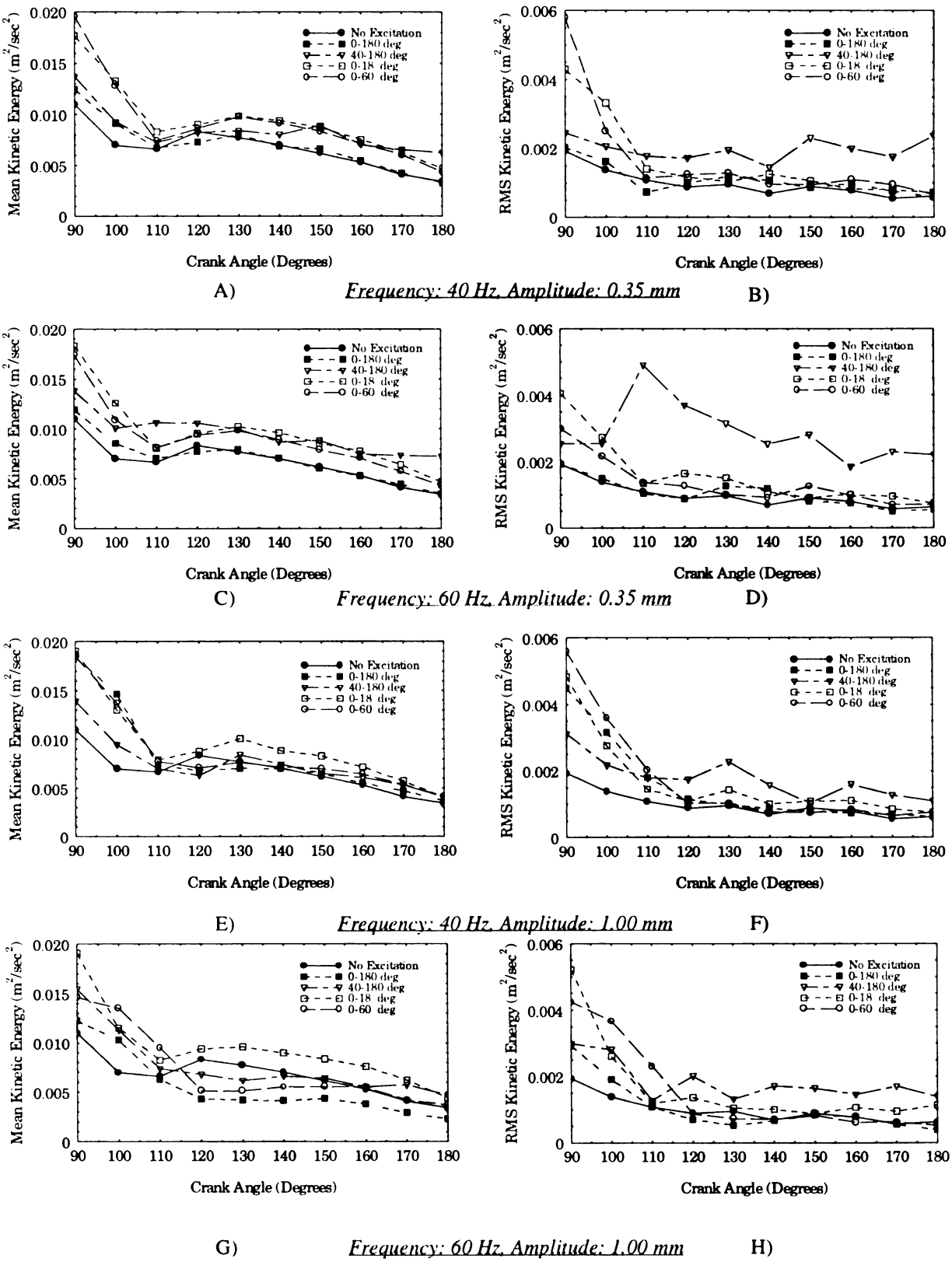

Figure C8. Effects of Amplitude and Excitation Duration on Kinetic Energy per Unit Mass.

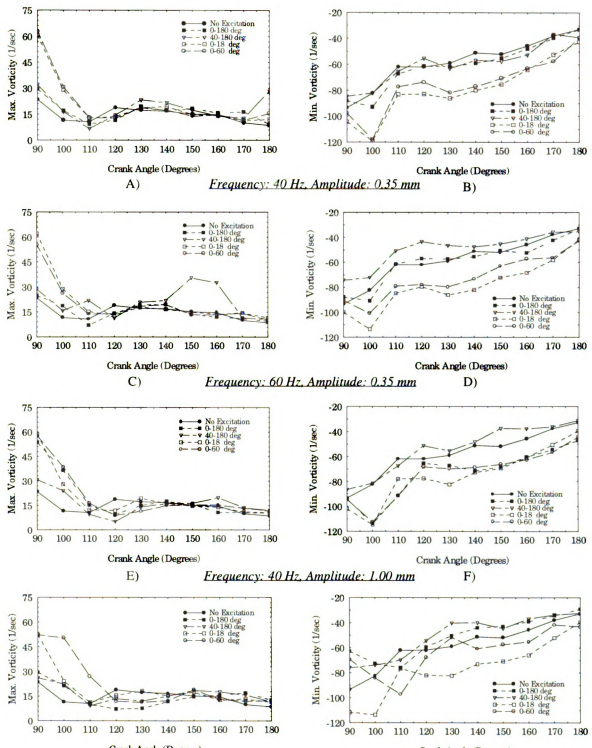

Figure C9. Effects of Amplitude and Excitation Duration on Peak Vorticity Levels.

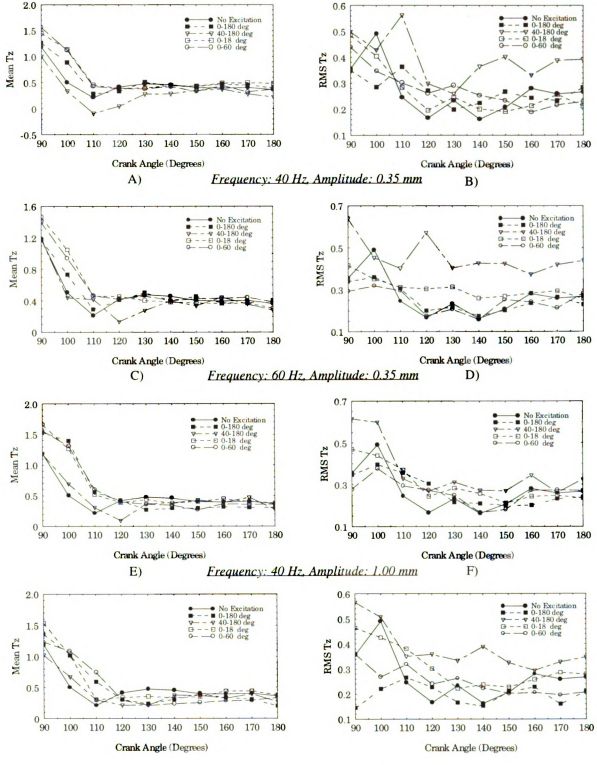

Figure C10. Effects of Amplitude and Excitation Duration on Tumble Ratio.

LIST OF REFERENCES

LIST OF REFERENCES

1. Gendrich, C. P. and Koochesfahani, M. M. (1996), "A spatial correlation for estimating velocity fields using molecular tagging velocimetry (MTV)," *Experiments in Fluids*, Vol. 22, pp. 67-77.

2. Tang, S. K. and Ko, N. W. M. (1994), "Experimental Investigation of the structure interaction in an excited coaxial jet," *Experimental Thermal and Fluid Sciences*, Vol 8, pp. 214-229.

3. Zaman, K. M. B. Q. and Hussain, A. K. M. F. (1980), "Vortex Pairing in a circular jet under controlled excitation. Part 1. General jet response," *Journal of Fluid Mechanics*, Vol. 101, part 3, pp. 449-441.

4. Zaman, K. M. B. Q. and Hussain, A. K. M. F. (1981), "The 'preferred mode' of the axisymmetric jet," *Journal of Fluid Mechanics*, Vol. 110, pp. 39-71.

5. Koochesfahani, M. M. and MacKinnon, (1991), "Influence of forcing on the composition of mixed fluid in a two-stream shear layer," *Physics of Fluids* A, Vol. 3, pp. 1135-1142.

6. Dahm, W. J. A., Frieler, C. E., and Tryggvason, G. (1992), "Vortex structure and dynamics in the near field of a coaxial jet," *Journal of Fluid Mechanics*, Vol. 241, pp. 371-402.

7. Khodadadi, J. M. and Vlachos, N. S. (1987), "Experimental and numerical study of confined coaxial turbulent jets," *American Institute of Aeronautics and Astronautics*, Vol. 27, No. 5, pp.532-541.

8. Khalighi, B. and Huebler, M. S. (1988), "A transient water analog of a dual intake valve engine for intake flow visualization and full-field velocity measurements," *Society of Automotive Engineers*, Paper 880519

9. Haworth, D. C., El Tahry, S. H., and Huebler, M. S. (1990), "Multidimensional port and cylinder flow calculations for two and four valve per cylinder engines: Influence of intake configuration on flow structure," *Society of Automotive Engineers*, Paper 900257

10. Hall, M. J. and Bracco, F. V. (1987) "A study of velocities and turbulence intensities measured in a firing and motored engines," *Society of Automotive Engineers*, Paper 870453.

11. Ko, N. W. M. and Chan, W. T. (1978) "Similarity in the region of annular jets: three configurations," *Journal of Fluid Mechanics*, Vol. 84, Part 4, pp. 641-656.

12. Lee, J. and Farrell, P. V. (1993) "Intake valve flow measurements of an IC engine using particle image velocimetry," *Society of Automotive Engineers*, Paper 930480.

13. Stuckey, M. J., Nino, E., Gajdeczko, B., and Felton, P. G. (1994) "Two color particle image velocimetry technique for an internal combustion engine," *Experimental Thermal and Fluid Science*, Vol. 8, pp. 305-314.

14. Hussain, A. K. M. F. (1983) "Coherent structures - reality and myth," *Physics of Fluids*, Vol 26, No. 10, pp. 2816-2850.